Raman Microspectrometry Applied to the Study of Electrode Materials for Lithium Batteries

Rita Baddour-Hadjean* and Jean-Pierre Pereira-Ramos

Institut de Chimie et Matériaux Paris-Est, UMR 7182 CNRS et Université Paris XII, 2 rue Henri Dunant 94320 Thiais, France

Contents

1. Introduction

Raman spectroscopy is a vibrational technique that provides unique structural information at the atomic scale[1,2] on inorganic and organic compounds. By coupling an optical microscope to a conventional Raman spectrometer, the technique becomes a microprobe with a spatial resolution of less than 1 μm, determined by the wavelength of the

* Phone: 33 1 49 78 11 55. Fax: 33 1 49 78 11 95. E-mail address: baddour@icmpe.cnrs.fr.

Rita Baddour-Hadjean was born in Coulommiers, France, in 1964. She received a chemical engineering diploma from the National School of Chemistry of Paris (ENSCP) in 1988. Working on the electrochemical and structural properties of sol−gel vanadium oxides usable as positive electrodes in lithium batteries, she obtained her Ph.D. degree in Analytical Chemistry from Université Pierre et Marie Curie—Paris VI in 1991. Then she joined the CNRS as researcher to understand the role that proton dynamics plays on the ionic conduction mechanism of various materials, using Inelastic Neutron Scattering in combination with other vibrational techniques, such as infrared and Raman spectroscopies. Since 2000, using Raman microspectrometry, she has focused on the study of electrode materials for rechargeable lithium batteries. This kind of investigation of the local structural changes induced by the lithium insertion process provides a better understanding of their electrochemical behavior. She earned a Habilitation qualification (Habilitation à Diriger des Recherches) from the Université Pierre et Marie Curie—Paris VI in 2004 and then joined the group of Electrochemistry and Spectroscopy of Materials, managed by Jean-Pierre Pereira-Ramos at the Institute of Chemistry and Materials Paris Est (ICMPE), CNRS, Thiais, France. Her current research interests include the study of various electrode materials (bulk and thin film oxides), *in situ* Raman microspectrometry measurements, and a theoretical approach based upon lattice dynamics simulations to get a quantitative assignment of the vibrational features.

radiation and the numerical aperture of the microscope objective. This has prompted several significant Raman applications in various fields dedicated to the characterization of a wide range of materials: inorganic solids, ceramics, semiconductor materials, protective coatings, polymers, and battery materials.

Raman spectroscopy has been found to be very sensitive to the state of metal oxide supported catalysts, with the Raman frequencies being dependent on the metallic oxidation state.[3] As the Raman probe is capable of performing studies of highly localized volumes with dimensions comparable to the grain sizes or phase size in microstructures, several research groups have reported Raman studies on polyphase ceramics. Microphases and inclusions can be observed directly under the microscope, then allowing the character-

Jean-Pierre Pereira-Ramos was born in Saint-Maur des Fossés, France, in 1957. He received a Ph.D. in Analytical Chemistry from Université Pierre et Marie Curie—Paris VI in 1982. He joined the CNRS as researcher in 1983. Working on the electrochemistry of lithium intercalation compounds in new sulfone-based electrolytes, he earned the grade of Doctor of Physical Sciences from Université Paris XII—Val de Marne in 1988. For almost 15 years he mainly has developed research activity on the synthesis by soft chemistry of new lithium intercalation compounds and their electrochemical properties. With Prof. Noël Baffier from ENSCP and University Paris VI, he has investigated the relationships between the structure, morphology, and electrochemistry of novel sol−gel transition metal oxides as positive electrodes for rechargeable Li and Li ion batteries. Director of research in CNRS since 1996, he currently heads the Group of Electrochemistry and Spectroscopy of Materials at the Institute of Chemistry and Materials Paris Est (ICMPE), CNRS, Thiais, France. The areas presently studied in his group include intercalation compounds, thin film oxides for Li microbatteries, and also lithiated transition metal nitrides and silicium nanowires as negative electrodes. His main research interest is to provide a comprehensive view of the Li insertion mechanism into such electrode materials. He also develops in his group Raman spectroscopy as a powerful tool to characterize the local structural changes occurring in electrode materials under operation.

ization of impurity phases, the study of phase transition mechanisms,[4] or the identification of different polymorphic forms, as reported, for example, in the case of silicon and boron nitride[5] and partially stabilized zirconia.[6] In the latter case, the use of the Raman imaging technique has enabled us to map phase-transformed zones accompanying crack propagation. Intense interest in the investigation and characterization of high T_c superconducting oxides by Raman spectroscopy has also been demonstrated since their discovery in 1986. In addition to fundamental studies of phonon and related electronic properties,[7] Raman spectroscopy has been extensively used as a controlling technique to evaluate the quality of variously prepared high-T_c materials (e.g., bulk powders, thin films, and single crystals). In particular, it has been found to be an excellent tool for characterizing the homogeneity and stoichiometry on the micrometer scale of superconducting films deposited on substrates through the observation of specific vibrational modes which are very sensitive to the oxygen content.[8] Micro-Raman spectroscopy has also been recognized as one of the most sensitive tools for studying the structural properties of carbonaceous materials.[9] In addition to its spatial resolution, which permits the study of individual microcrystals as well as thin films, Raman spectroscopy can distinguish between the various forms of carbon. Thus, carbon with sp^3-type bonding (diamond), carbon with sp^2-type bonding (graphite and carbonaceous materials), and carbon in mixtures with these two types of bonding (diamond-like carbons) can be characterized by their Raman spectra.[10] Protective diamond and silica coatings have also been characterized using the Raman microprobe tech-

nique. In the case of diamond films, the deep analysis of Raman scattering data, including the peak position, intensity, area, and width, allows us to obtain the sp^3- and sp^2-bonded C contents and the nature of internal stresses in the films.[11−13] Semiconductors in bulk, thin film, and device configurations have been thoroughly investigated. For such materials, Raman microspectrometry is very well suited to collect a wealth of information on the spatial distribution of physical quantities such as strains,[14] atomic fraction in mixed crystals, impurity concentrations, free carrier concentrations,[15] and local crystallographic orientation.[16] These data are useful not only to evaluate the quality of a sample but also to infer the relevant dynamical processes, e.g. growth of crystallites, atomic diffusion, and reactions at interfaces or surfaces. Numerous applications of Raman microanalysis can also be found in the field of art, jewelry, archeology, and forensic science,[17−22] as it constitutes a well adapted technique for the nondestructive examination of molecular species with good spatial resolution. Pigment investigation is one of the most active research domains within art analysis using Raman spectroscopy,[19] but other important research topics can be found, including the study of corrosion phenomena,[20] the analysis of glasses and ceramics,[21] and the study of minerals and gemstones.[22]

This review is focused on key issues and trends in Raman research on materials usable as negative or positive electrodes[23] in secondary Li and Li ion batteries. Rechargeable Li metal batteries use metallic Li as the negative electrode while lithium ion batteries use carbon or a Li intercalation compound as the negative one. The storage of electrical energy will be far more important in this century than it was in the last. The need for clean and efficient energy storage from renewable sources is important. Rechargeable batteries are required to power various portable consumer electronic devices (cell phones, PDAs, laptop computers, etc.), to power electric vehicles, for implantable medical applications, but also to store electricity from wind/solar energy. Advances in rechargeable lithium ion batteries have allowed the success of mobile electronic equipment, and the worldwide market for rechargeable lithium batteries is growing every year. But now an increase in energy and power density to meet these future challenges is needed. To promote such developments, it is essential to find new high performance materials but also to understand the materials properties that are responsible for the electrochemical features, cycle life, and structural behavior of electrode materials under operation.

The basic process that occurs in a rechargeable lithium battery is the intercalation of lithium ions into different host materials. One fundamental problem is the loss of capacity during successive electrochemical insertion−deinsertion processes. As is well-known, the electrochemical properties of such materials (e.g., specific capacity, reversibility, rate capability, cycling behavior, ...) are strongly dependent on the structural changes induced by the lithium insertion reaction. Therefore, the establishment of clear relationships between electrochemical and structural data seems to be one of the key issues for better understanding and further improving the electrochemical performance of electrode materials for rechargeable lithium batteries. Considering the experimental techniques carried out to fulfill this requirement, they allow the obtainment of either long-range (X-ray, neutron, or electron diffraction, ...) or short-range data (X-ray absorption, NMR, EPR, XPS, ...). Among the local probes, Raman spectroscopy is very appropriate, since determination of frequencies of normal vibrations provides a very

sensitive tool to detect structural variations at the atomic level. Indeed, unique molecular and crystalline information is then accessible, e.g. local disorder, changes in bond lengths, bond angles, coordination, Li dynamics, and cation ordering. As a matter of fact, a significant amount of Raman data can be found in the literature. We present here quantitative results obtained over the past few years from Raman microspectrometry on metallic lithium, carbonaceous materials, transition metal oxide MO_y (M = V, Mn, Ti), lithiated transition metal oxides Li_xMO_y (M = Co, Ni, Mn, Ti), and phospho-olivine $LiFePO_4$ compounds used as negative or positive electrode materials in Li or Li ion batteries. These studies have been selected in order to highlight the extraordinary potential of Raman microscopy to obtain structural information on the material under operation and to provide insight into the mechanisms governing the electrode performances.

2. The Raman Effect

2.1. Principle

It seems appropriate to review first the Raman effect principle, which is described in detail by Turrell et al.[24] The Raman effect was named after one of its discoverers, the Indian scientist Sir C. V. Raman, observed the effect by means of sunlight in 1928. This phenomenon results from the interaction of light and matter. When a photon of light interacts with a molecule, the photon can be absorbed or scattered. Considering the absorption process, it requires, first, that the energy of the incident photon is equal to the energy difference between two states of the molecule (this is referred to as the resonance condition) and, second, that the transition between the two states is accompanied by a change in the dipole moment of the molecule. Such conditions are those corresponding to infrared absorption. Photons which are not absorbed will be scattered and the incident photons need not to be resonant with two states of the molecule for scattering to occur. In quantum mechanics, this interaction is described as an excitation to a virtual state lower in energy than a real electronic transition, as shown in the energy level diagram shown in Figure 1a. When scattering of the photon occurs without any change in the atomic coordinates of the molecule, the photon is elastically scattered. It exhibits the same energy (frequency) and, therefore, wavelength as the incident photon. This process is commonly referred to as Rayleigh scattering. However, for a very small fraction of light (approximately 1 in 10^7 photons), a vibrational motion occurs. A quantum of vibrational energy is then transferred between the molecule and the incident photon and the remaining energy is scattered inelastically such that the energies of the incident and scattered photons are no longer equal. The process leading to this inelastic scattering constitutes the Raman effect. In this case, the molecule may either gain energy from or lose energy to the photon. If the transfer of energy in the virtual state is from the photon to the molecule, the scattered photon will be lower in energy than the incident photon and the phenomenon is referred to as Stokes Raman scattering. Conversely, if the transfer of energy in the virtual state is from the molecule to the photon, the scattered photon will be higher in energy than the incident photon, which is referred to anti-Stokes Raman scattering (Figure 1a). In classical terms, the scattering process can be viewed as a perturbation of the molecule's electric field. Vibrational Raman scattering occurs because a molecular vibration
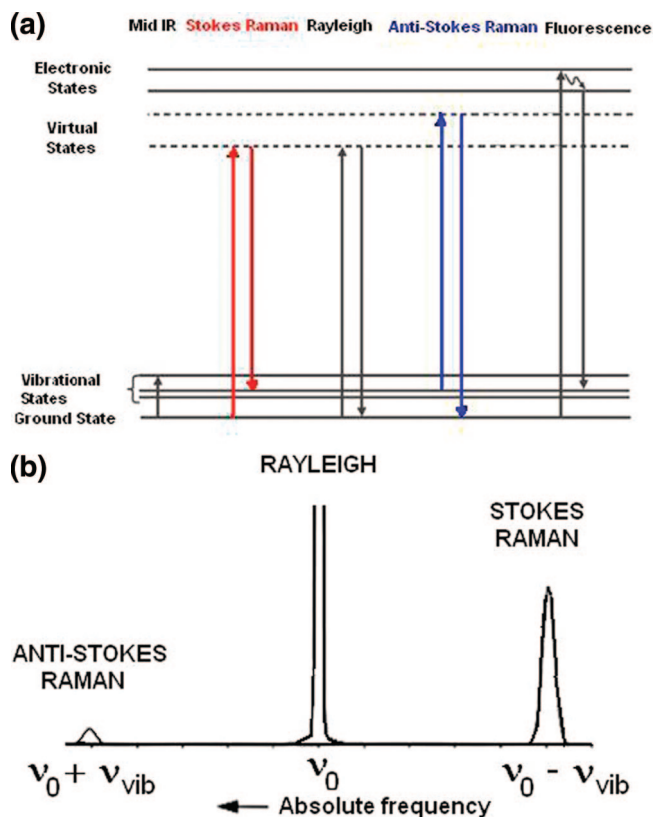

Figure 1. (a) Energy level diagram for different processes. (b) Raman and Rayleigh scattering of excitation at a frequency ν_0. The molecular vibration in the sample is of a frequency ν_{vib}.

induces a change in the polarizability. The polarizability, α, measures the ease with which the electron cloud around a molecule can be distorted. The change is described by the polarizability derivative, $\delta\alpha/\delta Q$, where Q is the normal coordinate of the vibration. The selection rules for Raman-active vibrations are linked to molecular symmetry and identify vibrations that change molecular polarizability.

A Raman spectrum is a plot of the intensity of Raman scattered radiation as a function of its frequency difference from the incident radiation (Figure 1b). This difference is called the *Raman shift*. Note that, because it is a difference value, the Raman shift is independent of the frequency of the incident radiation. Figure 1b illustrates the symmetry of Stokes and Anti-Stokes bands; however, because the ground-state population is greater than that of the excited state, the Stokes lines are more intense than the Anti-Stokes lines. For this reason, Raman spectra are often plotted as a function of intensity versus the Stokes-shifted frequencies in wavenumbers (cm^{-1}). Frequency shifts between the incident radiation and the Raman-scattered radiation correspond to the vibrational energy levels of the molecule or the crystal. Many parameters, e.g. local environment, symmetry of the crystal, atomic mass, bond order, H-bonding, molecular substituents, atomic environment, molecular geometry, structural disorder, and strains, can affect the vibrational force constants, which, in turn, dictate the vibrational energy. Hence, Raman spectroscopy allows the study of intramolecular vibrations, crystal lattice vibrations, and other motions of extended solids.

In addition to the Raman shift, which allows the determination of the vibrational frequencies of the normal modes, another property can be reached from Raman measurements, which is the polarization of the diffused light. In the ideal case of a crystal, the nature of the Raman spectrum depends
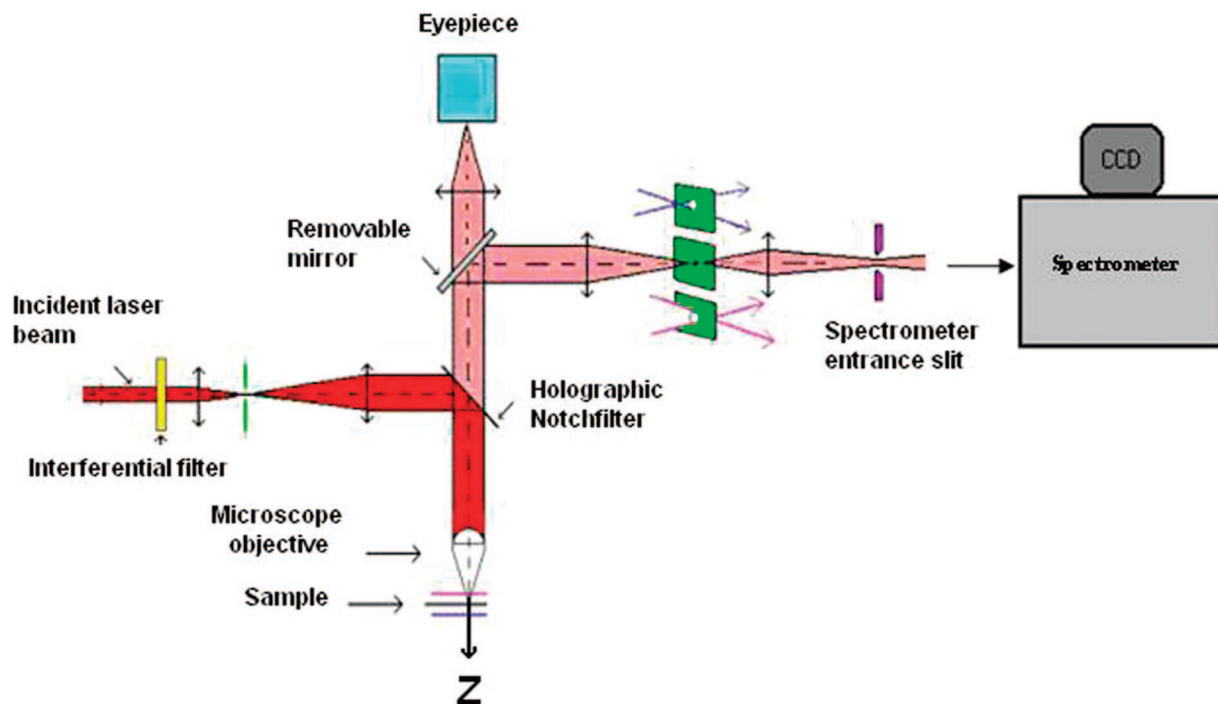
Figure 2. Schematic description of a confocal Raman microspectrometer system

on the orientation of the crystallographic axes with respect to the direction and polarization of both the excitation and the scattered light. Hence, polarized Raman spectroscopic investigations of single crystals are very useful in the interpretation of the Raman spectra of crystalline samples, since they can, by suitable choices of orientation, lead to the number and symmetry of the active modes.[24]

Quantum mechanics requires that only concerted atomic displacements are allowed for a given molecule. These are known as normal modes, which refer to molecular vibrations where each atom moves with the same frequency. A linear molecule with N atoms has $3N - 5$ normal modes, and a nonlinear molecule has $3N - 6$ normal modes of vibration. There are several types of motion that contribute to the normal modes. Some examples of molecular vibrations are as follows:

• stretching—a change in the length of a bond;
• bending—a change in the angle between two bonds;
• rocking—a change in the angle between a group of atoms and the rest of the molecule;
• wagging—a change in the angle between the plane of a group of atoms and a plane through the rest of the molecule;
• twisting—a change in the angle between the planes of two groups of atoms;
• out-of-plane—the atom moves in and out of the plane of the other atoms.

In a rocking, wagging, or twisting coordinate, the angles and bond lengths within the groups involved do not change. Rocking is distinguished from wagging by the fact that the atoms in the group stay in the same plane.

Molecules or crystals can be classified according to symmetry elements or operations that leave at least one common point unchanged. This classification gives rise to the point group representation for the molecule, which is uniquely defined by a set of symmetry operations—rotations C_n, reflections (σ_h, σ_v, and σ_d), inversion i, and improper rotations $S_n = C_n\sigma_h$—that transform that molecule into itself.[25] The full information of all symmetry transformations

in a point group is given in the so-called character tables. Character tables not only give the number and degeneracy of normal modes, but they also tell us which of the normal modes will be IR-active, Raman-active, or both. It turns out that a fundamental transition will be Raman-active if the normal mode involved belongs to the same symmetry representation as any one or more of the Cartesian components of the polarizability tensor of the molecule.

2.2. Experimental Considerations

The main features of the Raman microspectrometry system can be described by the basic layout shown in Figure 2 and described in detail by Delhaye et al.[26] In a Raman microspectrometer, the backscattering geometry is employed: the laser beam is focused on the sample through the microscope objective, and then the Raman light is collected by the same objective in the inverse direction of the incident light. The use of a microscope operating in a 180° back-scattering geometry eliminates the need to continually adjust the laser onto the sample and to focus the scattered light onto the spectrometer. Raman microspectrometers utilize research grade microscopes to focus the excitation onto the sample and to collect and transfer the Raman scattered light into the Raman spectrometer. High numerical aperture microscope objectives greatly enhance the spatial resolution and the optical collection power of the Raman instrument. These Raman microscopes are easy to use and are capable of analyzing small areas (~ 1 μm^2), which is an excellent spatial resolution to determine the distribution of chemical species. The concept of confocal scanning microscopy was introduced by Minsky[27] in the early 1960s to overcome some of the limitations of the conventional optical microscope. With this technique a significant improvement in both the contrast and the spatial resolution may be obtained. Unlike a conventional microscope, where the entire field is illuminated, the confocal system measures the intensity of the light reflected or transmitted by a very small area of sample.

Detailed theoretical and experimental studies on the properties of confocal microscopes can be found elsewhere.[28] The application of the confocal principle to Raman spectroscopy was first described in the 1990s.[29] The Raman microscope focuses the laser beam down to a small volume (on the order of 1 μm^3 in air) and is operated readily in a confocal mode by placing an aperture at a back focal plane of the microscope.[30] The aperture improves the lateral and axial spatial resolution of the microscope, allowing nondestructive depth profiling by acquiring spectra as the laser focus is moved incrementally deeper into a transparent sample. The critical importance of a correct interpretation of confocal Raman data is reported in many works.[31−33]

Raman microspectrometers are generally composed of several main parts:

1. The excitation source (laser). Lasers revolutionized Raman spectroscopy in the 1970s because they give a coherent beam of monochromatic light and can have very high power. Their high intensity allows the production of a detectable amount of Raman scatter.

2. The collection device. Monochromatic light from the laser passes through an interference filter to obtain the desired bandwidth with an improved rejection of the unwanted wavelengths. Then the laser beam is reflected by a holographic notch filter, which is basically a polymeric coating on a glass substrate. It is specially designed to have low transmission (high reflectivity) at the laser wavelength and high transmission at all other wavelengths. Then, the exciting laser beam is focused on the sample through a microscope objective. The scattered light is then collected by the same objective and passed through the notch filter, with the Rayleigh-scattered light being rejected, which allows an important gain in sensitivity. The rejection ratio for a single filter can be as high as 10^6, which allows a small single-stage spectrometer to be used in place of the double- and triple-grating used a few years ago. Indeed, the main difficulty of Raman spectroscopy is to detect the weak inelastically Raman scattered light from the intense background due to the Rayleigh scattered light. Holographic notch filters typically permit Raman spectral measurements of frequency shifts greater than $\sim$100 cm^{-1}.

3. The spectral analysis system and the detector. The polychromatic light beam collected by the objective of the Raman microprobe has to be analyzed by a spectrometric system. When Raman scattered photons enter the spectrograph, they propagate through a transmission grating to separate them by wavelength and are collected by a detector which records the intensity of the Raman signal at each wavelength. Significant advances in Raman spectroscopy have been afforded by the development of detectors, evolving from photographic plates to photoelectric tubes, photon counting, and various forms of multichannel detectors: photodiode arrays (PDA) and, more recently, charge coupled device (CCD) cameras. These little integrated circuit chips are extremely sensitive to light and contain thousands of little picture elements (called pixels) that take the whole spectrum at once in less than a second. The high detectivity of CCD detectors allows the use of very low laser power, in order to prevent thermal or photochemical destruction of the sample.

4. Finally, an acquisition electronics allows the scanning, the collection, and the processing of the data.

2.3. Advantages and Limitations of Raman Microspectrometry for the Study of Electrode Materials for Lithium Batteries

Since Raman microscopy is an optical spectrometry, it has several characteristics very well suited to the study of electrode materials. First, under careful excitation conditions, the analysis is nondestructive. The analysis causes neither damage nor alteration, so it is possible to continue the investigation of the same electrode material, even on the same spot, with another laser wavelength or with another technique.

Raman experiments can be performed without sample preparation. Neither special coating nor a controlled atmosphere is necessary. As Raman is relatively unaffected by strong IR absorbers such as water, CO_2, and glass (silica), no special accessories are needed for aqueous solutions. The visible excitation source can penetrate transparent container materials, and thus, Raman measurements can be acquired through glass vials, envelopes, plastic bags, and several other packaging materials. This characteristic facilitates the development of experimental devices, allowing *in situ* Raman investigations of electrode materials under operation. This is especially desirable when exposure to atmosphere might change some of a material's bulk and/or surface properties.

If the low sensitivity of Raman spectroscopy had long been a major limitation, the detectors have been tremendously improved and it is now possible to obtain the spectra of various kinds of electrode materials (composite electrodes, thin films, single particles, powders, electrode/electrolyte interfaces, electrolytes, thin films, ...) on a microspot in a few tens of seconds.

A significant advantage is the capability to focus the excitation beam on a very small spot, whose diameter depends on the selected laser wavelength and the aperture of the objective, typically $\sim$1 μm. Such a spatial resolution is required by the heterogeneous character of electrode materials used in lithium batteries. Because the surfaces of the composite electrodes typically contain one or two types of carbon and/or and oxide, a binder, and occasionally an additive, Raman microspectrometry is a very suitable technique, as it allows heterogeneous mixtures to be analyzed, with a lateral resolution at the electrode surface corresponding to a typical particle size of a few micrometers. Information about the local structure and chemical composition of each component may therefore be provided individually. Furthermore, as confocal Raman microspectrometry is able to analyze very small volumes on the order of the cubic micrometer, it is possible to perform Raman imaging from point by point analysis. Hence, two- or three-dimensional chemical or structural mapping can be produced with a micrometric resolution. Another advantage provided by confocal Raman spectroscopy consists in a true "optical sectioning" of the sample, because the confocal mode allows the Raman light coming from the focal plane at the sample to be selected. Spatial resolution of $\sim$1 μm^3 can be achieved, which allows the different elements of a working battery to be investigated (anode, cathode, electrode/electrolyte interface).

Raman spectroscopy is the technique of choice for the characterization of carbon-based materials used in lithium ion batteries. This property comes from the fact that the scattering efficiency gets larger when the laser energy matches the energy between optically allowed electronic

transitions in the material. This intensity enhancement process is called resonance Raman scattering.

In opaque materials, an interesting point concerns the axial resolution, determined by the optical skin depth (δ) of the laser beam, whose value is approximately 30−300 nm. The skin depth (δ) is directly related to the electronic conductivity, σ, the magnetic permeability, μ, and the laser wavelength, λ, through the following equation: $\delta = (2\lambda/\mu\sigma)^{1/2}$. Hence, an increase in the electronic conductivity will result in reduction of the optical skin depth. For example, in the case of highly oriented pyrolytic graphite, Raman spectroscopy allows us to examine phenomena within a skin depth of about 50−100 nm with a 514.5 nm green laser beam.[34]

Raman spectroscopy is a well suited technique for the characterization of the local structure in transition metal oxides used as positive (or negative) electrode materials in lithium and lithium ion batteries. From an analytical point of view, the Raman spectroscopy technique can solve the problem of phase identification when various environments are present. Indeed, the wavenumbers and relative intensities of the Raman bands are very sensitive to the crystal symmetry, coordination geometry, and oxidation states. For example, it is possible to differentiate various kinds of metal oxides whose atomic arrangements are closely related to one another, to distinguish between different metal oxide compounds having the same elementary analysis, such as manganese oxides MnO_2, Mn_3O_4, Mn_2O_3, or between compounds with the same stoichiometry but different crystalline structures, such as anatase and rutile TiO_2 or cubic and hexagonal $LiCoO_2$.

Since it does not need a long-range structural order, Raman spectroscopy also constitutes an alternative structural tool, as it allows the study of "amorphous" compounds, thin films, or cycled cathode materials which exhibit poor XRD information due either to their low crystallinity, their preferential orientation, or structural disorder.

From a more fundamental point of view, Raman spectroscopy constitutes a local probe of great interest, complementary to long-range structural techniques such as X-ray or neutron diffraction, to study the cathodic material under or after operation. The determination of frequencies of normal vibrations provides various useful data on the local structure variations induced by the lithium insertion deinsertion process in the lattice host, e.g. changes in metal−oxygen bond lengths, metal oxidation state, lithium environment, lattice distortions, disorder, lithium−lithium interactions, lithium−host lattice interactions, and cation ordering. Furthermore, the use of high resolution Raman microscopy mapping allows the identification of the local processes that contribute to the electrode capacity loss, through the analysis of the surface composition and distribution. This type of information is of great interest insofar as the processes that occur on a microscopic scale can be directly linked with the macroscopic behavior.

The main limitation of Raman spectroscopy is the difficulty in making this technique quantitative, due to the experimental effort needed to measure and calibrate the Raman band intensities, due to the small surface it probes, and due to the fact that its sensitivity strongly depends on the polarizability of the analyzed molecules. This yields, for example, an extremely good capacity to detect minimal amounts of anatase and rutile (TiO_2) and on the other hand a very low sensitivity toward manganese dioxide (MnO_2). It is also not a suitable technique for the analysis of metallic compounds, as nearly all pure metals are Raman silent, and some materials are quite unstable under the local heating due to the exposition to the laser light. Fluorescence (much more intense than the Raman signal) can also limit Raman usefulness. Background fluorescence occurs often in impurities or organic materials of the sample (typically fluorescence of the electrolyte). This problem can be partly solved by changing the laser wavelength in order to separate the Raman and the fluorescence spectra, since electronic fluorescence is excited by a specific wavelength.

2.4. Advanced Experimental Approaches for Raman Characterization of Lithium Battery Components

These whole characteristics have prompted the *in situ* application of Raman spectroelectrochemistry and stimulated the emergence of novel experimental approaches during the past decade. The ability to spatially and temporally probe working lithium batteries with Raman spectroscopy might provide another opportunity for researchers to experimentally verify theoretical models used to simulate the lithium ion dynamics.

The first *in situ* Raman spectroscopic studies in an operating lithium rechargeable battery focused on the intercalation of lithium ions into various oxide-based cathodes (e.g., Li_xCoO_2, $Li_xMn_2O_4$, and $Li_xV_2O_5$)[35−37] and graphitic anodes.[38−43] Rey et al. demonstrated the successful application of confocal Raman microspectrometry for *in situ* characterization of a lithium battery that consisted of a Li metal anode, a $P(EO)_{20}LiN(SO_2CF_3)_2$ polymer electrolyte, and a V_2O_5 cathode.[44,45] The authors could detect structural changes in the V_2O_5 cathode, concentration gradients in the polymer electrolyte, and contaminating agents that formed at the lithium−electrolyte interface. An innovative application of Raman microscopy was presented in several studies reported by Panitz and Novak,[43,46−48] who used Raman surface mapping to generate local surface composition images of 30×35 μm^2 areas (at 2 μm lateral resolution) of $LiCoO_2$ positive and carbon negative electrodes from commercial lithium batteries. The mapping technique application of Raman microscopy has provided unique insight into the mechanisms of specific chemical or electrochemical processes that may be responsible for the cell degradation, as demonstrated by the numerous works reported by Kostecki et al. on positive[49−54] and carbon negative[55,56] electrodes used in Li ion and high power Li ion cells. *In situ* simultaneous spectroscopic and electrochemical measurements on single particle electrodes were successfully performed by Scherson et al.,[57−60] who collected high quality, time-resolved Raman spectra as a function of the applied potential from single particle graphite electrodes embedded in thermally annealed Ni foils[57] as well as single particles of $LiMn_2O_4$ isolated in a microelectrode.[58,59] The same group reported an *in situ* space- and time-resolved Raman spectromicrotopography experiment of an operating lithium ion battery.[60] This arrangement enabled Raman spectra to be collected continuously from a sharply defined edge of the battery exposing the anode, separator, and cathode, during charge and discharge. Clear evidence was obtained regarding the state of charge of graphite particles within the anode and, to a lesser extent, of $LiCoO_2$, during battery discharge as a function of both position and time. More recently, Kostecki et al.[61] proposed an experimental approach enabling inves-

tigation of the *in situ* spectroscopic behavior of several individual $LiNi_{0.8}Co_{0.15}Al_{0.05}O_2$ particles in composite cathodes during a galvanostatic charge/discharge cycle while Migge et al.[62] performed confocal Raman spectroscopy on a specially designed button cell to study the intercalation of lithium into single particle graphite electrodes. Burba et al.[63] lately described a modification to industrially available coin cells to facilitate routine *in situ* Raman spectroelectrochemical measurements of electrodes in lithium batteries. The authors tested their strategy on $Li//V_2O_5$ cells. This approach is of importance for researchers to easily construct cells for *in situ* spectroscopy in addition to cells that are used in normal electrochemical evaluations.

3. Lithium Metal and Carbon-Based Electrodes

3.1. Lithium Metal Anodes

The lithium metal electrode is of great interest to battery researchers because of its high theoretical specific capacity. To date, however, problems associated with the reversibility of the deposition-dissolution process at the interface have prevented its successful application in secondary batteries for commercial purposes. The poor reversibility is due to nonuniform current density across the lithium surface under electrochemical operation. This limitation has been related to the formation of an inhomogeneous film on the metal surface. The film, known as the solid electrolyte interphase (SEI), is composed of various reduction products, which result from reaction between lithium and the electrolyte solution.[64] Charge–discharge cycling of the electrode requires the transport of lithium ions through the inhomogeneous film, which results in irregular deposition (charging) or dissolution (discharging) at the electrode surface and subsequent "dendritic deposition" of Li, which limits the cyclability of the Li electrode.[64]

Raman investigation on the lithium metal/electrolyte interface in an attempt to identify the passive surface film has so far been unsuccessful. A few Raman studies performed on the electrolyte itself have nevertheless allowed the identification of species present in the electrolyte and near the electrode surface,[38,65] the characterization of the local structure of solvated lithium cations,[66,67] and the access to the transport properties in polymer electrolytes through the concentration profiles obtained from *in situ* confocal Raman microspectrometry experiments.[44,45] A sealed lithium optical cell was specially designed and tested, with the aim to investigate alternative electrolyte systems for use with lithium metal electrodes.[68] The authors reported optical images of lithium surface deposits and *in situ Raman* spectra arising from both the electrolyte and the deposits formed during charge–discharge cycling of lithium metal electrodes. Nevertheless, the authors were not able to confidently assign the Raman peaks corresponding to the deposited species.

Researchers have employed a wide range of techniques to study the processes which occur on the lithium surface. The surface chemistry of lithium in organic electrolytes has been investigated using (FTIR) spectroscopy, EDAX, and XPS.[69] The results showed that solvents, such as propylene carbonate (PC), were decomposed on lithium and formed surface films of lithium alkylcarbonate, $ROCO_2Li$, and that the lithium surface consisted of Li_2CO_3, LiOH, Li_2O, and lithium halides. Raman studies focusing on the lithium anode are scarce. Indeed, as far as the characterization of the surface is concerned, the sensitivity of normal Raman is rather

limited, since Raman signals are only obtained after a degradation reaction has occurred.[70] Because surface-enhanced Raman scattering (SERS) provides an increase of sensitivity as a result of the large enhancement effect (up to a factor 10^7), this technique has been more helpful in identifying the SEI on an Ag anode through the formation of a nanometer-scale islandlike Li–Ag alloy on the electrode surface.[71] These experiments have allowed the detection of LiOH, H_2O, and Li_2CO_3 as the main stable species of the SEI film on the surface of the Ag electrode discharged in 1 M $LiPF_6$/EC-DEC electrolyte.[72]

3.2. Carbonaceous Materials

Carbon-based materials have received considerable attention as negative electrodes,[73] because they constitute good alternatives to solve the problem of cycle life and safety raised by the use of metallic lithium. Indeed, graphite serves as a host structure for lithium intercalation and the structure is resilient enough to provide reversibility by allowing easy insertion and deinsertion of lithium. Graphite exists in various forms ranging from a crystalline state to an almost amorphous state. The raw materials used to produce carbon anodes include natural graphite, oil pitch, coal tar, hydrocarbon gas, benzene, and various resins. In practice, at room temperature, graphite accepts sufficient lithium to form LiC_6, which on delithiation can deliver 372 (mA h)/g.[73] The relation between the electrochemical features of Li intercalation into various carbon-based materials and their crystal structure has been described in detail.[74] Before focusing on the Raman contribution to the study of carbon electrode materials, we present some salient aspects of the vibrational features of carbons.

3.2.1. Raman Spectra of Carbons

From a structural point of view, hexagonal graphite consists of stacked sheets with the carbons within the layers arranged in a two-dimensional network of regular hexagons. It crystallizes in the D_{6h}^4 space group and has two doubly degenerate Raman-active modes,[75] both vibrating in the plane of the sheets, E_{2g1}, at 42 cm^{-1}, and a strong C–C stretching mode, E_{2g2} (G-band), at 1582 cm^{-1}. Figure 3 shows the sharp intense band at 1580 cm^{-1} observed for a natural graphite crystal and HOPG. Because of the weak interlayer bonding, graphite crystals are subject to disorder along the *c* axis while, at the same time, the strong intralayer carbon–carbon bonding maintains a high degree of order within the individual carbon sheets. This so-called turbostratic disorder strongly influences the Raman features. Hence, in addition to these allowed two lines, many kinds of graphite materials exhibit a disorder-induced A_{1g} line (D-band) at about 1350–1360 cm^{-1}. Figure 3 illustrates the typical Raman features observed for polycrystalline graphite, with the 1357 cm^{-1} band appearing for well-crystallized graphite with small particle size but not with large grain single crystals. This mode has been linked to the break of symmetry occurring at the edges of graphite sheets originating from some kind of imperfection and disorder, such as defects, discontinuity in crystallites, and stacking disorder in the crystal structure of graphite.[75] The line width and D/G band intensity ratio vary depending on the structure of the carbon (Figure 4). Several authors[10,75] have found a linear relationship between the inverse of the intraplanar microcrystallite dimension L_a and the ratio of the intensity of the disorder-induced D-line to that of the Raman-active E_{2g2} G-line, I_D/I_G, denoted R.
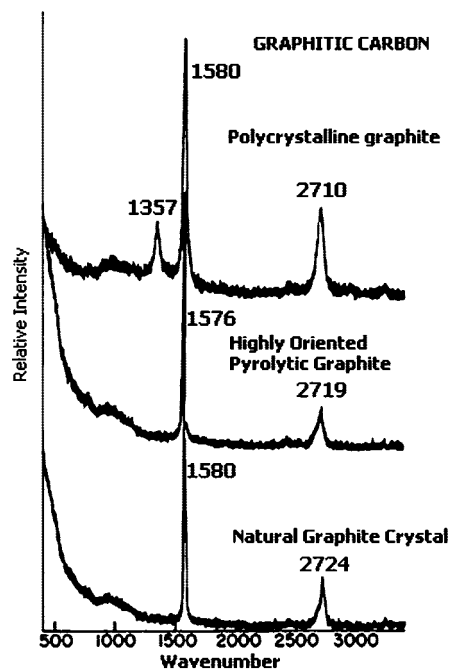
Figure 3. Raman spectra of various graphitic carbons, recorded using a laser excitation line of 514.5 nm. Reprinted with permission from ref 10. Copyright 1989 Materials Research Society.
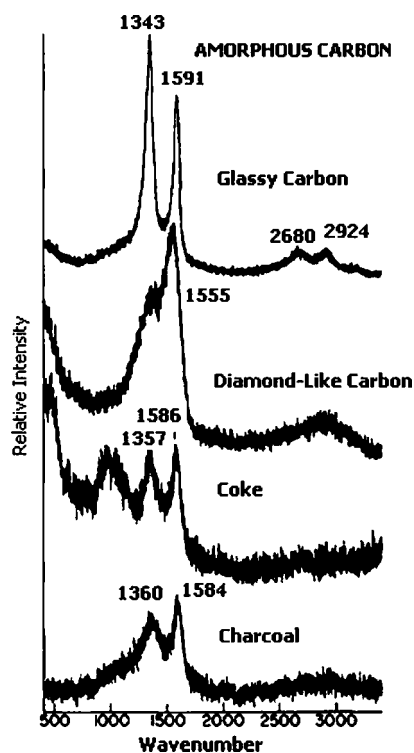
Figure 4. Raman spectra of various noncrystalline carbons, recorded using a laser excitation line of 514.5 nm. Reprinted with permission from ref 10. Copyright 1989 Materials Research Society.

From the value of R, the crystallite size along the a-axis, L_a, can be calculated according to the equation of Tuinstra and Koenig: $L_a \approx 4.4/R$ [nm]; however, this equation, originally developed for an excitation wavelength of 488 nm, must be taken cautiously, as Raman intensities of carbonaceous materials have been found to depend on the excitation wavelength. As a matter of fact, Mernagh et al.[76] have investigated the Raman spectrum of carbon black and found that the R value depends on the laser energy E_{laser} used for

Table 1. Raman Frequencies (ω) and Widths (Γ) for High Frequency Graphitic Bounded- and Interior-Layer Phonons for Stage 1−3 Li-Graphite[a]

compd	temp (K)	stage	ω (cm^{-1})	Γ (cm^{-1}) (fwhm)
LiC$_6$	300	1	1596 ± 2	35 ± 4
LiC$_6$	300	1	1594 ± 3	48 ± 4
LiC$_{12}$	300	2	1592 ± 2	33 ± 5
LiC$_{17}$	300	2	1598 ± 2	28 ± 3
LiC$_{17}$	300	2	1604 ± 4	33 ± 4
LiC$_{12}$	240	2	1590 ± 3	33
LiC$_{18}$	240	3	1602 ± 2	20 ± 4
			1577 ± 2	20 ± 3

[a] Reprinted with permission from ref 93. Copyright 1987 the American Physical Society.

the Raman excitation. This strong dependence of the R value upon the laser wavelength has been further observed in many different graphitic materials, amorphous-C materials,[77] polished glassy carbon samples,[78] pyrolytic graphites,[79] carbon nanotubes,[80] disordered graphite,[81] graphite edges,[82] as well as carbon foams.[83] The complete understanding of the intensity dependence of the D-band in graphitic materials as a function of E_{laser} and L_a is of fundamental importance, since Raman spectroscopy is one of the preferred tools for the characterization of graphitic carbons. Vidano et al.[84] performed a systematic investigation of the Raman spectra of different kinds of carbon materials by varying the laser excitation wavelength, and they observed that the wavenumber value of the disorder-induced D-band also varies linearly with increasing E_{laser}, with the slope of this dependence being $\partial \omega_D / \partial E_{laser} \simeq 50$ cm^{-1}/eV. The laser energy dependence of the D-band frequency was observed in many different graphitic materials, and the slope of this dependence was observed to be independent of the material type.[78] The first attempt to explain the dispersive behavior in the frequency of the D-band was presented by Baranov et al.,[85] who proposed that this band originates from a double resonance (DR) Raman process in graphite. This concept was further developed by Thomsen and Reich,[86] who calculated the scattering cross section for the double resonance mechanism that gives rise to the D-band. Despite the fact that the dispersive behavior of the D-band frequency has been successfully understood by the DR mechanism, the strong E_{laser} dependence of the ratio I_D/I_G is still an open problem and there is not yet a theory that explains the dependence of the ratio I_D/I_G on the crystallite size L_a.[87]

3.2.2. Graphite Intercalation Compounds

Because Raman spectroscopy is a pertinent tool for the study of ion insertion into carbonaceous materials, many groups have studied the Raman spectra of graphite intercalation compounds (GICs).[88−93] The most important property of graphite intercalation compounds is the staging phenomenon, which corresponds to intercalate layers that are periodically arranged in a matrix of graphite layers. The stage index, n, denotes the number of graphite layers between adjacent intercalate layers. Li-intercalated graphite is an example of a donor GIC, with the lithium layers donating electrons to the graphitic carbon layers, and different phases have been reported: stage-1 LiC$_6$, stage-2 LiC$_{12}$ and LiC$_{17}$, stage-3 LiC$_{18}$, and stage-4 LiC$_{27}$.[93] Table 1 summarizes the main features reported for stage 1−3 Li-graphite.[93] Intercalation of guest species into a host structure of carbon strongly affects the position, shape, and intensity of the E_{2g2} band at 1582 cm^{-1}. A Raman doublet is observed for GICs with stage

$n > 2$, at wavenumbers close to the singlet E_{2g2} of pristine graphite.[88−93] The lower wavenumber component $E_{2g2}(i)$ (around 1580 cm^{-1}) corresponds to graphitic layers not adjacent to intercalate layer planes (named "interior layers") whereas the upper wavenumber component $E_{2g2}(b)$ (around 1600−1610 cm^{-1}) corresponds to graphite layers adjacent to intercalate layer planes (named "bounded layers"). For $n \leq 2$, only bounded carbon layers exist, and a single Raman line is observed, around 1600 cm^{-1} for stage-1 LiC_6. Whereas LiC_x phases are difficult to detect by X-ray diffraction owing to the very weak intensity of the ($hk0$) diffraction peaks, Raman spectrometry is a pertinent tool to determine the stage of the Li intercalation process in carbonaceous materials through the analysis of the shape, the frequency shift, and the relative intensity of the Raman features in the 1570−1620 cm^{-1} range.[89]

3.2.3. Carbon-Based Anodes for Lithium Ion Batteries

Numerous works are devoted to the Raman study of lithium intercalation into carbon-based anode materials. Spectroscopy experiments have been conducted either in *ex situ*[38,55,56,94,95] or *in situ*[39−43,57,60,62,96−98] conditions, on different kinds of carbons: highly oriented pyrolitic graphite (HOPG), natural graphite, cokes, carbon fibers, synthetic high temperature graphite, multiwall carbon nanotubes (MWNTs), or spherical mesocarbon microbeads (MCMBs). Much information has been drawn from the observation of the Raman features: the nature of the lithium intercalated phases, the local distribution of lithium across the surface of graphite or carbon particles, the degree of surface structural disorder on graphitic anodes, the stability of the carbon-based material during electrochemical cycling and aging, etc.

During an *in situ* Raman study of the electrochemical lithium insertion into the HOPG electrode, Inaba et al.[39] showed spectral changes associated with phase transitions corresponding to different staged LiC_{27} ($n = 4$), LiC_{12} ($n = 2$), and LiC_6 ($n = 1$) phases, occurring reversibly during a charge and discharge cycle. The authors observed that the electrode potential was determined by the "surface stage" of graphite intercalation compounds. Recent advances in Raman spectroscopy in the latest years have made it possible to study the dynamic aspects of Li intercalation−deintercalation into single carbon particles embedded in thermally annealed Ni foils,[57] using *in situ*, time-resolved Raman microscopy. By analyzing the position of the prominent G band, the authors were able to determine spectroscopically and in real time the average concentration of Li$^+$ within the volume of the particle probed by the laser beam all along the electrochemical lithium deintercalation process. More recently, Migge et al.[62] used *in situ* confocal Raman microspectroscopy to investigate the first cycle of lithium intercalation−deintercalation into single graphite particles. During the first charge of the battery, they found the typical spectroscopic fingerprints of the LiC_{27}, LiC_{12}, and LiC_6 phases. However, the intercalation process was not homogeneous, even in single graphite particles, depending on various parameters of the working battery, such as current density, electrolyte, and temperature. Raman studies of the electrochemical Li intercalation into mesocarbon microbeads (MCMBs) heat treated at different temperatures[40] and multiwall carbon nanotubes (MWNTs)[94] revealed the same intercalation mechanism in the case of MCMBs heat treated at 2800 °C; that is, lithium is inserted between graphene layers via stages of GIC formation. Conversely, for MCMBs heat treated at 1800

and 1000 °C and MWNTs, the authors reported a random Li insertion without the formation of staged phases.

Several works have demonstrated that Raman microscopy constitutes a very convenient diagnostic tool to estimate the surface structural changes occurring on graphitic materials.[47,55,56,95,99−105] Indeed, a quantitative characterization of the degree of surface disorder can be obtained from the analysis of the Raman bands observed at 1357 and 1580 cm^{-1}. These studies have shown that several parameters such as sample preparation, surface modification, heat treatment, and cell operating conditions, greatly influence the surface crystallinity and, hence, the electrochemical performances of carbon-based anodes[47,55,56,95,99−101,104,105] and carbon-coated $LiFePO_4$ cathodes[102,103] for Li ion batteries. In the course of the understanding of the graphite disordering mechanism, Kostecki et al. used Raman microscopy and atomic force microscopy (AFM) to study the effect of structural changes which occur in graphitic materials during Li ion cell cycling at ambient and elevated temperatures.[55,56,104] The authors evaluated the near-surface and surface changes resulting from the exposure of graphitic electrodes to stresses associated with elevated temperature and numerous Li intercalation−deintercalation cycles, in terms of graphite structure disordering and SEI layer morphology, thickness, and composition change. By applying high resolution Raman microscopy mapping, a nonuniform gradual structural degradation process was found in graphite upon cycling at 60 °C. The authors also detected the formation of nonhomogeneous electrolyte decomposition products within the bulk of the anode. The Raman data were found to be in good correlation with the corresponding experimental electrochemical data, indicating an increase of cell impedance and a loss of reversible capacity. A nonuniform current density distribution was thought to be responsible for large Li concentration gradients within the crystalline structure of graphite eventually surpassing the tensile stress of graphene planes. The authors suggested that the gradual disordering of the graphite anode during prolonged cycling leads to the fragmentation of surface graphene and subsequent continuous SEI layer reformation reducing the reversible capacity of the cell.[55,56]

It is well-known that the electrochemical behavior of the carbon anode depends not only on the type of carbon materials but also on the solvent and electrolyte system used in batteries. A prominent example is the incompatibility of propylene carbonate (PC) electrolytes with highly crystalline graphite materials. During the electrochemical insertion of Li$^+$ in such electrode materials from PC-based electrolytes, the graphite structure exfoliates, leading to severe battery failure.[69,95,106] An *in situ* Raman study of the graphite surface structure revealed drastic Raman spectral changes in the high potential range during the first discharge process in $LiClO_4$ EC/DME solution, where large irreversible capacity losses take place.[41] Frech et al.[41] suggested that this alteration of the graphite surface structure corresponded to extensive graphite exfoliation caused by solvent cointercalation with lithium ions and subsequent decomposition. Hardwick et al.[98] recently used *in situ* Raman microscopy to compare the stability in PC of two microcrystalline graphites with different grain sizes (3 and 24 μm) toward exfoliation. A split of the G-band at higher wavenumber was detected only for the sample with larger crystallite size and the largest
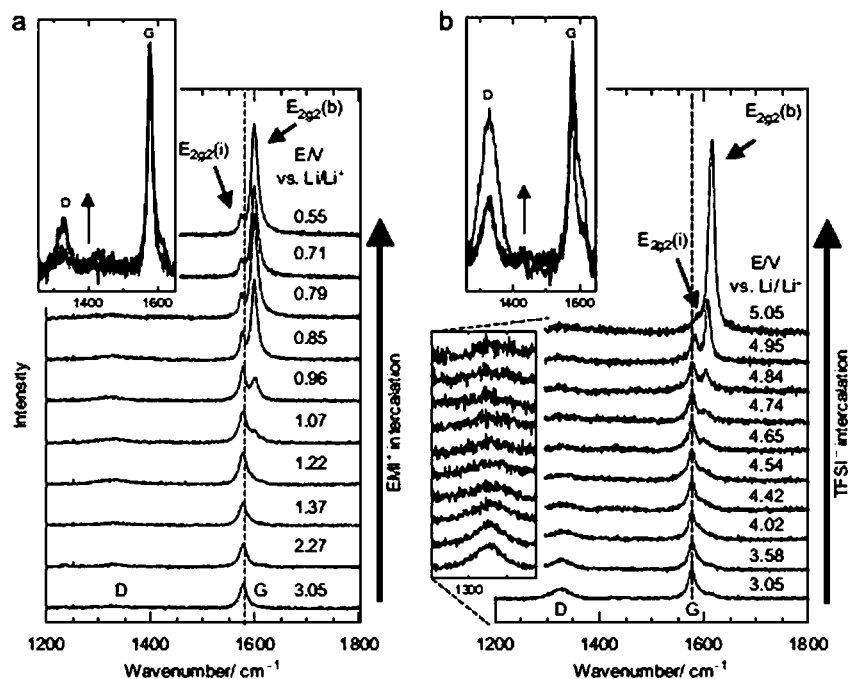
Figure 5. *In situ* Raman spectra series of the first (a) EMI^+ and (b) $TFSI^-$ intercalation into graphite. Insets in the figure show Raman spectra before (bold line) and after (thin line) one cycle. Laser excitation line: 632.8 nm. Reprinted with permission from ref 97. Copyright 2008 Elsevier.

irreversible charge loss, indicating the presence of solvated ions intercalated into graphite. This spectral change was associated with the beginning of the exfoliation process. *In situ* Raman microscopy was also newly used to demonstrate large cation (EMI^+) and anion ($TFSI^-$) intercalation into microcrystalline graphite during cyclic voltammetry experiments from the ionic liquid (EMI-TFSI).[97] The Raman spectral series (Figure 5) clearly displays, with the split of the G-band at 1578 cm^{-1}, the intercalation of these ions into graphite. From the analysis of the intensity ratio $E_{2g2}(i)/E_{2g2}(b)$, Hardwick et al.[97] show that GICs between stages 2 and 3 were formed at the potential limits of 0.55 V for (EMI^+) and 5.05 V vs Li/Li$^+$ for ($TFSI^-$). Furthermore, a significant increase in the I_D/I_G ratio is observed after both the anodic and cathodic cycles, which indicates graphite deterioration on anion intercalation. Such a result may have a negative impact for the use of ionic electrolytes when carbon additive is used as conductive agent at the high voltage cathode.

4. Transition Metal Oxide-Based Compounds

We intend to present here a review of the most prominent data reported for various metal oxide-based materials, which have been selected in order to highlight the contribution of Raman spectroscopy in the area. The results of these studies have provided a better understanding of the different processes responsible for the loss of electrochemical performance, which constitutes a key step to have an idea about improving the electrode material. Particular attention will be paid to the $Li_xV_2O_5$ and the Li_xTiO_2 systems, for which a thorough analysis has been provided using Raman microspectrometry thanks to a careful and rigorous experimental approach combined with a theoretical analysis based upon lattice dynamics simulations.
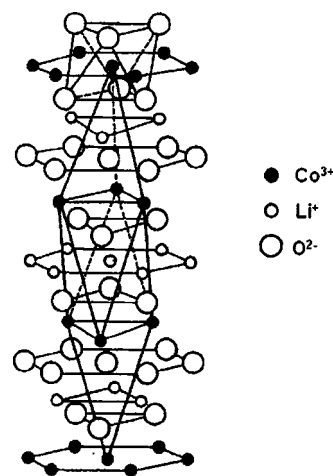

Figure 6. Crystal structure of α-NaFeO$_2$-type compounds.

4.1. Lithium Cobalt Oxide LiCoO$_2$

This cathodic material deintercalates lithium at a very high voltage, ca. 4 V vs Li/Li$^+$. Three basic lithiated systems (as well as their substitutive derivative forms) with high operating voltage are presently known. These are $LiCoO_2$ and $LiNiO_2$ with the pseudolayered α-NaFeO$_2$ structure, and the 3D spinel $LiMn_2O_4$. To improve their electrochemical properties, the mixed compounds resulting from various substitutions on the transition metal site have been investigated in these structures.

In 1980, Mizushima et al.[107] proposed using layered $LiCoO_2$ with the α-NaFeO$_2$ structure as an intercalation cathode. It took around 10 years to put $LiCoO_2$ to commercial use. This oxide is now mainly used as the cathode material in commercial lithium ion batteries.[108] The layered structure of $LiCoO_2$ is shown in Figure 6. $LiNiO_2$, $LiCrO_2$, and $LiVO_2$ also adopt this structure. These $LiMO_2$ compounds, prepared at temperature ranges of 700−900 °C, are rock salt-structured materials based on a close-packed network of oxygen atoms with Li^+ and M^{3+} ions in octahedral interstices in this
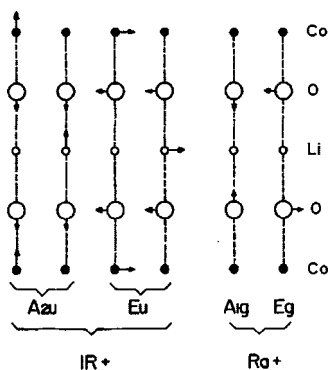
Figure 7. Atomic displacements of the IR and Raman-active modes of hexagonal ($R\bar{3}m$) LiCoO$_2$.

packing in alternating (111) planes. This (111) ordering introduces a slight distortion of the lattice to hexagonal symmetry.

LiCoO$_2$ crystallizes in the hexagonal ($R\bar{3}m$) space group (D_{5}^{3d}) with a unit cell consisting of one formula unit ($Z = 1$) and unit cell parameters $a_{hex} = 2.82$ Å and $c_{hex} = 14.08$ Å. The atoms of the LiCoO$_2$ units are on sites with symmetries and coordinates given below:

Co:	(3a, D_{3d})	0, 0, 0	
Li:	(3b, D_{3d})	0, 0, $^{1}/_{2}$	
O:	(6c, C_{3v})	0, 0, u	0, 0, $\bar{u}$

By factor group analysis, the total irreducible representation for the vibrational modes of LiMO$_2$ is obtained as A$_{1g}$ + 2A$_{2u}$ + E$_g$ + 2E$_u$. The *gerade* modes are Raman-active, and the *ungerade* modes are IR-active. The two Raman-active modes are especially simple. In the A$_{1g}$ mode, two adjacent oxygen layers move rigidly against each other and parallel to the c axis, whereas the atomic displacements in the E$_g$ mode are perpendicular to the c axis (Figure 7).

The Raman spectrum of LiCoO$_2$ was first reported by Inaba et al.,[109] who studied the effects of replacing Co in LiCoO$_2$ by Ni. The Raman-active lattice modes were later assigned by the same team from polarized Raman measurements on a c-axis oriented LiCoO$_2$ thin film.[110] Two Raman-active modes have been found, which correspond to oxygen vibrations involving mainly Co−O stretching, ν_1(A$_{1g}$) at 595 cm^{-1}, and O−Co−O bending, ν_2(E$_g$) at 485 cm^{-1}.

The mechanism of lithium deintercalation and intercalation in LiCoO$_2$ has been investigated using XRD.[108,111,112] The discharge curve and the lattice parameters changes in bulk Li$_{1-x}$CoO$_2$ are shown in Figure 8. The a axis remains practically constant, whereas the c axis increases from ≈14.08 to 14.45 Å for $0 < x < 0.5$, due to the production of a second hexagonal phase with an expanded c parameter.[108] The expansion in the c axis has been ascribed to an increase in the electrostatic repulsion between adjacent CoO$_2$ layers because negatively charged oxygen−oxygen interactions increase with the removal of lithium ions.[112] Two monoclinic phases were also reported, one at about $x = 0.45$, and another for $0.75 < x < 1$.[108] One single study reports the Raman spectra of Li$_{1-x}$CoO$_2$ powder prepared by electrochemical lithium deintercalation.[110] The spectral changes were well correlated with the structural changes determined by X-ray diffraction, namely as a series of phase transitions. In particular, a set of two new bands, located at lower wavenumbers, are observed for the second hexagonal phase (Figure 9). These downward shifts of both bands have been

found in good agreement with the increase of the c-axis length as lithium ions are deinserted. However, the expected Raman peak splitting due to the distortion in the monoclinic phase was not observed. *In situ* Raman spectroscopy has also been conducted on thin film electrodes of pure LiCoO$_2$.[35,113] An interesting feature concerns the reported invariance of the peak frequency with the electrode potential,[35] which is not discussed by Itoh et al. but can be correlated to the specific structural response of a LiCoO$_2$ thin film reported later by Kim et al.[114] from XRD measurements on thin films, that is different from the structural behavior usually known for the LiCoO$_2$ powder. Indeed, when the cutoff voltage is limited to the conventional value of 4.2 V corresponding to the Li$_{0.5}$CoO$_2$ material, the XRD patterns of charged films at 4.2 V showed negligible change in the c lattice parameter. Five or ten cycles are needed to induce the appearance of the conventional Li$_{0.5}$CoO$_2$ expanded phase observed from the first charge for the bulk material. In another work, Itoh et al.[113] reported that applying potentials more positive that 4.7 V leads to a sudden increase of the Raman background signal which was ascribed to the formation of a film on the LiCoO$_2$ electrode surface in organic solution (LiClO$_4$/PC or EC).

Micro-Raman spectrometry constitutes a convenient and powerful technique for the qualitative microstructural analysis of LiCoO$_2$ cathodes. Because Raman spectroscopy is capable of detecting unambiguously the nature of the cobalt oxide phases present, lithiated or not, it has been extensively used for the characterization of powders[115−117] and thin film electrodes.[118−127] Considering the fabrication of the LiCoO$_2$ compound, especially when the thin film material is prepared at low temperature, Raman microspectrometry is thoroughly used as a quality control tool to check the nature and crystallinity of the LiCoO$_2$ active phase as a function of the synthesis conditions and to detect the presence of residual secondary phases, such as Co$_3$O$_4$ or Li$_2$CO$_3$.[118−127] An important point concerns the formation of the layered LiCoO$_2$ structure, which is known to be crucial for obtaining a good rechargeability of the cell. Indeed, a low temperature spinel LiCoO$_2$ phase (prepared at 400 °C and denoted as LT-LiCoO$_2$) has been reported, with different electrochemical features compared to the high temperature layered LiCoO$_2$ structure (prepared at 850 °C and denoted as HT-LiCoO$_2$).[115,128−130] Comparison of cyclic voltammetric curves for LT- and HT-LiCoO$_2$ emphasizes a large difference in the electrochemical behavior (Figure 10). The LT LiCoO$_2$ is characterized by unusual broad anodic and cathodic peaks with a difference between the peak potentials greater than 200 mV; these latter are located at 3.75 and 3.45 V. A faradaic yield around 0.4 F/mol is involved in both cases.

Standard powder neutron diffraction and X-ray diffraction cannot unambiguously distinguish between layered and spinel LiCoO$_2$.[128−131] Conversely, from a spectroscopic viewpoint, the ideal spinel type LiCoO$_2$ belongs to the space group *Fd3m*, for which the Bravais cell contains four molecules ($Z = 4$), and four Raman-active modes, A$_{1g}$, E$_g$, and 2F$_{2g}$, are predicted.[131] As shown in Figure 11, each LiCoO$_2$ crystal structure gives rise to a specific Raman fingerprint; that is, four Raman bands are observed at ca. 605, 590, 484, and 449 cm^{-1} for LT-LiCoO$_2$, whereas only two Raman bands at 597 and 487 cm^{-1} are observed for the layered HT-LiCoO$_2$.[131,132] This result is consistent with the theoretical prediction given for a spinel (*Fd3m*) and hexagonal ($R\bar{3}m$) crystal, respectively. These spectral disparities justify the
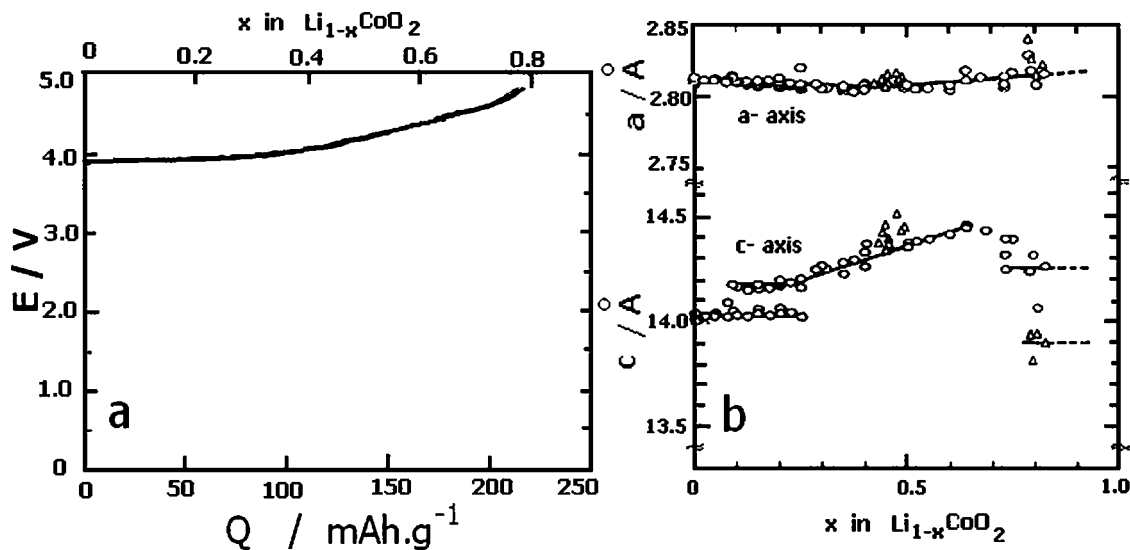
Figure 8. (a) Continuous charging curve of $Li_{1-x}CoO_2$ at a rate of 0.17 mA·cm^{-2} at 30 °C. (b) Lattice parameters of the hexagonal unit cell of $Li_{1-x}CoO_2$. Triangles indicate the converted unit cell parameters from the monoclinic cell. Reprinted with permission from ref 108. Copyright 1994 The Electrochemical Society.
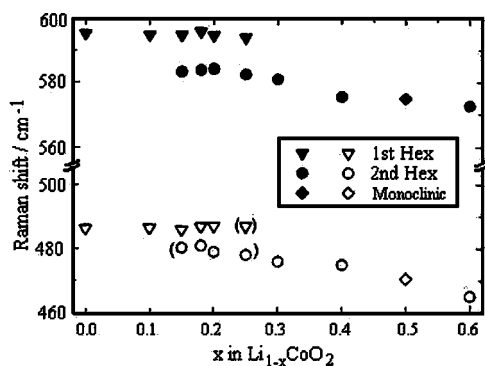

Figure 9. Variations of the peak wavenumbers of the upper (closed circles) and lower (open circles) Raman bands with x in $Li_{1-x}CoO_2$. Symbols in parentheses designate poorly fitted data. Excitation with 514.5 nm radiation. Reprinted with permission from ref 110. Copyright 1997 Wiley.
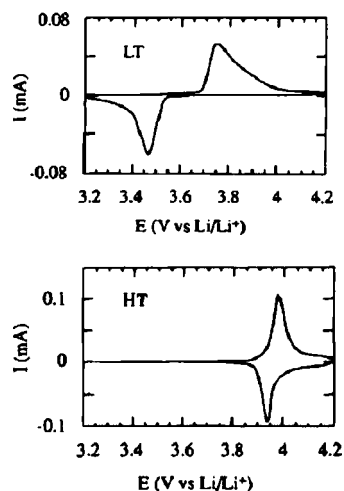
Figure 10. Cyclic voltammetric curves at 40 μV/s for HT-LiCoO$_2$ and LT-LiCoO$_2$. Reprinted with permission from ref 130. Copyright 1997 The Electrochemical Society.

systematic use of Raman spectroscopy for the structural determination of lithiated cobalt oxide phases. When used as a thin protective layer on the nickel cathode of a molten carbonate fuel cell (MCFC), LiCoO$_2$ is also of particular
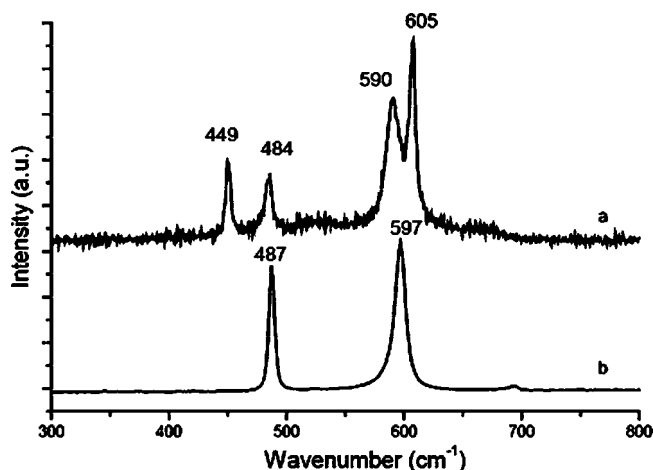
Figure 11. Raman scattering spectra for (a) spinel LT-LiCoO$_2$ and (b) layered HT- LiCoO$_2$. Excitation with 514.5 nm radiation. Reprinted with permission from ref 132. Copyright 2004 Elsevier.

interest due to its good mechanical resistance and low cost. In this field, Raman spectroscopy is also of interest, as it has allowed, for instance, obtainment of relevant information on the nature and stability of cobalt oxides layers when exposed to a second-generation electrolyte, $Li_2CO_3-Na_2CO_3$, at 650 °C,[132] showing the *in situ* formation of a cubic LT-LiCoO$_2$ thin layer, instead of the usually layered HT-compound reported in molten carbonate media.[133,134]

Over the past few years, attention has been focused toward application of Raman spectroscopy as an *in situ* vibrational probe of electrode materials in an operating Li ion battery during discharge−charge cycles. A specially designed *in situ* cell was developed by Novak et al.[46] with LiCoO$_2$ as cathode material and graphite as anode (Figure 12). This approach allowed access to the Raman signature of LiCoO$_2$ particles randomly selected on the surface of the commercial electrode. The authors observed that, upon lithium insertion into the host material, the background intensity rises significantly whereas, upon lithium deinsertion, the background intensity is nearly constant. These results were found in accordance with those reported earlier by Itoh at al. for a three electrode configuration.[35] More recently, *in situ* Raman measurements
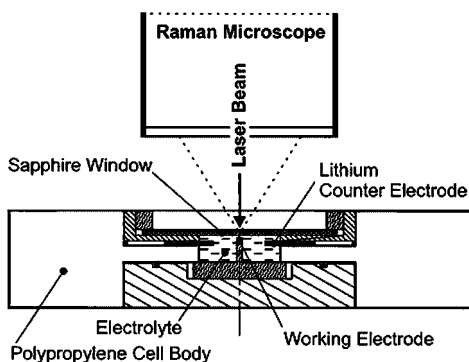
Figure 12. Example of an electrochemical cell developed for *in situ* Raman microscopy. Reprinted with permission from ref 46. Copyright 2000 Elsevier.
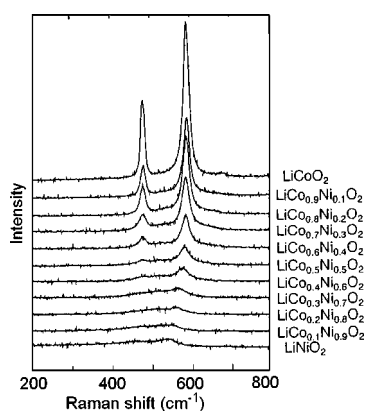
Figure 13. Raman scattering spectra of $LiNi_{1-y}Co_yO_2$ powder samples. Excitation with 514.5 nm radiation. Reprinted with permission from ref 109. Copyright 1995 The Chemical Society of Japan.

in an operating Li ion battery during discharge were carried out with the aim to construct time-resolved, two-dimensional maps of the state of charge within the electrodes.[60] However, if clear evidence was obtained for changes in the amount of Li^+ within particles of graphite during battery discharge, this effect was observed to a lesser extent for the $LiCoO_2$ cathode.

4.2. Lithium Nickel Oxide LiNiO$_2$ and Its Substitutive Derivative Compounds LiNi$_{1-y}$Co$_y$O$_2$ (0 < y < 1)

The limited capacity of $LiCoO_2$, its high cost, and toxicity are considered as drawbacks, especially for large scale applications. In order to overcome these problems, another layered compound of interest, $LiNiO_2$, has been investigated. However, this material suffers from a tendency to nonstoichiometry in relation with the presence of an excess of nickel[135] and from poor thermal stability in its highly oxidized state (Ni^{3+}/Ni^{4+}). Indeed, the metastable layered structure $Li_{0.5}NiO_2$ transforms into the cubic spinel on heating to 300 °C. The substitution of nickel by cobalt has been reported to be an easy way to stabilize the two-dimensional (2D) structure. The use of the solid solution $LiNi_{1-y}Co_yO_2$ (0 < y < 1), has therefore been explored, and improved electrochemical properties have been reported.[136] The Raman spectra of lithium–cobalt–nickel oxides have been reported by many authors.[109,131,137,138] It turns out that replacing Co by Ni does not change the space group, but both bands assigned to the E_g and A_{1g} Raman-active modes in ($R\bar{3}m$) symmetry are found to decrease drastically in intensity with increasing Ni content (Figure 13). Hence, the Raman scattering efficiency of $LiNiO_2$ appears to be very weak in comparison to that of other rock-salt compounds. The origin of these features was ascribed

to a reduction of the rhombohedral distortion by increasing Ni content or/and an increase in the electrical conductivity in $LiNiO_2$.[109] Conversely, the Raman spectrum of a PLD deposited $LiNi_{0.8}Co_{0.2}O_2$ film recently reported by Ramana et al.[139] exhibits intense features at 478 and 587 cm^{-1} which are not discussed by the authors, whereas they are contradictory toward previous data related with the same composition.[109] Another effect of cobalt substitution in $LiNi_{1-y}Co_yO_2$ powdered samples concerns the observed shift of both Raman bands toward higher frequencies, from 544 cm^{-1} in $LiNiO_2$ to 595 cm^{-1} in $LiCoO_2$ for the A_{1g} mode and from 465 cm^{-1} in $LiNiO_2$ to 485 cm^{-1} in $LiCoO_2$ for the E_g mode.[137] These frequency shifts are consistent with the observed decrease of the hexagonal unit cell parameters as the Co content increases (from 2.86 Å to 2.82 Å for the intralayer metal–metal distance a_{hex} and from 14.15 Å to 14.08 Å for the interlayer parameter c_{hex}) when y varies from 0.3 to 1.[138] It is suggested that the observed increase in vibrational frequencies with the cobalt content is related to the increase in the bond covalency inside the layers.

With the aim to better understand Li ion battery cell performances and the factors that limit battery lifetime, Kostecki et al. carried out several studies to characterize the degradation processes occurring on the surface of multisubstituted-based $LiNi_{1-y-z}Co_yAl_zO_2$-based electrodes during storage or electrochemical cycling under different conditions.[49–54,61,140–142] Using a set of microscale and nanoscale techniques (e.g., Raman microscopy, current-sensing atomic force microscopy, FTIR, XPS, EDX, XRD, NMR) coupled to the electrochemical analysis, the authors obtained maps yielding information about the chemical composition and structure of the electrode material. Raman microscopy mapping of $LiNi_{0.8}Co_{0.15}Al_{0.05}O_2$ composite cathodes harvested from high power Li ion cells showed that the surface distribution of carbon additives in these cathodes changes noticeably upon aging and/or cycling at elevated temperature[52] and also upon cycling over different depths of discharge.[53] The noticeable difference in the active material to carbon concentration ratio at the surface of the cathode was thought to be at least partially responsible for the observed power and capacity losses. Very recently, the same group put forward the nonuniform local kinetic behavior of individual oxide particles using *in situ*[61] and mapping Raman microscopy.[50] The micro-Raman spectra of the tested $LiNi_{0.8}Co_{0.15}Al_{0.05}O_2$ cathode[50] provided clear evidence of the inhomogeneous state of charge (SOC) of oxide particles on the cathode surface despite deep discharge of the Li ion cells at the end of the test. As shown in Figure 14, the spectra of oxide particles vary significantly as a function of location on the cathode surface. The 475/554 band relative intensity and peak half-width were found to vary noticeably with lithium content in the lattice from *in situ* Raman measurements.[61] This has allowed the authors to assign the Raman features of the cycled cathode to fully discharged, partially charged, and fully charged $Li_{1-x}Ni_{0.8}Co_{0.15}Al_{0.05}O_2$ particles. From these results, the authors proposed that electrode degradation is due to a deterioration of electronic contact resistance within the composite cathode. Carbon additive rearrangement, formation of surface films, as well as the poor intrinsic properties of the oxide active material would contribute to this nonuniform local kinetic behavior, which constitutes a common degradation mode for composite Li ion cathodes.[50,61]

Since the interesting observation of high discharge capacity with $Li(Ni_{1/3}Co_{1/3}Mn_{1/3})O_2$ material in 2001 by Ohzuku and
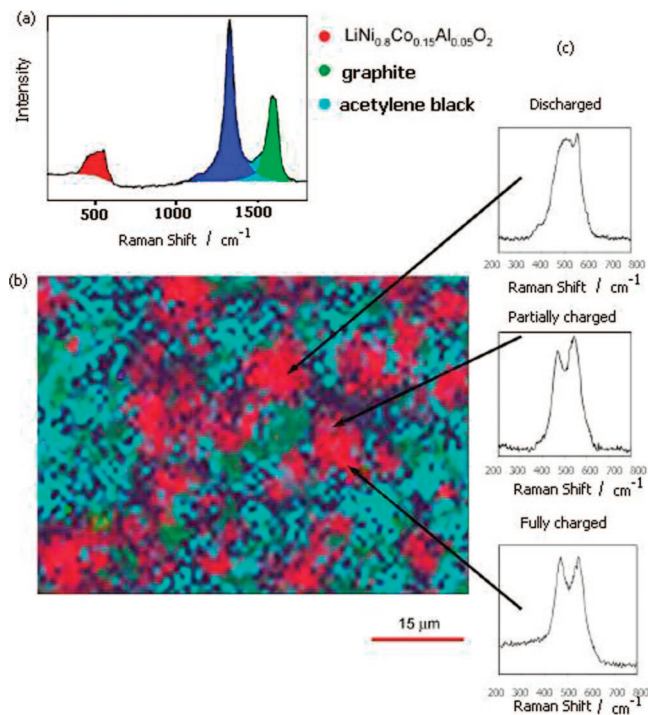
Figure 14. (a) Average Raman spectrum of the fresh composite $LiNi_{0.8}Co_{0.15}Al_{0.05}O_2$ electrode; (b) 52 μm $\times$ 75 μm Raman image of the composite $LiNi_{0.8}Co_{0.15}Al_{0.05}O_2$ cathode from the cycled cell. The image was collected at 0.7 μm resolution. The intensities of red, blue, and green colors correspond to the integrated band intensities of $LiNi_{0.8}Co_{0.15}Al_{0.05}O_2$, and D, G carbon bands of each spectrum, respectively. (c) Raman microscope spectra of three individual $LiNi_{0.8}Co_{0.15}Al_{0.05}O_2$ particles in the tested cathode. Reprinted with permission from ref 50. Copyright 2007 Elsevier.

Makimura1,[143] enormous research on the layered cathode materials based on $Li(Ni_xCo_yMn_{1-x-y})O_2$ with various values of x and y has been reported in the literature.[144−148] A latest *ex situ* structural study by X-ray diffraction and Raman scattering at various stages of charging and discharging of the $Li(Ni_{0.8}Co_{0.1}Mn_{0.1})O_2$ cathode material showed that the host layered structure is maintained throughout the electrochemical lithiation delithiation process in the 3−4.5 V range.[148] XRD data evidenced a reversible and continuous change in the lattice parameters, with a decreasing and c increasing, during the electrochemical extraction, while the Raman spectra exhibit two peaks at ~500 and 560 cm^{-1} characteristic of the rhombohedral layered symmetry, with slight frequency variations.

4.3. Manganese Oxide-Based Compounds

Manganese oxides (MOs) with three- and two-dimensional crystal networks constitute a large family of porous materials that can accept foreign species in their tunnel or interlayer space. There is a wide variety of natural and synthetic MOs, including the various allotropic forms of MnO_2 and ternary lithiated compounds Li_xMnO_y. Having good electrochemical performance, they are attractive as positive electrode materials for lithium cells because manganese has economical and environmental advantages over compounds based on cobalt or nickel.[149,150]

4.3.1. MnO₂-Type Compounds

MnO_2 was originally developed as the positive electrode for primary alkaline batteries.[151] Extensive research was carried out during the last few decades to improve the
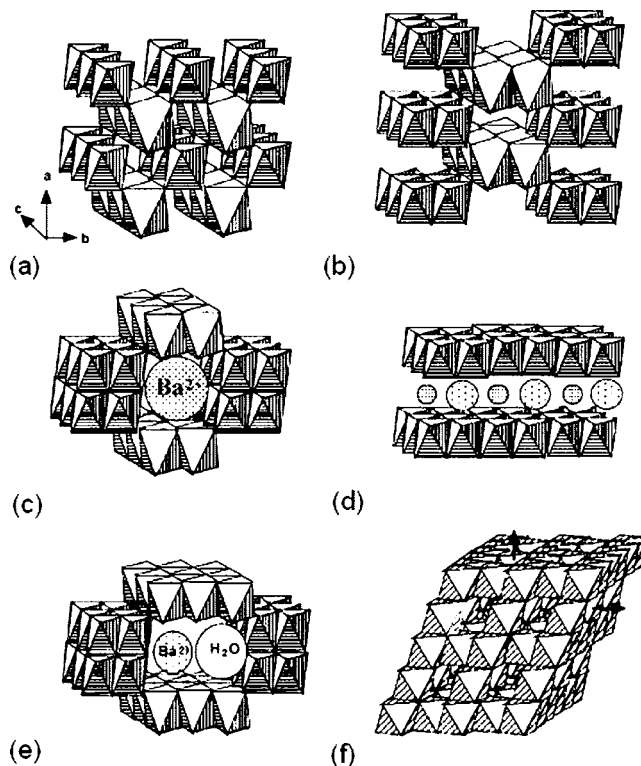
Figure 15. Schematic representation of the various manganese dioxide frameworks showing the variation in the chain and tunnel ($m \times n$) structures. (a) pyrolusite (1×1), (b) ramsdellite (1×2), (c) hollandite (2×2), (d) birnessite ($1 \times \infty$), (e) romanechite (2×3), and (f) spinel (1×1). Reprinted with permission from ref 158. Copyright 2004 Elsevier.

reversibility of lithium insertion in the manganese dioxide cathode for rechargeable Li//MnO_2 cells.[152] Since then, much effort has been devoted to the study of lithium insertion into various forms of manganese dioxides, especially synthetic products prepared by either electrolytic (EMD) or chemical (CMD) methods that belong to the nsutite (γ-MnO_2) group, for use as cathodes in lithium batteries.[153,154] Lithium accommodation in γ-MnO_2 occurs predominantly by insertion into the (2×1) tunnels of the ramsdellite (R-MnO_2) domains, while the β-MnO_2 domains only accommodate 0.2 Li in the (1×1) channels.[73] Besides the γ-MnO_2 form, which suffers from moderate capacity, low reversibility, and poor cycling stability, there are many MO materials under study, such as $LiMn_2O_4$ spinel-like phases,[150,155] layered $LiMnO_2$,[156] and new layered phases, such as hexagonal $\alpha Li_{0.51}Mn_{0.93}O_2$ and orthorhombic $\beta Li_{0.52}MnO_2$.[157]

The common crystallographic unit building the lattice of MOs and that of their lithiated products is the basal MnO_6 octahedron. Table 2[158] summarizes the crystallographic data of various MO compounds. As shown in Figure 15, their structure can be described as a close packed network of oxygen atoms consisting of edge- and corner-sharing MnO_6 octahedra forming tunnels of various sizes for the insertion of Li ions, leading to more or less compact structures in which Mn^{4+} and/or Mn^{3+} ions are distributed.

Figure 16 shows the Raman scattering spectra reported for various manganese dioxide compounds.[158,159] Because the Raman cross section of Mn-oxide is relatively low, the Raman features of MOs are rather weak. Three major regions can nevertheless be distinguished: at 200−450, 450−550, and 550−750 cm^{-1}. They correspond to spectral domains where the skeletal vibrations, the deformation modes of the

Table 2. Crystallographic Data of Some MO Compounds[a]

compd	mineral	crystal symmetry	lattice parameters (Å)	features
MnO	manganosite	cubic ($Fm3m$)	$a = 4.44$	rock-salt
α-MnO$_2$	hollandite	tetragonal ($I4/m$)	$a = 9.96$; $c = 2.85$	(2 × 2) tunnel
R-MnO$_2$	ramsdellite	orthorhombic ($Pbnm$)	$a = 4.53$; $b = 9.27$; $c = 2.87$	(1 × 2) tunnel
β-MnO$_2$	pyrolusite	tetragonal ($P4_2/mnm$)	$a = 4.39$; $c = 2.87$	(1 × 1) tunnel
γ-MnO$_2$	nsutite	complex tunnel (hex)	$a = 9.65$; $c = 4.43$	(1 × 1)/(1 × 2)
δ-MnO$_2$	vemadite	hexagonal	$a = 2.86$; $c = 4.7$	(1 × ∞) layer
λ-MnO$_2$	spinel	cubic ($Fd3m$)	$a = 8.04$	(1 × 1) tunnel
MnO$_x$, H$_2$O	birnessite	tetragonal	$a_{hex} = 2.84$; $c_{hex} = 14.64$	(1 × ∞) layer
MnOOH	groutite	orthorhombic ($Pbnm$)	$a = 4.56$; $b = 10.70$; $c = 2.87$	
α-Mn$_2$O$_3$	bixbyite	cubic ($Ia3$)	$a = 9.41$	C-type
Mn$_3$O$_4$	haussmannite	tetragonal ($I4_1/amd$)	$a = 9.81$; $c = 2.85$	spinel-like

[a] Reprinted with permission from ref.[158] Copyright 2004 Elsevier.
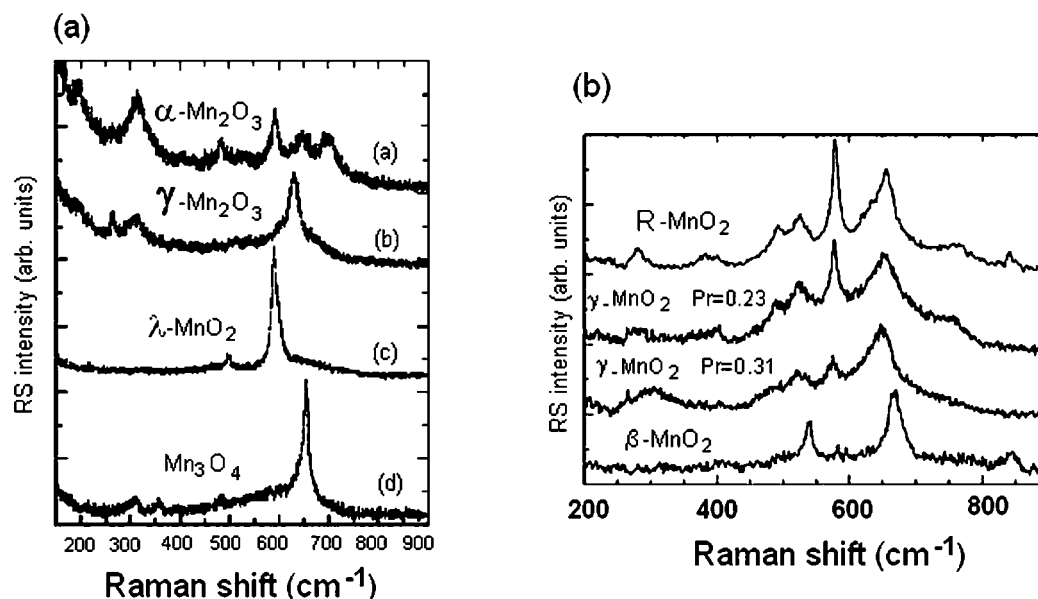
Figure 16. Raman scattering spectra reported for various manganese dioxide frameworks. Pr is the intergrowth rate of the pyrolusite into the ramsdellite matrix. Excitation with 514.5 nm radiation. (a) Reprinted with permission from ref 158. Copyright 2004 Elsevier. (b) Reprinted with permission from ref 159. Copyright 2006 Elsevier.

metal−oxygen chain of Mn−O−Mn in the MnO$_2$ octahedral lattice, and the stretching modes of the Mn−O bonds in MnO$_6$ octahedra occur, respectively.

Few works reported the vibrational spectra of pyrolusite β-MnO$_2$, ramsdellite R-MnO$_2$, and γ-MnO$_2$ compounds. A careful examination of the results published up to now shows discordance regarding Raman spectra reported by different researchers. Strohmeier at al.[160] and Kapteijn et al.[161] found that MnO$_2$ was not Raman-active, whereas Gosztola et al.,[162] Bernard et al.,[163] Buciuman et al.,[164] Widjaja et al.,[165] and Julien et al.[158,159] reported Raman spectra of MnO$_2$ with different spectral features. These disagreements are due to various factors as follows:

(i) the confusing structural characterization of MnO$_2$ compounds (X-ray diffraction patterns are frequently broad, indistinct, or absent);

(ii) the wide variety of synthesis routes, which determine the structural and physicochemical properties (the structural differences are commonly attributed to variations in oxygen stoichiometry, Mn oxidation state, particle size, and the type of defect chemistry);

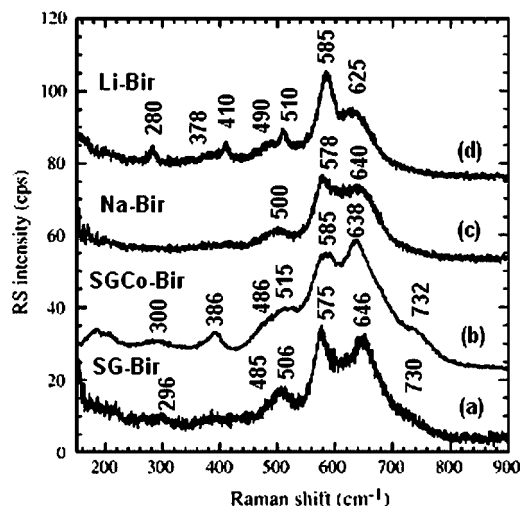(iii) the low Raman activity for most of the manganese oxides;

(iv) the high sensitivity of many manganese compounds (contrary to nickel compounds) under the laser beam. Most MOs are so black that they absorb the photon energy, which results in local heating at the localized region. This point

should be considered with particular attention, since local heating can cause misleading shifts and broadening of the Raman modes due to photoinduced or thermal-induced chemical reactions. Indeed, reduction reactions are easily produced, leading to degradation compounds such as Mn$_2$O$_3$ and Mn$_3$O$_4$.[165−167] It follows that accurate and reliable determination of the pure Raman components of MO compounds is not yet elucidated and that particular caution should be taken toward reported Raman spectra.

The birnessite-type manganese oxides constitute another class of materials with layered structure, with water molecules and/or metal cations occupying the interlayer region (Figure 15d). It has been recently shown that attractive electrochemical performances, with stable capacities of 170 (mA h)/g after 40 cycles at C/20 (Figure 17) could be reached for sol−gel prepared birnessite doped with Co (SGCo-Bir) with chemical formula Co$_{0.15}$Mn$_{0.85}$O$_{1.84}$·0.6H$_2$O.[168] The Raman features of several birnessite compounds were first reported by Julien et al.[169] As shown in Figure 18, in spite of a slight variation in band positions and relative band intensity, the general similarity of the spectra suggests that samples are characterized by the same basic structure. In fact, MnO$_6$ octahedral layers are separated by layers of lower-valent cations (Li$^+$, Na$^+$, Mn^{2+}, etc.) and by layers of water. The highest Raman band is assigned to the symmetric vibration ν(Mn−O) of the MnO$_6$ group, with A$_{1g}$ symmetry in the O_h^7 spectroscopic space group. This mode is observed
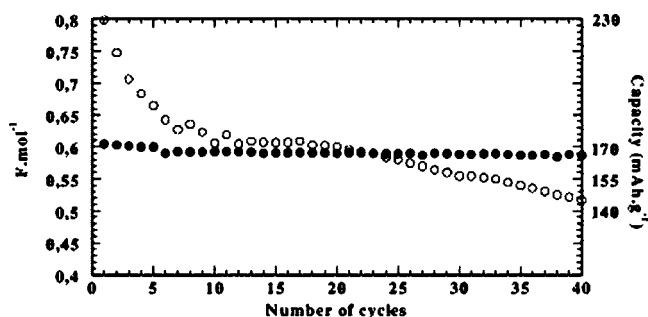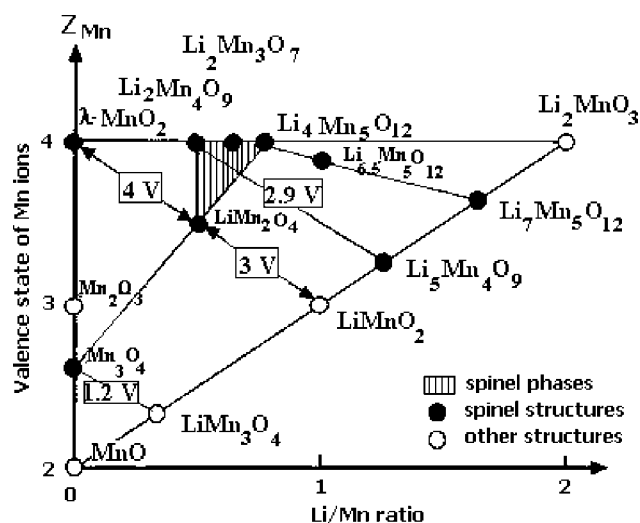
Figure 17. Comparison of the evolution of the specific capacity with the number of cyles at C/20 for the sol−gel birnessite (○) and for the sol−gel Co-Birnessite (●). Reprinted with permission from ref 168. Copyright 2002 Elsevier.

Figure 18. Raman spectra of birnessite-type manganese oxides (a) $MnO_{1.84} \cdot 0.6H_2O$, (b) $Co_{0.15}Mn_{0.85}O_{1.84} \cdot 0.6H_2O$, (c) $Na_{0.32}MnO_2 \cdot 0.6H_2O$, and (d) $Li_{0.32}MnO_2 \cdot 0.6H_2O$. Excitation with 514.5 nm radiation. Reprinted with permission from ref 169. Copyright 2003 Elsevier.

Figure 19. Li−Mn−O phase diagram showing the compositions of spinel, defect spinel, and rock salt structures. Reprinted with permission from ref 171. Copyright 2003 Elsevier.

Co-doped SG-bir. This finding is in good accordance with the better structural stability of the host lattice for the Co-doped material during cycling, as illustrated in Figure 17.

4.3.2. Ternary Lithiated Li_xMnO_y Compounds

Lithiated transition manganese oxides involved as positive electrode materials in high voltage lithium ion batteries exhibit different crystallographic structures. As a consequence, the number of active bands in the vibrational spectra of these compounds varies significantly, depending on their local symmetry (Table 3). Two classes of materials are currently being studied: the spinel-type and the rock-salt-type compounds. The Li−Mn−O phase diagram shown in Figure 19 highlights the positions of spinel and rock salt compositions within the λ-MnO_2, MnO, and Li_2MnO_3 tie-triangle. It emphasizes the wide range of spinel and rock salt compositions that exist in the Li−Mn−O system.

4.3.2.1. Stoichiometric Spinel Phases in the Li−Mn−O System. Stoichiometric spinels fall on the tie line between Mn_3O_4 and $Li_4Mn_5O_{12}$. They are defined by a cation/anion ratio M/O of 3/4. The stoichiometric spinels of importance for lithium battery applications form a solid solution between $LiMn_2O_4$ and $Li_4Mn_5O_{12}$. They are considered currently of technological interest as insertion electrodes for rechargeable 4 V lithium batteries because of their diffusion pathways for Li ions, their low cost, low toxicity, and high energy density (due to the combination of high capacity and high voltage).[150,171−174] The structural, chemical, and electrochemical properties of the $LiMn_2O_4$ system have been extensively reported.[150,171,175] $LiMn_2O_4$ has a normal spinel structure, which is cubic with the space group $Fd3m$ (O^7_h) containing 8 AB_2O_4 units per unit cell. It can be represented by the formula $\{Li\}_{8a}[Mn_2]_{16d}O_4$, in which the subscript 8a indicates occupancy of tetrahedral sites by Li^+ ions, with Mn^{3+} and

at 625 and 640 cm^{-1} for Li-Bir and Na-Bir, respectively, and at 646 and 638 cm^{-1} for SG-Bir and SGCo-Bir, respectively. A correlation between the wavenumber value of this stretching mode and the interlayer *d*-spacing was proposed.[169] The band located at 575 cm^{-1} is attributed to the $\nu(Mn-O)$ stretching vibration with F_{2g} symmetry and is commonly related to the vibrational stretching frequency inherent to the presence of Mn^{4+} ions. Its intensity is particularly strong in birnessite compound compared with the literature data related to lithiated spinels due to the high content of Mn^{4+} in the birnessite family.[168−170] The Raman spectrum of SGCo-Bir, where cobalt partly substitutes for manganese, displays similar features to SG-Bir, $MnO_{1.84}$, $0.6H_2O$. As a result of the substitution of Mn^{4+} by Co^{3+} ions in MnO_2 layers,[168] a frequency shift of 10 cm^{-1}, from 575 to 585 cm^{-1}, was observed[169] for the $\nu(Mn-O)$ stretching vibration with F_{2g} symmetry (Figure 18). This result was correlated with a strengthening of the Mn−O bond in the

Table 3. Structure and Raman Activity for Various Lithiated Transition-Metal Oxide Materials

compd	type of structure	space group	Raman activity
$LiCoO_2$	layered hexagonal rock-salt	$D^{3d}_5 - R\bar{3}m$	$A_{1g} + E_g$
$mLiMnO_2$	layered monoclinic rock-salt	$C^3_{2h} - C2/m$	$2A_g + B_g$
$LiMn_2O_4$	normal cubic spinel	$O^7_h - Fd3m$	$A_{1g} + E_g + 3F_{2g}$
λMnO_2	modified cubic spinel	$O^7_h - Fd3m$	$A_{1g} + E_g + 2T_{2g}$
$Li_2Mn_2O_4$	normal tetragonal spinel	$D^{19}_{4h} - I4_1/amd$	$2A_{1g} + 2B_{1g} + 6E_g + 4B_{2g}$
$Li_{0.5}Mn_2O_4$	ordered cubic spinel	$T^2_d - F43m$	$3A_1 + 3E + 6F_2$

$\{Li\}_{8a}[Mn_2]_{16d}O_4$ **(a)** **(b)**
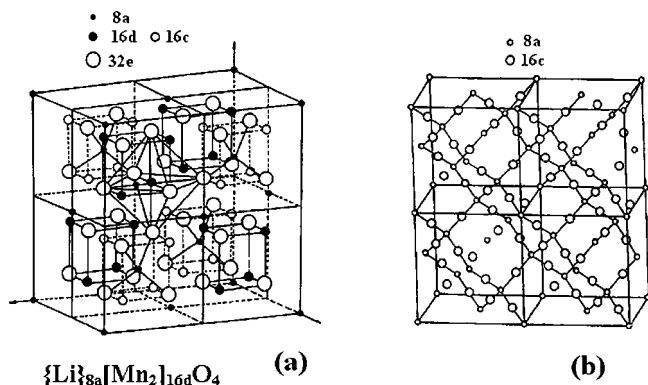
Figure 20. Schematic representation of the structure of AB_2O_4 spinel lattices showing (a) the smallest (primitive) cubic unit cell of a normal spinel ($Fd3m$ space group) and (b) the diffusion path of lithium. Reprinted with permission from ref 73. Copyright 2001 Elsevier.

Mn^{4+} ions (in 1:1 mixture) being randomly distributed over the octahedral 16d sites and oxygen anions in 32e Wyckoff positions (Figure 20a). The approximately cubic close-packed array of oxide ions incorporates MnO_6 octahedra, connected to one another in three dimensions by edge sharing (Figure 15f) LiO_4 tetrahedra, sharing each of their four corners with

a different MnO_6 unit and a three-dimensional network of octahedral 16c holes and tetrahedral 8a sites. When the lithium ion diffuses in the structure, first it moves from the 8a site to the neighboring empty octahedral 16c site and then to the next 8a site in such a way that the Li^+ takes the diffusion path (8a-16c-8a) (Figure 20b).

Vibrational features of spinel oxide structures have been widely studied. Tarte et al. published numerous infrared data on spinels and solid solutions.[176−178] White et al. treated the vibrational spectra of spinel structures by a factor group analysis.[179] The various types of ordering were considered, and the predicted changes were compared with literature data.

Early spectroscopic data on electrochemically prepared spinel-type $Li_xMn_2O_4$ composite electrodes were obtained from FTIR measurements.[180,181] Observation of $LiMn_2O_4$ Raman features at 593 and 628 cm^{-1} was first reported from *in situ* measurements of lithium ion electroinsertion in a spinel-type Pt/λ-MnO_2 electrode.[182] Ammundsen et al.[183] calculated the lattice dynamics of spinel-structured lithium manganese oxides using atomistic modeling methods, which allowed the prediction and the assignment of the Raman spectra of lithiated, fully delithiated, and partially delithiated $Li_xMn_2O_4$ thin films. In good agreement with the calculations,

Table 4. Calculated and Observed Wavenumbers (in cm^{-1}) for Raman-Active Modes of $LiMn_2O_4$, λ-MnO_2, and $Li_{0.5}Mn_2O_4$ Thin Films, Assuming a $F\bar{4}3m$ Space Group for the Latest^a

LiMn₂O₄			λ-MnO₂				Li₀.₅Mn₂O₄			
calcd	obsd		calcd	obsd		symmetry species	calcd	obsd		symmetry species
354	365	382^b				$T_{2g}(1)$	313	296	296^b	T_2
434	432	426^b	479	463	462^b	E_g	317			E
455	480	483^b	511	498	501^b	$T_{2g}(2)$	385		380^b	T_2
597	590	580^b	630	647	644^b	$T_{2g}(3)$	457		425^b	E
598	625	625^b	592	592	596^b	A_{1g}	481	493	483^b	T_2
							537		522^b	T_2
							559	560	563^b	A_1
							586			E
							593	597	596^b	A_1
							615	612	611^b	T_2
							646	630	648^b	T_2
							665	657		A_1

^{a} Most values are reported from ref 183. ^{b} Values reported from ref 171.
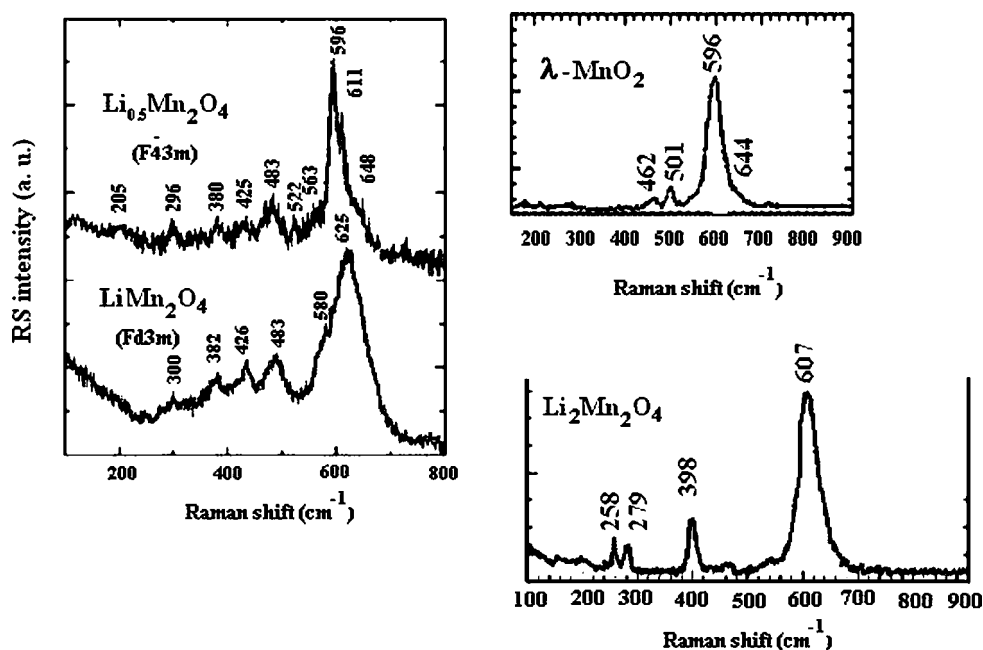
Figure 21. Raman spectra of spinel $LiMn_2O_4$, $Li_{0.5}Mn_2O_4$, λ-MnO_2, and $Li_2Mn_2O_4$. Excitation with 514.5 nm radiation. Reprinted with permission from ref 171. Copyright 2003 Elsevier.

five Raman-active modes are observed for the $LiMn_2O_4$ phase, one of A_{1g} symmetry at 625 cm^{-1}, one of E_g symmetry at 426−432 cm^{-1}, and three of T_{2g} symmetry at 365−380, 480−485, and 580−590 cm^{-1} (Table 4 and Figure 21). The slight underestimation of the calculated A_{1g} mode for $LiMn_2O_4$ (598 instead of 625 cm^{-1}) was ascribed to a small deviation from the model used to describe the electronic polarizability of oxygen ions in $LiMn_2O_4$ (transferred without any change from the λ-MnO_2 model).[183] In a localized vibration analysis, Julien et al.[171] attributed the broadness of the highest frequency A_{1g} mode to the existence of two types of Mn−O vibrating entities: isotropic $Mn^{+IV}O_6$ octahedra and locally distorted $Mn^{+III}O_6$ octahedra. According to the same author, the shoulder peak around 580 cm^{-1} of T_{2g} symmetry would mainly originate from the stretching vibration of the Mn^{+IV}-O bond. Its intensity would depend on the Mn^{+IV} concentration in the spinel and reflect the Mn average oxidation state for this reason. The lowest energy $T_{2g}(1)$ phonon would predominantly derive from a vibration of the Li sublattice and can be viewed as a Li−O stretching motion.

On studying the effect of chromium substitution on the lattice vibration of spinel lithium manganate by performing a combinative micro-Raman and X-ray absorption (XAS) analysis, Hwang et al.[184] provided a new interpretation of the Raman spectrum of $LiMn_2O_4$. On the basis of the dynamic local structural information obtained from XANES/EXAFS experiments, the authors assigned the two intense features at ~580 and ~620 cm^{-1} as totally symmetric A_{1g} modes for regular $Mn^{+IV}O_6$ octahedra and tetragonally distorted $Mn^{+III}O_6$ octahedra, respectively. This new interpretation was further supported by the comparison with the reference spectra of $Li_2Mn_2O_4$ and λ-MnO_2 and the good correlation between the ratio of Mn^{+IV}/Mn^{+III} concentration and the relative intensities of the two Raman peaks.[184] An interesting result provided by this study is that the relative intensity of the two main Raman peaks of the spinel lithium manganate can be used as a measure for estimating the local symmetry and the oxidation state of manganese ion in the spinel lattice.

There have already been many reports on the charge−discharge characteristics of the $Li_xMn_2O_4$ cathode.[173−175] The theoretical specific capacity of $LiMn_2O_4$ is 148 (mA h)/g. The open circuit voltage (OCV) curve of $Li_xMn_2O_4$ (0 < x < 2) is shown in Figure 22.

The structural changes of $Li_xMn_2O_4$ powder electrodes during charge and discharge have been mainly characterized by X-ray diffraction[173,185−187] and neutron powder diffractometry.[185] However, due to the high symmetry of the spinel system, the low X-ray scattering power of lithium, and the occurrence of partial occupation of the various cation sites, the XRD patterns are not always easily interpreted. It is often difficult not only to determine the precise distribution of cations in a given pure phase but also to quantitatively analyze multiphase mixtures or to distinguish between different phases with similar lattice constants. This problem is especially acute for $Li_xMn_2O_4$ with $0.2 \leq x \leq 1$, as the cubic cell parameter changes by only 3% over the entire composition range. Diffraction data obtained from electrodes is commonly of poor quality due to degradation of crystallinity during cycling, the presence of other phases (carbon, electrolyte), and compositional inhomogeneity.

While vibrational spectroscopy cannot give the detailed structural information available from high quality diffraction
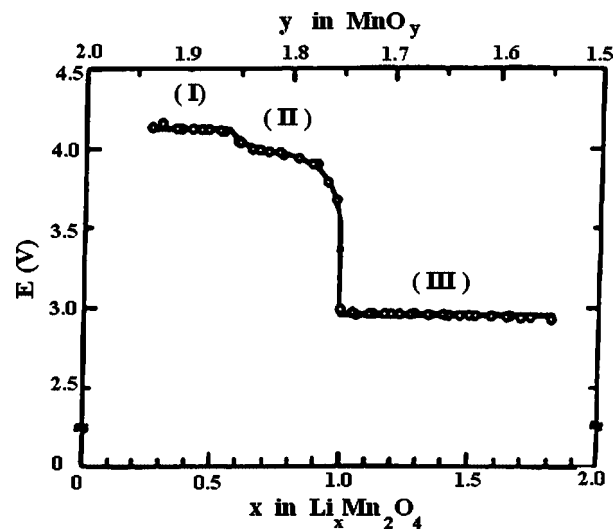
Figure 22. Open circuit voltage (OCV) curve of $Li_xMn_2O_4$ (0 < x < 2) at 30 °C. Reprinted with permission from ref 173. Copyright 1990 The Electrochemical Society.

data, it is sensitive to the local environments of lithium and transition metal cations in the oxide lattice. The number, frequency, and relative intensities of the vibrational bands depend upon both coordination geometries and bond strengths (which may, in turn, depend on occupancy factors and oxidation states). Poorly crystalline or amorphous components that make only broad background contributions to XRD patterns are, however, represented quantitatively in FTIR and Raman spectra.

Lithium may be electrochemically extracted from $LiMn_2O_4$, at a potential of about 4 V vs metallic lithium, corresponding to the (I) + (II) region in Figure 22, according to the oxidation reaction:

$$LiMn_2O_4 \rightarrow Li_xMn_2O_4 + (1-x)e^- +$$
$$(1-x)Li^+ \qquad 0.2 \leq x \leq 1$$
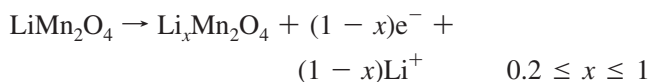
In this composition range, $Li_xMn_2O_4$ retains the cubic symmetry and appears to be composed of a single phase for $0.5 < x < 1$. As lithium is removed from the tetrahedral 8a site, there is a monotonic decrease in the cubic cell parameter. The OCV curve is nearly flat, showing two distinct plateaus above and below $x = 0.5$. The flat part of the discharge curve in the range $x < 0.5$ is considered to be a two-phase region in which a new cubic phase is produced and exists up to full electrochemical delithiation near a composition $x \approx 0.015$. The $Li_{0.015}Mn_2O_4$ phase (termed λ-MnO_2) has a slightly modified cubic symmetry, with the removal of lithium ions resulting in the loss of the $T_{2g}(1)$ phonon at low wavenumber 365−382 cm^{-1} (see Tables 3 and 4). Phonon lattice calculations predict that the T_{2g} and E_g modes should increase in wavenumber whereas the A_{1g} mode should decrease in wavenumber[183] (Table 4). However, this prediction is not supported by any structural consideration. The experimental Raman spectrum of λ-MnO_2, reported in Figure 21, is in good accordance with these calculations, in terms of both number of bands and frequencies.

For intermediate compositions between $LiMn_2O_4$ and λ-MnO_2, the local symmetry no longer belongs to the $Fd3m$ space group. A lower symmetry has been proposed with the $F\bar{4}3m$ (T_d^2) space group (Table 3). It turns out that a richer Raman fingerprint is expected for the partially delithiated

compounds, with 12 expected Raman-active modes instead of 5 for $LiMn_2O_4$. This analysis is supported by reported experimental Raman data for the $Li_{0.5}Mn_2O_4$ phase, summarized in Table 4 and Figure 21. In this structure, every second lithium tetrahedral site is vacant, producing an ordered Li configuration, which has been experimentally observed for the $Li_{0.5}Mn_2O_4$ composition.[188] This subtle ordering transition could be responsible for the flat potential curve observed for $0.5 < x < 1$ (Figure 22).

Continuous charge−discharge cycling of $Li_xMn_2O_4$ electrodes in the high voltage region (I + II) results in significant capacity fading, particularly when they are charged at potentials greater than 4 V. A FTIR spectroscopy study has demonstrated that overcharging causes a gradual conversion to a lithium-poor defect spinel material *via* dissolution of manganese ions in the electrolyte.[181]

Electrochemical insertion of lithium into $LiMn_2O_4$ proceeds in a very different manner for $1 \leq x \leq 2$, in the flat region (III), according to a reduction reaction involving a phase transition from cubic spinel to an ordered tetragonal, $Li_2Mn_2O_4$ phase:

$$LiMn_2O_4 + e^- + Li^+ \rightarrow Li_2Mn_2O_4$$
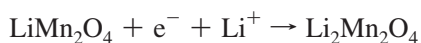
For $1 < x < 2$, $Li_xMn_2O_4$ is a mixture of two distinct phases: the original cubic phase and a tetragonal spinel-type compound. This phase transition is provoked by the Jahn−Teller distortion due to the increase in Mn^{3+} ($3d^4$) concentration during intercalation of lithium in $LiMn_2O_4$. As a consequence, the crystal symmetry is lowered from cubic to tetragonal, which results in a volume expansion of about 6.4%. Mechanical degradation due to the large volume change during the cubic-to-tetragonal phase transition is the primary cause of capacity fading in the 3 V region ($1 < x < 2$).

The structure of $Li_2Mn_2O_4$ is a distorted spinel, which belongs to the $I4_1/amd$ space group (see Table 3). According to a neutron diffraction study, the added Li ions go into the previously vacant 16c octahedral sites, and about half of the lithium ions in the tetrahedral 8a sites move also in the 16c position.[189] The cubic-to-tetragonal transition is detected only by the splitting of some peaks in the X-ray diffraction patterns whereas lithium incorporation into $LiMn_2O_4$ leads to an important change in the vibrational features. As shown in Figure 21, the Raman spectrum of tetragonal $Li_2Mn_2O_4$ is dominated by four typical lines located at 607, 398, 279, and 258 cm^{-1}. It should be noticed that a greater number of bands was expected from the spectroscopic analysis, which predicts 14 Raman-active modes for the tetragonal $Li_2Mn_2O_4$ phase with D_{4h}^{19} symmetry: $2A_{1g} + 2B_{1g} + 6E_g + 4 B_{2g}$ (Table 3). A straightforward description of the experimental Raman spectrum of tetragonal $Li_2Mn_2O_4$ is not yet provided, even if some tentative assignments have been speculated from a localized vibration analysis.[190]

Raman microspectrometry constitutes a very efficient probe for the identification of electrochemically produced spinel-like lithiated manganese oxide materials. *In situ* Raman measurements during the charge−discharge of a $LiMn_2O_4$ composite cathode have been performed.[36] However, only poor structural information can be drawn due to the limited frequency range, low quality Raman spectra and local inhomogeneity. *In situ* Raman investigation of pure $Li_{1-x}Mn_2O_4$ ($0 \leq x \leq 1$) thin films produced by electrostatic spray deposition did not allow a straightforward analysis,
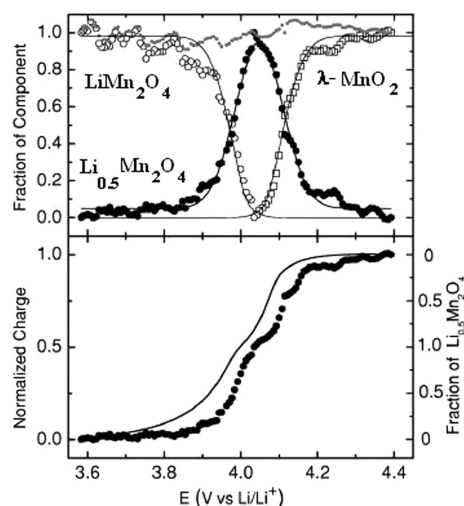
**Figure 23.** (top) Fraction of each of the components of $Li_xMn_2O_4$ as a function of the potential extracted from Raman data using classical least-squares (CLS) curve resolution. (bottom) Normalized charge determined by coulometric analysis of the voltammetric curve (left ordinate, solid curve) and fraction of $Li_{0.5}Mn_2O_4$ as a function of the potential (scattered symbols). Reprinted with permission from ref 192. Copyright 2005 The Electrochemical Society.
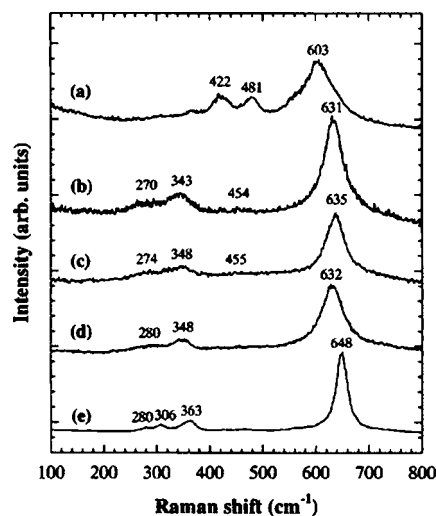
since the Raman spectra are hampered by the lines of the sapphire optical window and the electrolyte.[191] On the other hand, *in situ* spectroelectrochemical Raman measurements performed by Scherson et al. on a $LiMn_2O_4$ single crystal microelectrode during simultaneous cyclic voltammetry experiments have afforded the spectroscopic fingerprints of λ-MnO_2, $Li_{0.5}Mn_2O_4$, and $LiMn_2O_4$, respectively.[59,192] From the analysis of the Raman spectra using classical least-squares (CLS) curve resolution, the authors provide the fraction of the different $Li_xMn_2O_4$ components as a function of the potential (Figure 23). The obtained results allow direct correlations to be made between the state of charge of single particle electrodes and their Raman spectroscopic properties, thereby providing means of monitoring spatiotemporal effects induced by Li intercalation−deintercalation.

One of the main routes considered to reduce the capacity fading of $LiMn_2O_4$ is partial substitution of manganese by transition metals M.[73,193,194] As a matter of fact, $LiM_xMn_{2-x}O_4$ (M = Cr, Co, Ni, Al, Li, ...) materials are regarded as attractive cathodes for lithium batteries, allowing the cell voltage to be increased to 5 V with an improved cycle life. The stabilization of the octahedral 16d site is achieved by reducing the amount of Mn^{3+} causing the Jahn−Teller distortion. The enthalpy of the cubic-to-tetragonal phase transition in partially substituted $LiM_xMn_{2-x}O_4$ spinels gradually decreases with increasing amount of substituent and is completely suppressed with 10−20 mol % of substitution in the octahedral Mn site.[193] The variation of the specific capacity with cycle number for various $LiM_{1/6}Mn_{11/6}O_4$ spinels (M = Cr, Co, Ni, Al) is reported in Figure 24. It can be seen that the cells with substituted $LiMn_2O_4$ show better cycling characteristics than the one with undoped $LiMn_2O_4$.
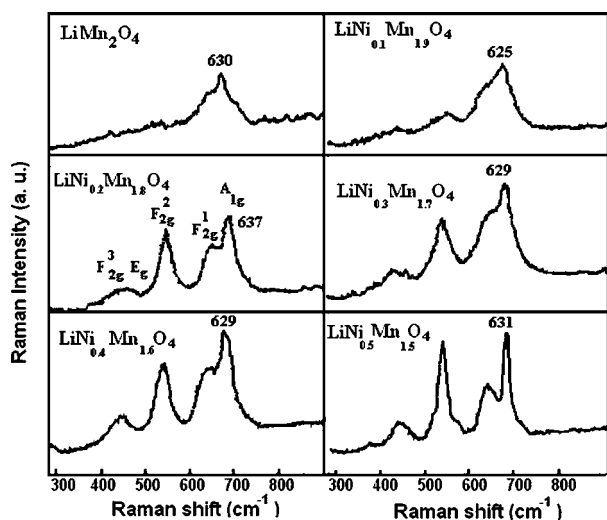
Several studies have shown that the improvement in the cycleability of the substituted $LiM_xMn_{2-x}O_4$ was related to the enhanced stability of the local structure of the materials in comparison to that of $LiMn_2O_4$.[195] Furthermore, when the cations involved have indistinguishable scattering power, vibrational spectroscopy has proved to be very powerful in
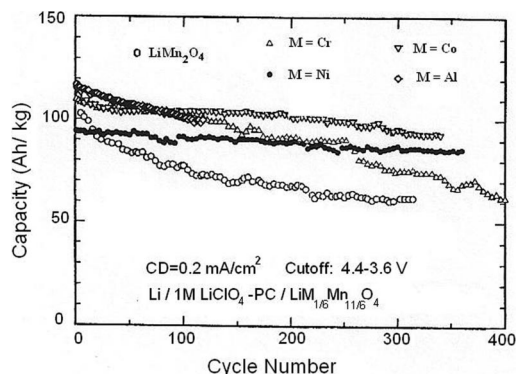
Figure 24. Specific capacity as a function of the cycle number for $LiM_{1/6}Mn_{11/6}O_4$ (M = Cr, Co, Ni, Al). Reprinted with permission from ref 73. Copyright 2001 Elsevier.

Figure 25. Raman spectra of the $LiNi_xMn_{2-x}O_4$ compounds. Laser excitation line: 514.5 nm. Reprinted with permission from ref 197. Copyright 2006 Elsevier.

Figure 26. Micro-Raman spectra for (a) monoclinic layered $LiMnO_2$, (b) cubic spinel $LiMn_2O_4$, (c) delithiated $LiMnO_2$, (d) relithiated $LiMnO_2$, and (e) electrochemically cycled $LiMnO_2$. Excitation with 514.5 nm radiation. Reprinted with permission from ref 203. Copyright 2001 The Electrochemical Society.

determining symmetry changes undetectable by XRD. In spite of this, only limited Raman studies have been devoted to this topic, presumably because of the difficulties in interpreting the Raman spectra of such materials.

On investigating the question of cation ordering in Li−Mn−O spinels with 1/4 substitution on the octahedral sites, Strobel et al. reported several IR and Raman changes which have been related to the presence of well-separated, ordered cationic sites and symmetry lowering, depending on the nature of the substituent.[196] A Raman study of the evolution of the local structure of spinel $LiNi_xMn_{2-x}O_4$ with the Ni substitution ($0 < x \leq 0.5$) was performed.[197] Particular attention has been paid to the position of the A_{1g} Raman band, which reflects the [MO_6] octahedron compactness (M = Ni, Mn). Its value depends on the nature and the rate of the substituent (Figure 25). The variation of the A_{1g} Raman wavenumber with the nickel content indicates that there exists a critical composition level in $LiNi_xMn_{2-x}O_4$ with respect to the local structural stability of the materials. Hence, the most compact [MO_6] octahedron with the highest bond energy of Mn(Ni)−O was formed at the Ni substitution of x = 0.2.

Raman investigations were conducted for $LiNi_xMn_{2-x}O_4$ ($0 < x < 0.5$)[198] and $LiCo_xMn_{2-x}O_4$ ($0 < x < 1$)[199] thin films as well as for lithium-rich $Li_{1+\delta}Mn_{2-\delta}O_4$ powders.[200] In particular, Uchida et al. clearly showed that *in situ* Raman spectroscopy is very helpful in clarifying the valence states

of the metals in $LiNi_xMn_{2-x}O_4$[198] and $LiCo_xMn_{2-x}O_4$[199] thin film electrodes during the electrochemical lithiation/delithiation processes.

4.3.2.2. Layered Rock Salt Phases in the Li−Mn−O System. Stoichiometric rock salt compounds are located on the tie line between MnO and Li_2MnO_3 (Figure 19). These layered lithiated manganese oxides are also under investigation for battery applications.[156,201] Among them, α-$LiMnO_2$ exhibits the largest initial capacity for the 4 V region, but it suffers from severe capacity fading after the first charge process.[156] In fact, most layered compounds have structural features in common with spinels and convert readily upon cycling.

The structure of α-$LiMnO_2$ is monoclinic ($C2/m$ space group, C^3_{2h} spectroscopic symmetry, $Z = 2$) because the coordination polyhedron around the Mn^{3+} ions is distorted due to the Jahn−Teller effect. This compound exhibits cation ordering of the α-$NaFeO_2$ structure, in which Li^+ ions are located between the MnO_6 sheets, in the same octahedral 2d interstices as Mn^{3+} ions, whereas oxygen anions are in 4i sites. According to the group theory, the monoclinic $LiMnO_2$ oxide is predicted to show three Raman-active modes with $2A_g + B_g$ species. As shown in Figure 26a, three main peaks are detected in the Raman spectrum of the monoclinic $LiMnO_2$ phase, at 422, 481, and 603 cm^{-1}, with this latest peak being attributed to the A_g mode involving the symmetric stretching vibration of equatorial oxygen atoms, while the shoulder at 575 cm^{-1} is attributed to the stretching mode of Mn ions bonded to axial oxygen atoms.[190] Indeed, in the case of layered $LiMnO_2$, a manganese ion possesses six neighbor oxygen ions with two different Mn−O distances, that is two Mn−$O_{equatorial}$ = 1.91 Å and four Mn−O_{axial} = 2.32 Å.[202]

Therefore, Raman spectroscopy is very effective in identifying closely related structures such as rock-salt (Figure 26a) and spinel lithium manganate (Figure 26b) phases. On studying the local structural changes of lithium manganese oxide upon electrochemical cycling, an irreversible Mn migration process into the interlayer lithium site was found from the first charge process, which results in the creation of a spinel-like cation ordering[203] (Figure 26c−e).
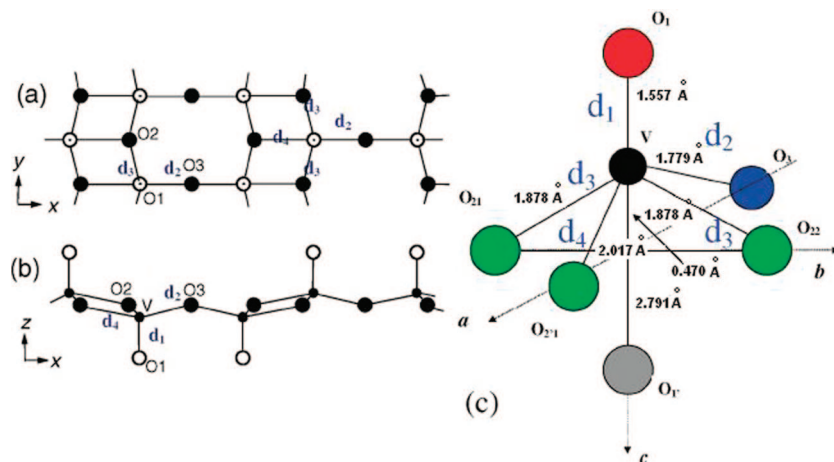
Figure 27. Crystal structure in V_2O_5 in *xy* (a), in *xz*-projection (b), and in local vanadium environments (c). The V atoms are shown by the small black circles, and the O2 and O3 atoms are shown by the large black circles. The O1 atoms are shown by the large open circles.

Work is underway by several groups to improve the metastability by admetal doping or by pillaring the layers. In fact, less rigid manganese oxide structures, and those not based on a cubic close packed array of oxygen atoms, are much more likely to remain phase-stable upon cycling in a lithium cell configuration. As an example, Li_xMnO_2 compounds derived from $Na_{0.44}MnO_2$ exhibit remarkable stability in polymer or in carbonate-based electrolytes, attributed to the double tunnel structure, which cannot easily undergo rearrangement to spinel.[204,205] However, Li_xMnO_2 exhibits poor cycling behavior in room temperature ionic liquids, which potentially offer a wider stability window.[206] A vibrational study was recently performed, using Raman microscopy and FTIR spectroscopy, which showed evidence for the formation of a thick surface film on the Li_xMnO_2 cathode arising from surface decomposition, phase transformation of part of the material, and direct oxidation of the electrolyte at the cathode.[207] This complex surface layer, whose thickness is found to increase during cycling, would create electronic barriers within the composite cathode and affect both rate capability and charge capacity.

In conclusion, the wide variety of Mn−O and Li−Mn−O crystalline phases makes the Raman probe particularly relevant to identify the local signature of each family of compounds. Raman research in this field leads to two different sets of data. Considering the MO system, it is clear that, apart from general considerations, there is up to now no clear and relevant trend in the literature data for a straightforward assignment of the complex and various vibrational features of MnO_2-based compounds. In particular, there is a lack of experimental approach devoted to the study of either chemically lithiated samples or cathode materials under operation. In contrast, for the more attractive spinel system $LiMn_2O_4$ working at 4 V as well as for the layered $LiMnO_2$ material, detailed spectroscopic data are available with a relevant interpretation of the Raman spectra for the charged and discharged electrodes. Raman spectroscopy constitutes a particularly powerful technique in this field, since it affords in many cases a clear identification of the phases whereas X-ray diffraction data analysis is hampered by their high structural similarity. It remains however that this complex system is far from being completely investigated. Other spinel compositions such as $Li_2Mn_3O_7$, $Li_2Mn_4O_9$, $Li_4Mn_5O_{12}$, etc. require additional efforts, both

to obtain reference Raman spectra and to provide consistent assignments.

4.4. Vanadium Pentoxide V_2O_5

Vanadium pentoxide is an attractive material for applications in electrochromic thin film devices and as cathode in lithium batteries, due to its capacity to accommodate up to three lithium ions per mole of oxide, providing a high specific capacity around 450 (mA h)/g in the voltage range 4/1.5 V.[208−213] The electrochemical performances are strongly related to the nature and the amplitude of the structural changes induced by the lithium insertion−deinsertion process, which has prompted a great number of studies focusing on the structural features of V_2O_5 and its lithiated $Li_xV_2O_5$ phases.

4.4.1. V_2O_5 Structure

V_2O_5 crystallizes in the *Pmmn* space group, with lattice parameters *a* and *c* of the orthorhombic cell equal to 11.50 and 4.40 Å, respectively. The point symmetry group of V_2O_5 is D_{2h}. The structure of the vanadium−oxygen layers in V_2O_5 is presented in Figure 27. It can be seen (Figure 27c) that the vanadium atom is located within the oxygen coordination polyhedron VO_5 and is shifted away from the plane formed by four oxygen atoms at a normal distance of 0.47 Å. Four types of V−O bonds, characterized by their particular bond length, can be distinguished:

 - the short and strong apical V=O_1 bonds, $d_1 = 1.577$ Å,
 - the bridge V−O_3 bonds, $d_2 = 1.779$ Å,
 - the "ladder step" V−O_2 bonds (giving two equivalent intra ladder V−O_{21} and V−O_{22} bonds), $d_3 = 1.878$ Å,
 - the interchain V−O_2 bonds (labeled as V−$O_{2'1}$ in Figure 27c), $d_4 = 2.017$ Å.

Polarized Raman[214] and IR reflection[215] spectra of the V_2O_5 crystal have been thoroughly studied and interpreted on the basis of phonon state calculations. More recently, a qualitative characterization of the normal vibrations of the V_2O_5 lattice has also been performed in terms of atomic displacement.[216] With all valence V−O bonds being oriented along coordinate axes (Figure 27), any bond-stretching mode involves oscillations of particular oxygen atoms along particular Cartesians axes. Moreover, due to the difference in bond lengths, the spectral lines characteristic for the bond-
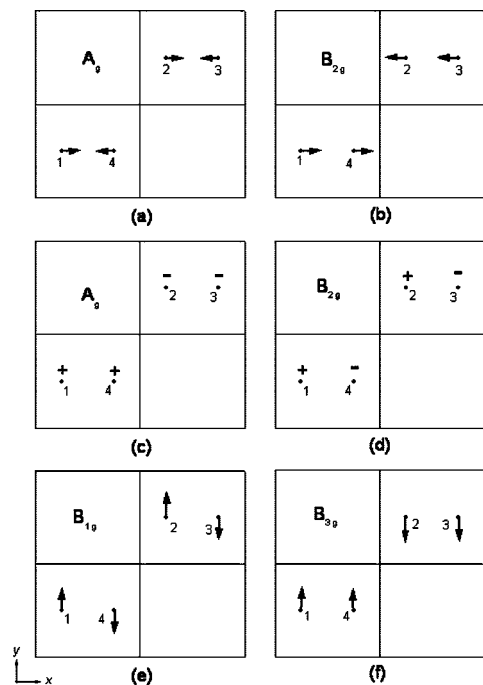
Figure 28. Symmetric atomic displacement combinations for the *Pmmn* space group. The numbers 1, 2, 3, and 4 refer to the four symmetry equivalent atomic positions for a given atom in the unit cell. Reprinted with permission from ref 216. Copyright 2008 American Chemical Society.
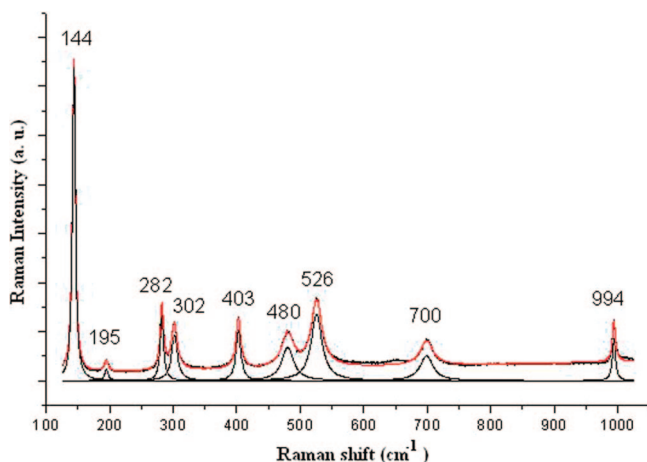
Figure 29. Raman spectrum of V_2O_5 (in red) and the deconvolution shown below (in black). Excitation with 532 nm radiation. Reprinted with permission from ref 216. Copyright 2008 American Chemical Society.

stretching oscillations of the different V–O bonds can be easily assigned. There are four symmetry-equivalent atomic positions per unit cell for the V, O_1, and O_2 atoms and only two for the O_3 atoms, because they lay in the mirror plane perpendicular to the x axis. All these positions correspond to atoms of the same layer, and all layers, which alternate with each other in the z-direction, are equivalent. By using the standard table of characters of irreducible representations of the D_{2h} group, 12 symmetric combinations can be built from Cartesian displacements of four equivalent atoms, six of which are IR-active and six others of which are Raman-active. The Raman-active combinations are shown in Figure 28, with numbers 1, 2, 3, and 4 referring to the four symmetry equivalent atomic positions for a given atom in the unit cell. It is seen that the x- and z-displacements give rise to the A_g and B_{2g} modes while the y-displacements give

Table 5. Symmetry and Frequency Distribution of Normal Vibrations of the V_2O_5 Lattice with Their Assignment to Particular Atomic Displacements[a]

atomic displacement	assignment	Ag	B2g
Z(O1)	$\nu(d_1)$	994	976[b]
X(O3)	$\nu(d_2)$		848[b]
X(O2′)	$\nu(d_4)$	526	502[b]
Z(O3)	δ(V–O3–V)	480	
X(O1)	ρ(V=O1)	403	350[b]
Z(O2)		302	310[b]
X(V)	δ(O2–V–O2)	195	195
Z(V)	δ(O3–V–O2)	104	143[b]

atomic displacement	assignment	B1g	B3g
Y(O2)	$\nu(d_3)$	700	700
Y(O1)	ρ(V=O1)	282	282
Y(O3)	δ(O2–V–O2)		220[b]
Y(V)	δ(O3–V–O2)	144	144

[a] Reprinted with permission from ref 216. Copyright 2008 American Chemical Society. [b] Not observed experimentally.

rise to the B_{1g} and B_{3g} modes. Taking also into account the infrared B_{1u} and B_{3u} IR-active modes related to x, z-displacements respectively and the A_u and B_{2u} species related to y-displacements, the vibrational species for V, O_1, and O_2 atomic motions can be represented as

$$\Gamma(V) = \Gamma(O_1) = \Gamma(O_2) = 2A_g + 2B_{2g} + B_{1g} + B_{3g} + 2B_{1u} + 2B_{3u} + A_u + B_{2u}$$

Due to the special position of the O_3 atoms, the $x(O_3)$ displacements do not contribute to A_g and B_{1u} modes, the $z(O_3)$ displacements do not contribute to B_{2g} and B_{3u} modes, and the $y(O_3)$ displacements do not contribute to B_{1g} and A_u modes. Hence, the vibrational species for the motion of this atom can be expressed as

$$\Gamma(O_3) = A_g + B_{2g} + B_{3g} + B_{1u} + B_{3u} + B_{2u}$$

In total, the optically vibrational modes of V_2O_5 are obtained from the overall contributions of each atom after subtracting the acoustic modes ($\Gamma_{acoustic} = B_{1u} + B_{2u} + B_{3u}$)

$$\Gamma(V_2O_5) = \sum \Gamma(i) - \Gamma_{acoustic}$$

$$\Gamma(V_2O_5) = [7A_g + 7B_{2g} + 3B_{1g} + 4B_{3g} + 7B_{1u} + 7B_{3u} + 3A_u + 4B_{2u}] - [B_{1u} + B_{2u} + B_{3u}]$$

$$\Gamma(V_2O_5) = 7A_g + 7B_{2g} + 3B_{1g} + 4B_{3g} + 6B_{1u} + 6B_{3u} + 3A_u + 3B_{2u}$$

It follows then that 21 modes are expected in the Raman spectrum of V_2O_5.

The Raman spectrum of V_2O_5 is shown in Figure 29. The frequency distribution of the normal vibrations of V_2O_5, with their assignments to particular atomic displacements, is presented in Table 5. The modes originating from the same atomic displacement are gathered in the rows of Table 5. The modes of different symmetry are arranged in different columns in this table.

The bond-stretching modes cover the interval of 500–1000 cm^{-1}. First, z-displacements of O_1 atoms give rise to the highest frequency $\nu(d_1)$ mode at 994 cm^{-1}. It corresponds to the in-phase stretching vibration of all apical V–O_1 bonds. The Raman-active $\nu(d_1)$ mode of B_{2g} symmetry expected

around 976 cm^{-1} was not detected in our spectra. According to the general theory of Raman intensities, the main contributions to the Raman tensor for the bond-stretching modes are determined by derivatives of bond polarizability with respect to the bond lengths. Owing to the symmetry of the B_{2g} representation, half of the V–O$_1$ bonds stretch, whereas the other half compress. This could explain that this mode is hardly observed in spite of the fact that it is Raman allowed from symmetry considerations. A very weak Raman line located at 976 cm^{-1} was assigned the B_{2g} mode by Abello et al.[214]

Next in the frequency scale is the $\nu(d_2)$ mode, which comes from $x(O_3)$ displacements and which corresponds to an antiphase stretching of the V–O$_3$ bonds forming the V–O$_3$–V bridges. This mode of B_{2g} symmetry, calculated at 848 cm^{-1}, was also not detected experimentally.[214] Its low Raman intensity is caused by the fact that the V–O$_3$–V bridge is pseudocentrosymmetric (V–O$_3$–V angle is 148°).

Then follows the $\nu(d_3)$ mode (at 700 cm^{-1}) involving the $y(O_2)$ displacements. It corresponds to an antiphase stretching of the V–O$_2$ bonds. The V–O$_2$ bonds (1.88 Å) are longer than the V–O$_3$ bonds (1.78 Å). Correspondingly, the frequencies of the O$_2$-modes are lower than that of the O$_3$-mode.

The Raman-active mode at around 526 cm^{-1} originates from the $\nu(d_4)$ stretching vibration involving x-displacements of O$_{2'}$ atoms. The A_g mode gives rise to the Raman line observed at 526 cm^{-1}. The B_{2g} line at 502 cm^{-1} was not detected because of its low intensity.

The angle-bending modes cover the 200–500 cm^{-1} range. It is more difficult to determine the frequency distribution for these modes because of considerable coupling. The Raman peak at 480 cm^{-1} can be assigned to bending vibrations of the V–O$_3$–V bridge angle (Figure 27). Raman bands in the frequency region between 400 and 200 cm^{-1} correspond to the modes which involve the x- and y-displacements of O$_1$ atoms at 403 and 282 cm^{-1}, respectively, and the z-displacements of O$_{21}$ and O$_{22}$ atoms at 302 cm^{-1}. These atomic displacements produce the $\delta(O_1–V–O_2)$ and the $\delta(O_1–V–O_3)$ bending deformations. Corresponding modes can be characterized as the $\rho(V=O_1)$ bond rocking oscillations. The $\rho(V=O_1)$ deformation in the xz-plane, which involves the O$_1$ atom oscillations along x-axis, gives rise to the A_g Raman peak at 403 cm^{-1}. The Raman features at around 300 cm^{-1} correspond to y-oscillations of O$_1$ atoms accompanied with z-oscillations of O$_2$ atoms. Two peaks in the low-frequency region are associated with the modes involving displacements of the V atoms. The line at 195 cm^{-1} comes from the A_g and B_{2g} modes with the atoms oscillating along the x-axis, $\delta(O_2–V–O_2)$. The most intense Raman line at 144 cm^{-1}, $\delta(O_3–V–O_2)$, corresponds to a mixture of signals coming from B_{1g} and B_{3g}. The B_{1g} mode involves the shear motion of the ladders, whereas the B_{2g} consists of rotations of the ladders along their axes. The high intensity of this line reflects the long-range order in the plane of the vanadium oxygen layers.

4.4.2. Li$_x$V$_2$O$_5$ Bulk Phases

In spite of numerous studies, the Li/V$_2$O$_5$ system is far from being completely elucidated, and this is mainly due to the complex nature of the lithiated phases involved during the lithium insertion–deinsertion process according to the electrochemical reaction:

$$V_2O_5 + xe^- + xLi^+ \rightleftharpoons Li_xV_2O_5 \qquad 0 < x \leq 3$$
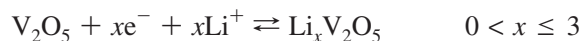
The typical discharge–charge curve of a composite V$_2$O$_5$ cathode exhibits several voltage plateaus corresponding to well-known phase transitions reported for the bulk Li$_x$V$_2$O$_5$ system (Figure 30). Depending on the amount of lithium (x) intercalated in V$_2$O$_5$, several structural modifications have been reported.[208,211,213,217−223] The α-, ε-, and δ-Li$_x$V$_2$O$_5$ were identified in the $0 < x \leq 1$ composition range. Above 3 V, the α-Li$_x$V$_2$O$_5$ phase occurs with $x < 0.1$ whereas the pure ε-phase exists in the range $0.3 < x < 0.7$. Then the pure δ-phase appears with x between 0.9 and 1. The lithium contents corresponding to the limiting composition of the three solid solutions differ slightly from one report to another. The crystallographic data of the Li$_x$V$_2$O$_5$ phases are reported in Table 6.[224]

The structure of the vanadium–oxygen layers is rather similar in pure V$_2$O$_5$ and in the α, ε, and δ phases of Li$_x$V$_2$O$_5$ (Figure 31), with however an increased puckering of the layers revealed by the decrease in the a parameter in the ε and δ phases. Moreover, the increase of the number of inserted lithium ions between the layers is responsible for the increase in the c parameter. All these phase transitions are fully reversible in the $0 < x \leq 1$ composition range, and the structure of the pristine V$_2$O$_5$ phase is recovered upon deintercalation. The situation becomes more problematic for lithium contents $x > 1$, with the δ-phase being transformed into a γ-one on the third voltage plateau at 2.2 V via an irreversible reconstruction mechanism.[211,213] The space group of the γ-LiV$_2$O$_5$ structure is *Pnma*. As in the α- and δ-phases, this structure still contains the V$_2$O$_5$ layers perpendicular to the z-axis. However, the structure of the γ-phase differs from the structure of the δ-phase markedly (Figure 31). The Li atoms are shifted in the x-direction from their symmetric positions in the δ-phase. This is accompanied by important deformations of the V$_2$O$_5$ layers leading to irreversible symmetry loss and bond breaking. It follows that the γ-phase structure remains stable even after deintercalation of all Li atoms,[213] leading to a new metastable γ' variety of V$_2$O$_5$.[221]
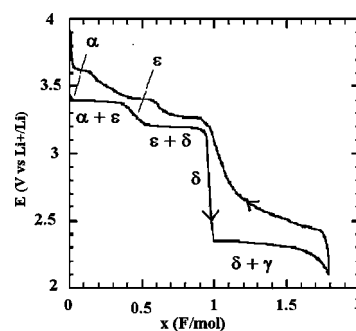

Figure 30. First discharge–charge curve of a composite Li$_x$V$_2$O$_5$ electrode showing the different phases electrochemically produced in the $0 < x < 2$ composition range. C/10 rate.

Table 6. Lattice Parameters for α-V$_2$O$_5$, ε-Li$_{0.52}$V$_2$O$_5$, δ-LiV$_2$O$_5$, and γ-LiV$_2$O$_5$ Phases[a]

|	α-V$_2$O$_5$ (*Pmmn*)	ε-phase (*Pmmn*)	δ-phase (*Amma*)	γ-phase (*Pnma*)
a (Å)	11.51	11.38	11.24	9.69
b (Å)	3.56	3.57	3.60	3.60
c (Å)	4.37	4.52	9.91	10.67

[a] Reprinted with permission from ref 224. Copyright 2006 American Chemical Society.
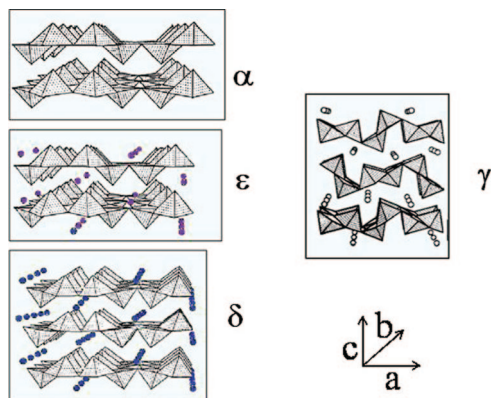
Figure 31. Schematic representation of the structures of the different $Li_xV_2O_5$ phases electrochemically produced in the $0 < x < 2$ composition range. Reprinted with permission from ref 211. Copyright 1994 Elsevier.

Figure 32. Raman spectra of V_2O_5 (a), ε-$Li_{0.52}V_2O_5$ (b), and δ-LiV_2O_5 (c). Excitation with 532 nm radiation. Reprinted with permission from ref 224. Copyright 2006 American Chemical Society.

The intercalation of three lithium ions in V_2O_5 is possible through the formation of a weakly crystallized phase, namely ω-$Li_3V_2O_5$ with a tetragonal[222] or cubic[223] symmetry. However, some authors[225] put in doubt the Li/V_2O_5 phase diagram for $x > 1$, reporting the appearance of a mixture of Li_xVO_2 and Li_3VO_4 compounds instead of the so-called "γ-" and "ω-phase".

A number of structural investigations on the $Li_xV_2O_5$ system have been carried out using different experimental techniques such as X-ray diffraction,[219,225,226] X-ray absorption,[227] NMR,[228] EPR,[229] and neutron and electron diffraction.[230−232] Some researchers have also used Raman spectroscopy to characterize powder[37,45,63,224,233] and thin films[216,234−239] $Li_xV_2O_5$ crystalline phases. The first vibrational *ex situ* study on chemically prepared lithium vanadium pentoxides carried out by Frech et al. focused on the δ-, ε-, and γ-$Li_{0.95}V_2O_5$ compounds.[233] However, only the γ-Raman spectrum can be safely considered, with the other spectra probably corresponding to degradation compounds locally produced under the laser beam. *In situ* experiments were performed by the same authors on a composite γ-$Li_{0.95}V_2O_5$ cathode in an operating rechargeable cell with the aim to study the transformation of γ-LiV_2O_5 into γ'-V_2O_5 and ξ-$Li_2V_2O_5$.[37] Four $Li_xV_2O_5$ samples differing from their intercalation degree during the second discharge process were investigated, but only poor spectral changes were detected, with the Raman spectra recorded for the $x = 0.1$, 0.93, and 1.15 compositions being nearly identical, especially in the high frequency range. *In situ* Raman microspectrometry was successfully applied to characterize a lithium battery involving pure lithium metal at the anode and V_2O_5 powder at the cathode.[45,63] Rey and Lassègues[45] examined a functioning $Li/P(EO)_{20}LiN(SO_2CF_3)_2/V_2O_5$ solid polymer electrolyte lithium cell with *in situ* confocal Raman microspectrometry. The authors provided a quantitative evaluation of salt concentration gradients in the electrolyte and detected polluting species (LiOH, Li_2CO_3, Li_2O, Li_3N) at the lithium electrolyte interface. Conversely, Raman changes of the composite V_2O_5 positive electrode were hampered by fluorescence of the polymer electrolyte. A recent spectro-electrochemical investigation was carried out on a modified coin cell specially designed to facilitate routine *in situ* Raman measurements.[63] Raman spectra were nevertheless limited to the 650−1000 cm^{-1} range, which prevents consistent phase identification, especially in the absence of X-ray diffraction data. However, Burba et al. tentatively assigned
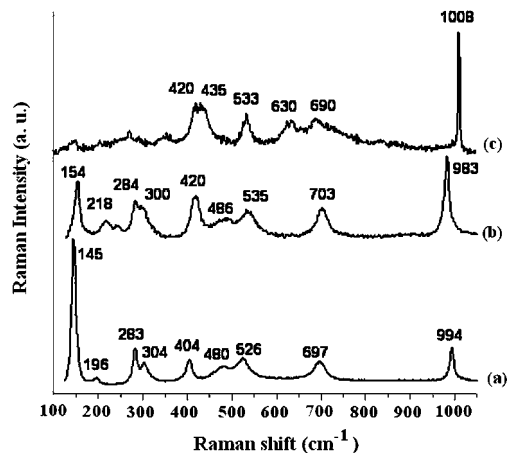
the Raman spectra observed during the first discharge at 2.5 and 2.1 V to the ε- and γ-phases, respectively.

In fact, the literature data related to the Raman features in the Li/V_2O_5 system are very scarce and controversial, essentially due to inappropriate experimental conditions and also because the efficiency of Raman spectroscopy depends on the availability of a relevant band assignment. The spectroscopic data on the lithiated phases have been recently enriched by Raman microspectrometry investigations, which afforded reference Raman spectra for the ε-$Li_{0.5}V_2O_5$, δ-LiV_2O_5, and γ-LiV_2O_5 bulk phases chemically prepared[224] and to follow the structural changes occurring in a $Li_xV_2O_5$ thin film under operation.[216,237,239] We develop in the following the most prominent results extracted from these studies.

Figure 32 shows the Raman spectra obtained for the ε-$Li_{0.5}V_2O_5$ and δ-LiV_2O_5 phases prepared through soft chemistry reduction reactions[224] and compared to that of V_2O_5. The Raman spectrum of ε-$Li_{0.52}V_2O_5$ exhibits several spectroscopic changes: the intensity of the translational mode is strongly quenched, and its wavenumber is shifted from 145 to 154 cm^{-1}. Several modes in the 200−700 cm^{-1} range are also shifted toward higher wavenumber: 196−218 cm^{-1}, 404−420 cm^{-1}, 480−486 cm^{-1}, 526−535 cm^{-1}, 697−703 cm^{-1}. Conversely, the V=O stretching mode along the c axis decreases in frequency from 994 to 983 cm^{-1}. This shift in frequency has been shown to be consistent with the lengthening of the V=O bond from 1.58 Å for the α-phase to 1.6 Å for the ε-phase.

The Raman spectrum of δ-LiV_2O_5 can also be compared with that of V_2O_5 (Figure 32 and Table 7). The low intensity of the bands in the low-frequency part of the Raman spectrum, as well as the broadening of the bands, indicates that the δ- phase is less ordered than the α- and ε-lattices. It is seen also that the same single line, corresponding to the V=O stretching mode along the c axis, dominates the high-frequency part of the Raman spectra. In the spectrum of the δ-phase, this line is narrow and shifted up to 1008 cm^{-1} with respect to 994 cm^{-1}, typically observed for the α-phase. This line can serve as a spectral fingerprint of the δ-phase. Other marked distinctions of the Raman spectrum of this phase are the presence of the peak at 630 cm^{-1} and the disappearance of the peak at 480 cm^{-1}. The Raman features of the δ-phase reflect the particularity of this structure. As

Table 7. Wavenumbers (in cm⁻¹) of Raman-Active Modes Observed for the α-, ε-, δ-, and γ-Phases of Li$_x$V$_2$O$_5$ Samples[a]

α-V$_2$O$_5$	ε-Li$_{0.52}$V$_2$O$_5$	δ-LiV$_2$O$_5$	γ-LiV$_2$O$_5$
145vs	154s	145vw	145
196vw	218w	271vw	**171**, **197**
283s	284m	355vw	209
304s	300m	420s	**271**, **282**
404s	420s	435s	**301**, **327**
480m	486w	533s	376
526s	535m	630m	404
697s	703s	690m	482
994s	983s	837vw	528
		1008vs	546
			647
			703, **737**
			881
			947
			966
			992, **997**

[a] vs, very strong; s, strong; m, medium; w, weak; vw, very weak. Reprinted with permission from ref 224. Copyright 2006 American Chemical Society.
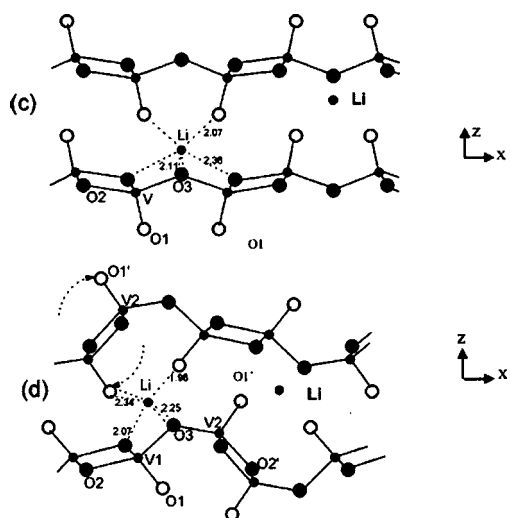

Figure 33. Crystal structures of δ-LiV$_2$O$_5$ (c) and γ-LiV$_2$O$_5$ (d) in the *xz*-projection. Reprinted with permission from ref 224. Copyright 2006 American Chemical Society.

shown in Figure 33, the O1−O1 distances in the δ-phase (2.77 Å) are markedly shorter than those in the α- and ε-phases (3 Å). The relatively high wavenumber of the V=O stretching mode could reflect the steric V=O repulsion, which becomes very strong in the δ-phase because of pronounced layer puckering.

Raman spectroscopy has allowed the investigation of the δ → ε → γ phase transitions during appropriate heat-treatment. X-ray diffraction measurements[224] showed that δ → ε phase transition is initiated around 100 °C and that ε → γ transformation proceeds from 135 °C. The δ → ε transformation ends at 170 °C, with the ε- and γ-phases being simultaneously present. Finally, at 250 °C, the complete transformation of ε into γ-LiV$_2$O$_5$ is achieved. These results are consistent with those recently reported using a synchrotron X-ray powder analysis.[240]

The evolution of the Raman spectrum of δ-LiV$_2$O$_5$ vs temperature in the 100−250 °C range (Figure 34) shows that the δ → ε transformation begins from 100 °C, as indicated by the emergence of the high frequency band at 975 cm⁻¹. Up to 170 °C, both δ- and ε-phases coexist, with the δ-phase growing at the expense of the ε-phase. At this temperature,
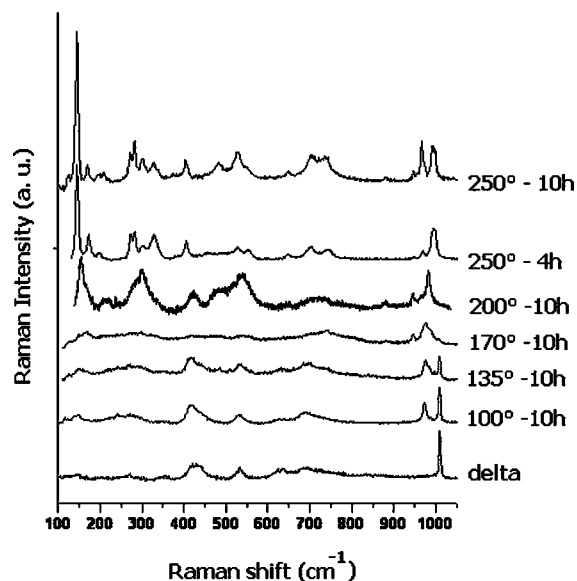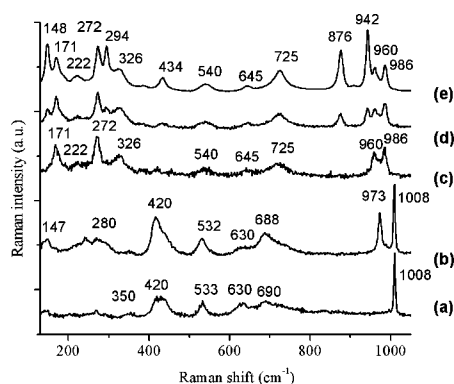

Figure 34. Raman spectra of heat-treated δ-LiV$_2$O$_5$ at different temperatures. Excitation with 532 nm radiation. Reprinted with permission from ref 224. Copyright 2006 American Chemical Society.
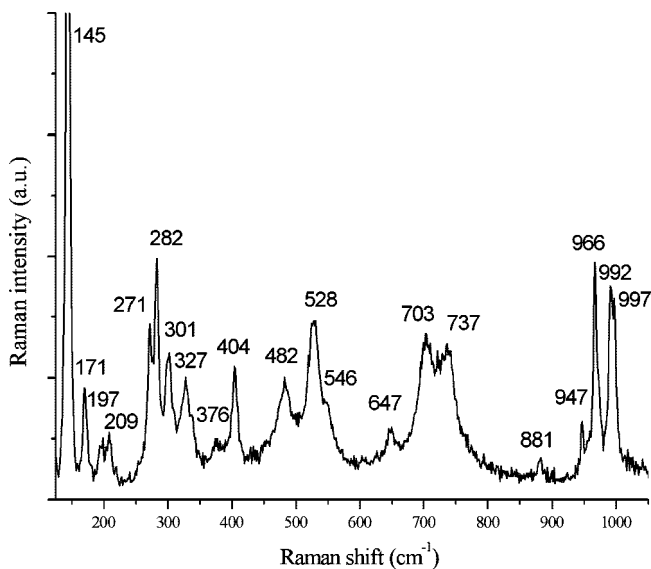
Figure 35. Raman spectrum of γ-LiV$_2$O$_5$. Excitation with 532 nm radiation. Reprinted with permission from ref 224. Copyright 2006 American Chemical Society.

the nucleation of the γ-phase begins, as evidenced by the appearance of a new feature at 945 cm⁻¹. At 200 °C, the Raman spectrum changes drastically, with the emergence of intense and well resolved Raman features in the whole wavenumber range showing the crystallization of the γ-LiV$_2$O$_5$ phase. The ε → γ transformation ends at 250 °C, as indicated by the disappearance of the 985 cm⁻¹ band. Raman data for the resulting γ-LiV$_2$O$_5$ phase are reported in Figure 35 and Table 7. It follows that the thermal treatment of the δ-phase at 250 °C allows us to obtain the pure γ-phase LiV$_2$O$_5$, with lattice parameters $a = 9.69$ Å, $b = 3.60$ Å, and $c = 10.67$ Å (Table 6). These values are in good agreement with those previously reported.[219−221] The space group of the γ-LiV$_2$O$_5$ crystal is *Pnma* (D_{2h}^{16}). The *xz*-projection of this structure is shown in Figure 33d. As in the α and δ-phases, V$_2$O$_5$ layers are perpendicular to the *z*-axis and built up of V−O$_2$ ladders connected by V−O−V bridges. Likewise, in the δ-phase, the layers are alternatively

Figure 36. Raman spectra of (a) δ-LiV$_2$O$_5$ powder illuminated with a laser power of 0.2 mW. (b) δ- and ε- phases observed under a laser power of 0.6 mW. (c) ε- and γ- phases observed under a laser power of 0.8 mW with an integration time of 20 s. (d) γ-phase observed under a laser power of 0.8 mW with an integration time of 90 s. (e) γ-phase observed under a laser power of 0.8 mW with an integration time of 900 s. Excitation with 532 nm radiation. Reprinted with permission from ref 224. Copyright 2006 American Chemical Society.

shifted on the vector $b/2$ and the unit cell of this structure is doubled in the z-direction; however, the structure of the γ-phase differs from the structure of the δ-phase markedly. The Li atoms are shifted in the x-direction from their symmetric positions in the δ-phase. This is accompanied by important deformations of the V$_2$O$_5$ layers. Each second ladder undergoes a strong transformation: it rotates along the y-axis and the O atoms of neighboring vanadyl groups exchange their positions. These displacements are shown by curved arrows. As a result of such a deformation, two nonequivalent V positions (labeled as V1 and V2) appear and the V1$-$O3$-$V2 bridges become strongly nonsymmetric.

The Raman wavenumbers observed for the γ-LiV$_2$O$_5$ polycrystalline powder are in good agreement with those previously measured for a LiV$_2$O$_5$ single-crystal.[241] Furthermore, on comparing the Raman features of γ-LiV$_2$O$_5$ and V$_2$O$_5$ (Table 7), the following considerations can be drawn: first, all the main spectral features observed in V$_2$O$_5$ can be clearly discriminated in the spectrum of γ-LiV$_2$O$_5$. Second, some bands, which have a singlet form in the Raman spectrum of V$_2$O$_5$ and ε- and δ-V$_2$O$_5$, are clearly 2-fold split in the spectrum of γ-LiV$_2$O$_5$. Third, some new spectral features not seen in the Raman spectrum of V$_2$O$_5$ can be detected in the spectrum of γ-LiV$_2$O$_5$ (bands at 209, 376, 546, 647, 881, and 966 cm^{-1}). At least two factors can account for the distinction between the spectra of these crystals. First, the nonequivalent character of the ladders in the lattice of γ-LiV$_2$O$_5$, inducing two kinds of vanadium environments, must lead to the 2-fold splitting. Second, the Li atom oscillations may couple with some modes of the V$_2$O$_5$ lattice.

A very interesting point which has to be outlined is the possibility for the Raman microprobe to induce *in situ* phase transitions, only by increasing the power of the incident laser beam illuminating the sample. This effect is well illustrated in Figure 36, where the spectral changes observed are related to the successive $\delta \rightarrow \varepsilon \rightarrow \gamma$ phase transitions. It is noteworthy that the γ-phase formation is achieved at a laser power less than 1 mW, as a result of the great instability of the δ-phase. This peculiarity is at the origin of numerous misinterpretations in the literature, with the Raman response being strongly affected by this severe experimental artifact.
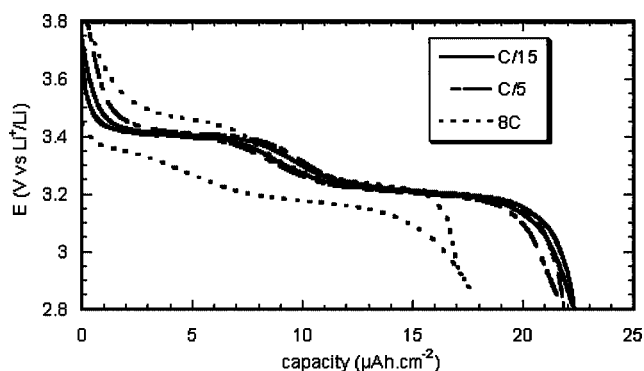
Figure 37. First discharge$-$charge cycles of a V$_2$O$_5$ thin film (thickness 0.6 μm) at different C rates. Reprinted with permission from ref 216. Copyright 2008 American Chemical Society.

4.4.3. Li$_x$V$_2$O$_5$ Crystallized Thin Films

As for bulk oxides in composite electrodes, the electrochemical properties of pure thin films are strongly dependent on the structural changes induced by the lithium insertion reaction. Several studies carried out on polycrystalline films[242$-$247] seem to show that the structural features of the lithiated Li$_x$V$_2$O$_5$ phases can be significantly different from that known for the bulk material. *In situ* and *ex situ* XRD experiments performed on sol$-$gel,[226,246,247] electrodeposited,[244,245] and sputtered[242,243,248,249] Li$_x$V$_2$O$_5$ films have shown the existence of an unexpected elongated c axis for $x = 0.8$ as well as the nonappearance of the δ-phase usually observed[213] in bulk samples from $x \approx 0.6/0.7$.

On the other hand, few Raman spectroscopy studies have been carried out on polycrystalline V$_2$O$_5$ films.[234$-$239] Fast amorphization of the sputtered oxide was observed,[234] with the V$_2$O$_5$ lines vanishing nearly completely from the early lithium content, whereas practically no change seemed to take place in the PLD film in the $0 < x < 1$ composition range.[235] Moreover, only two compositions were reported by Ramana et al.,[235] and the Raman spectra were simply assigned on the basis of the phase diagram known for the bulk material. We develop in the following recent results obtained from *ex situ* and *in situ* Raman spectroscopic analysis of crystallized V$_2$O$_5$ thin films prepared by radio frequency magnetron reactive sputtering without any heat treatment,[216,239] with particularly attractive electrochemical properties.[248$-$251] A specific structural response was evidenced for such films, which strongly contrasts with that known for bulk samples.

The galvanostatic discharge$-$charge curves of a 0.6 μm sputtered thin film (Figure 37) show two well-defined insertion steps located at about 3.4 and 3.2 V, as expected for the crystalline form of V$_2$O$_5$. The value of the specific capacity recovered at C/15 rate, 22 μAh/cm^2, corresponds to the accommodation of 0.94 Li$^+$ ion per mole of oxide. This insertion reaction is reversible, as shown from the lack of polarization and the efficiency of 100% in the charge process. No influence of the current density on the discharge potential and capacity is seen from C/15 up to C/5 rate, and the specific capacity is seen to decrease by only $\approx$18% when the C rate increases from C/15 to 8C. Moreover, the polarization observed at high rate never exceeds 150 mV, which suggests a high kinetics of lithium transport.

Figure 38 pertains to Raman spectra with different x values in Li$_x$V$_2$O$_5$ thin films. Examining the $0 \leq x \leq 0.5$ composition range, several comments can be made: (i) The intensity
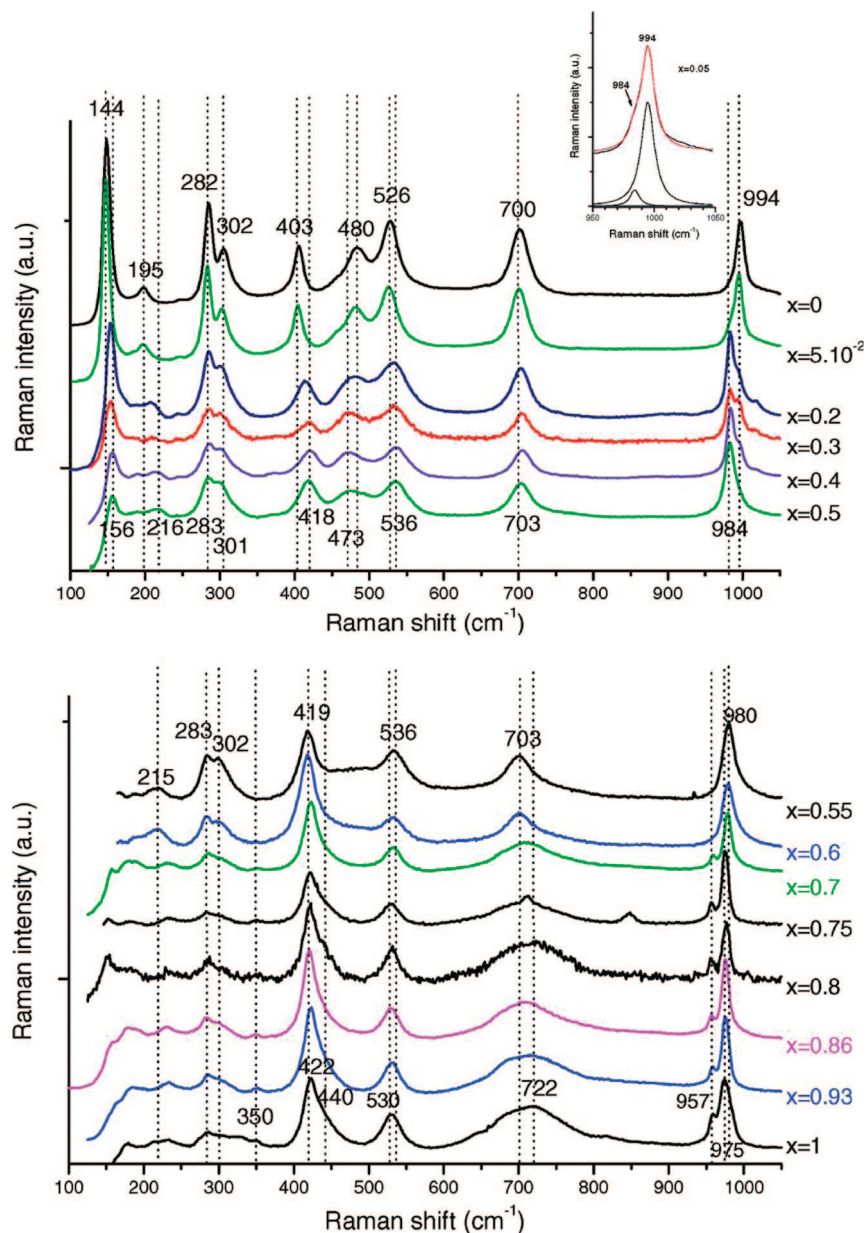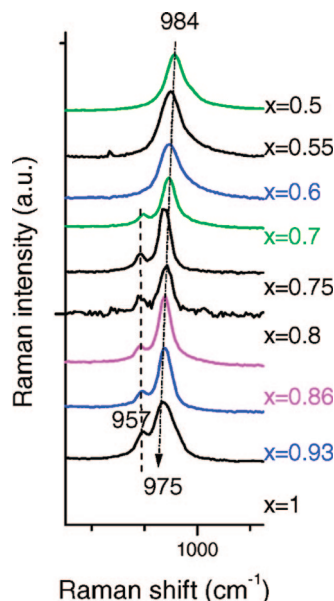
Figure 38. Raman spectra of a galvanostatically lithiated $Li_xV_2O_5$ thin film, $0 \leq x \leq 1$. Excitation with 532 nm radiation. Reprinted with permission from ref 216. Copyright 2008 American Chemical Society.

of the translational mode at low frequency is progressively quenched, and its wavenumber is shifted from 145 to 153 cm^{-1} for $x = 0.5$. (ii) A significant loss of intensity is observed in the $200-700$ cm^{-1} range. (iii) In the vanadyl stretching frequency range, a new component at 985 cm^{-1} appears from the first lithium content, which continuously increases in intensity at the expense of the 997 cm^{-1} band and shifts up to 980 cm^{-1} for $x = 0.5$ (Figure 39). (iv) Several modes in the $400-800$ cm^{-1} range are progressively shifted toward higher wavenumber (Figures 38 and 40): 404 to 420 cm^{-1}, 527 to 533 cm^{-1}, 702 to 705 cm^{-1}. Conversely, the 482 cm^{-1} band gradually shifts toward lower wavenumbers, up to 470 cm^{-1} for $x = 0.33$, and then completely disappears. (v) The two lines at 282 and 303 cm^{-1} do not undergo any frequency shift but progressively broaden to give rise to a single and broad band centered at 290 cm^{-1} for $x = 0.5$.

In the $0.5 \leq x \leq 0.94$ composition range, the whole Raman spectrum of the $Li_xV_2O_5$ film electrode is little affected. The stretching mode at 980 cm^{-1} remains unchanged in frequency, while a new line at 958 cm^{-1} appears from $x =$

0.75. In addition, the 533 cm^{-1} band shifts to 527 cm^{-1} whereas the 705 cm^{-1} line gives rise to a broad and asymmetric signal centered around 730 cm^{-1}.

It follows that the structural variations depicted all along the lithium insertion process from the Raman microprobe consist in rather moderate local distortions which allow the thin film material to accommodate up to 0.94 Li/mol of oxide without breaking of the orthorhombic symmetry. These structural changes consist mainly in (i) an increase of disorder within the V_2O_5 layers, as suggested by the significant decrease in intensity of the 145 cm^{-1} mode and the significant loss of intensity observed in the $200-700$ cm^{-1} range; (ii) a weakening of the vanadyl stretching mode, illustrated by the shift in frequency of the apical $V-O_1$ stretching mode toward lower frequency values; (iii) a stiffening of the lattice along the a direction, suggested by the shift of the 404 and 527 cm^{-1} modes, which both come from oxygen displacements along the a axis. These changes may reflect the puckering of the V_2O_5 layers, as indicated by the observed decrease of the a parameter from 11.51 to 11.35 Å when the lithium

**Figure 39.** Enlarged view in the high-frequency range of the Raman spectra of a galvanostatically lithiated $Li_xV_2O_5$ thin film, $0.5 < x < 1$. Excitation with 532 nm radiation. Reprinted with permission from ref 216. Copyright 2008 American Chemical Society.

content increases from 0 to 0.55.[249] In the $0.5 \leq x \leq 0.94$ composition range, the Raman spectra fit well with that previously reported for $\varepsilon Li_{0.5}V_2O_5$ and εLiV_2O_5 powders.[224] Moreover, the new line observed at 958 cm^{-1} for the highest lithium uptakes ($x \geq 0.75$) is well consistent with the presence of an additional kind of vanadium atom in the epsilon lithium-rich phase. Indeed, although the lithium positions in the ε-phase remain to be determined accurately, a unique type of lithium site has been described for the whole ε phase domain. It consists of elongated cuboctahedra joining common faces,[252] with the symmetry of such sites remaining unchanged with x. It was however reported that increasing the amount of lithium in the ε-phase leads to a lithium-rich phase (called ε') in which the lithium environment is modified:[219,231,252−254] for lithium amounts below $x = 0.5$, the number of unoccupied cuboctahedra exceeds the number of occupied octahedral, whereas, above $x = 0.5$, neighboring cuboctahedra have to be occupied. This induces a change in the interatomic Li−Li distances: the shortest Li−Li distance decreases from 7.2 Å for $x < 0.5$ to 3.6 Å for $x > 0.5$.[219]

As shown in Figure 41, *in situ* Raman microspectrometry experiments performed on sputtered thin films[239] confirm the data obtained from *ex situ* measurements. The *in situ* Raman spectra of thin film electrodes collected along the galvano-static charge process (Figure 42) show a progressive and complete recovery of the whole characteristic Raman features of the pure V_2O_5 lattice, in terms of both intensities and frequencies. Such a finding is in good agreement with the excellent electrochemical reversibility evidenced in the 3.8/2.8 V potential range.[248−251]

One of the major findings of this Raman investigation is that the expected lithiated δ phase, which exhibits a strong line at 1008 cm^{-1} for $x > 0.5$,[224] is never identified in the V_2O_5 thin film electrode. Instead of that, in the $0.5 \leq x \leq 0.94$ composition range, both the Raman and XRD experiments provide evidence for the existence of a solid solution behavior, with the interlayer c parameter of the ε-phase varying to an unusually large extent, up to 4.68 Å. This lattice parameter value corresponds to that known for the chemically
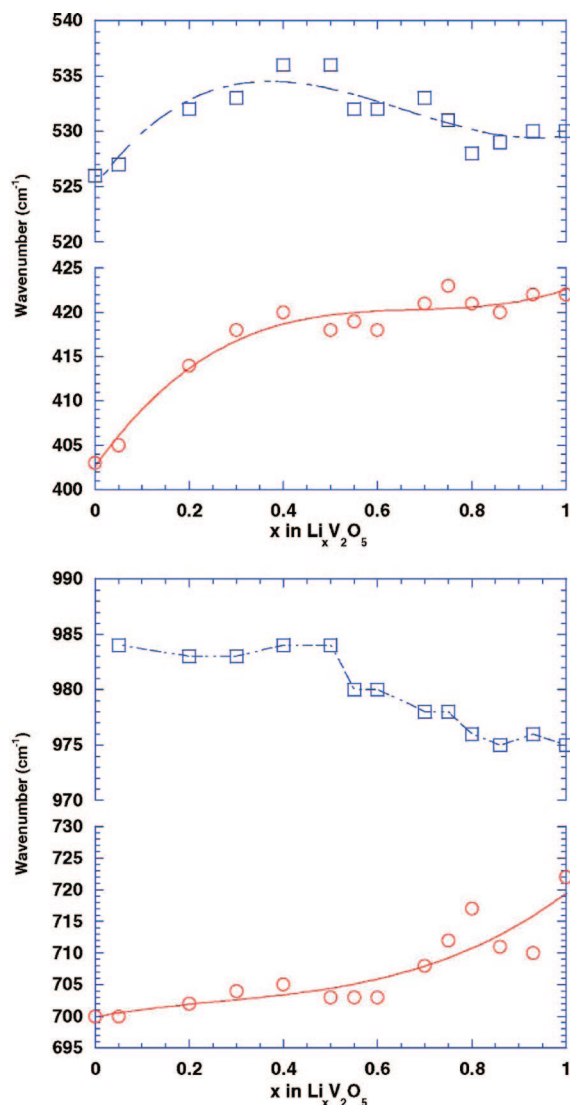
Figure 40. Evolution of the Raman band wavenumbers at 403, 526, 700, and 984 cm^{-1} as a function of x in the $Li_xV_2O_5$ thin film, $0 < x < 1$. Reprinted with permission from ref 216. Copyright 2008 American Chemical Society.

formed εLiV_2O_5.[220] This result strongly contrasts with the more pronounced structural changes described for the conventional composite V_2O_5 cathode,[213] with the emergence of one- and two-phase domains as well as the formation of the δ phase from $x \approx 0.6/0.7$. The lower magnitude of the structural changes evidenced for the thin film electrode can be ascribed to the nanosize effect of V_2O_5 planes with a cross section of 40 nm × 200 nm stacked perpendicular to the substrate. Hence, a more homogeneous Li insertion reaction takes place in the present films, avoiding the local over-lithiation phenomenon. This favors a better relaxation of the host lattice and a lower structural stress.

4.5. Titanium Oxide-Based Compounds

In the framework of the research for new electrode materials for lithium batteries, negative electrode materials have to be developed working at a higher potential than that of the currently used carbon or graphite electrodes ($\sim$1 V vs Li), which are to be replaced for safety reasons.[255] Titanium oxides with the Ti^{4+}/Ti^{3+} redox couple working at approximatively 1.5 V vs Li/Li^+ fulfill this requirement. We will focus on lithium titanate $Li_4Ti_5O_{12}$ and anatase TiO_2.
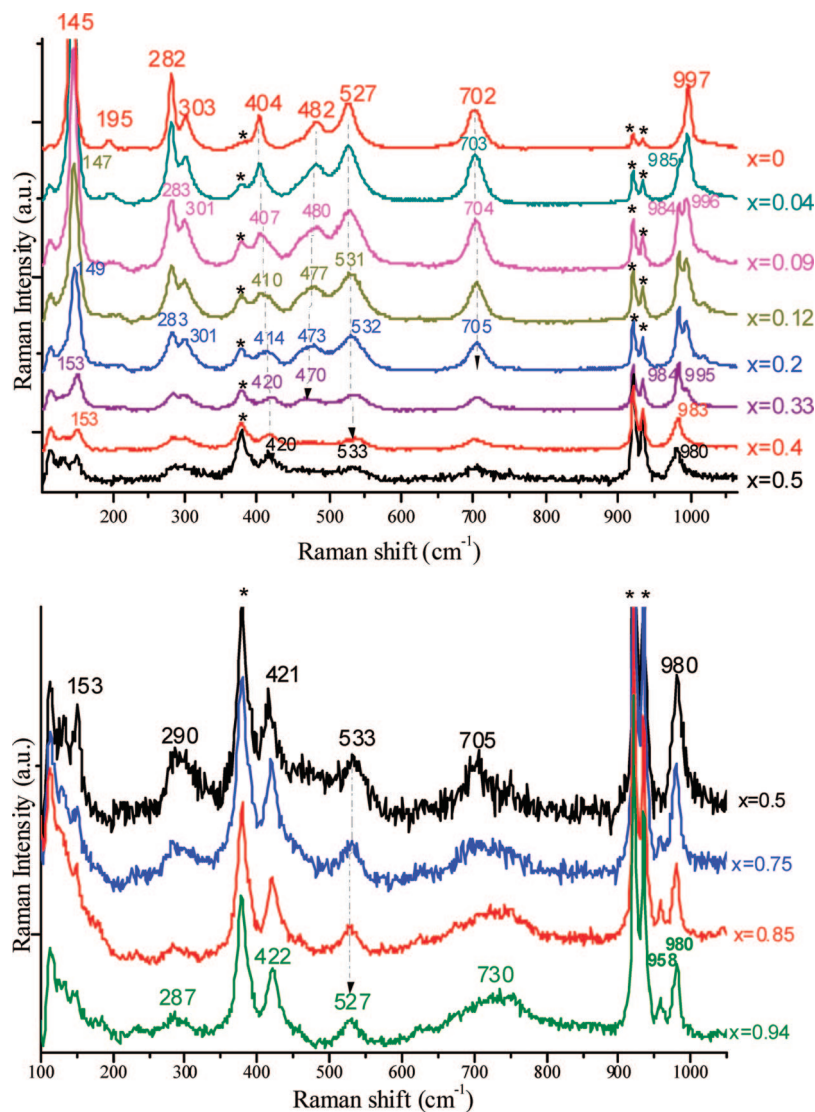
Figure 41. Detailed view of the *in situ* Raman spectra collected during the first discharge of a $Li_xV_2O_5$ thin film electrode. $0 \leq x \leq 0.94$. Excitation with 532 nm radiation. *$LiClO_4/ACN$ bands.

4.5.1. Lithium Titanate $Li_4Ti_5O_{12}$

Lithium titanates, which are known in the spinel and the ramsdellite form, are interesting candidates as negative electrodes in Li ion batteries. Presently, they are being evaluated for use in the next generation of secondary lithium cells. The most widely considered metal oxide for low potential applications is spinel $Li_{4/3}Ti_{5/3}O_4$ ($Li_4Ti_5O_{12}$),[255−263] reported as a zero strain insertion compound.[255−258] This material shows an extremely flat voltage plateau at 1.55 V (Figure 43), allowing the reversible insertion of 0.8 to 1 Li per $Li_{4/3}Ti_{5/3}O_4$ formula unit, leading to a theoretical specific capacity of 175 (mA h)/g, with an exceptional cycling stability.[257] The demonstration of the use of $Li_4Ti_5O_{12}$ as a negative electrode in a high-power lithium battery with safety has been done. Excellent cycle life was achieved for $Li_4Ti_5O_{12}//LiCoO_2$ cells.[262]

The constant working potential of this material suggests a two-phase reaction between the defect spinel $Li_{4/3}Ti_{5/3}O_4$ and the fully lithiated $Li_{7/3}Ti_{5/3}O_4$ according to the general equation proposed by Ohzuku et al.:[258]

$$(Li)_{8a}(Li_{1/3},Ti_{5/3})_{16d}O_4 + e^- + Li^+ \rightleftarrows$$
$$(Li_2)_{16c}(Li_{1/3},Ti_{5/3})_{16d}O_4$$
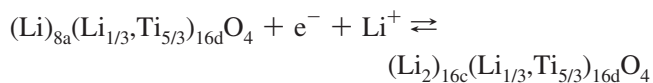
Both lithium titanium oxides crystallize in the $Fd\bar{3}m$ space group (Figure 44). In the structure of the spinel $Li_{4/3}Ti_{5/3}O_4$, the octahedral 16d sites are randomly occupied by Li^+ and Ti^{4+} whereas the tetrahedral 8a positions are occupied by Li^+. Insertion of additional lithium transforms the spinel $Li_{4/3}Ti_{5/3}O_4$ into a structure of the NaCl type, $Li_{7/3}Ti_{5/3}O_4$, by incorporation of the inserted lithium into octahedral 16c positions. Simultaneously, the tetrahedral Li^+ ions of $Li_{4/3}Ti_{5/3}O_4$ are shifted to 16c positions. Hence, in the rock-salt $Li_{7/3}Ti_{5/3}O_4$ phase, the octahedral 16c positions are occupied by lithium, and the occupancy of the octahedral 16d positions is the same as in $Li_{4/3}Ti_{5/3}O_4$, but in contrast, the tetrahedral 8a positions are not occupied.

The difference in the unit cell volume of $Li_{4/3}Ti_{5/3}O_4$ and lithium-rich $Li_{7/3}Ti_{5/3}O_4$ is extremely small. For instance, on studying the structural changes as lithium accommodation proceeds in $Li_{4/3+x}Ti_{5/3}O_4$ using XRD, Bach et al.[260] reported only a negligible modification in the cubic cell parameter, from 8.344 Å for $x = 0$ to 8.357 Å for $x = 0.9$. These results have been confirmed by Scharner et al.,[263] which show the ordered rock-salt structure of lithiated $Li_{7/3}Ti_{5/3}O_4$ using high angle X-rays scans.

Raman data on lithium titanium oxide spinels are very scarce.[264−268] The vibrational analysis of $Li_4Ti_5O_{12}$ can be
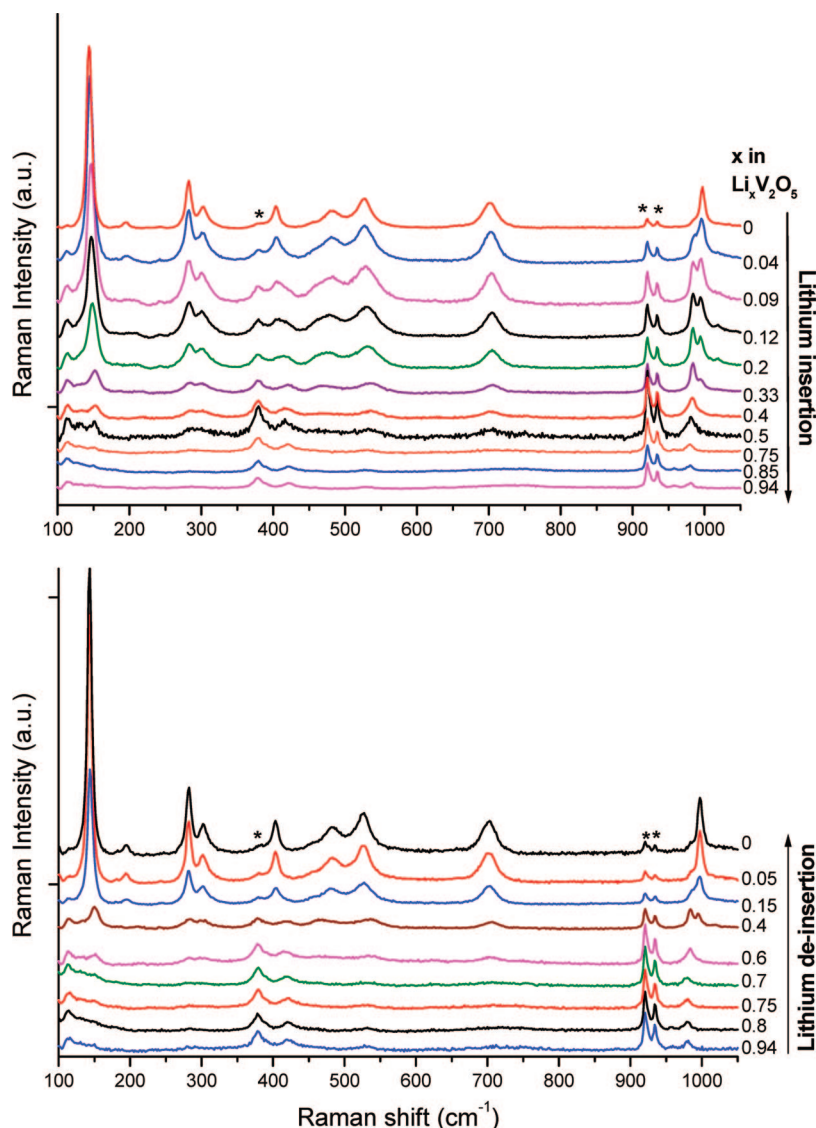
Figure 42. *In situ* Raman spectra series of the first discharge−charge process of a $Li_xV_2O_5$ thin film electrode. $0 \leq x \leq 0.94$. Excitation with 532 nm radiation. *$LiClO_4$/ACN bands.
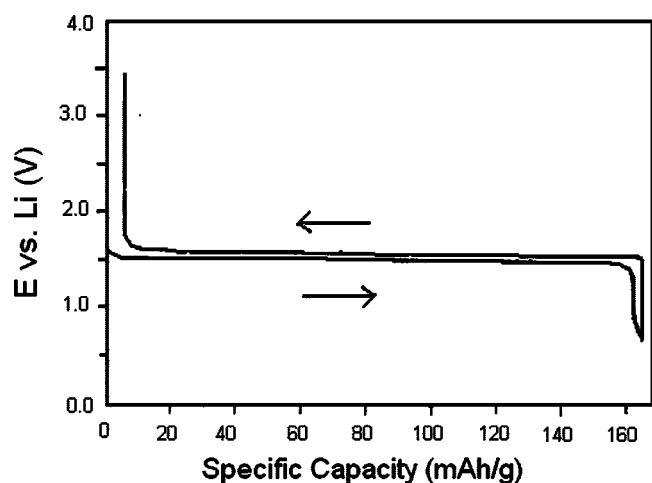
Figure 43. Typical charge and discharge curve of a $Li_{4/3}Ti_{5/3}O_4$ pellet. C rate: 2.1 mA/g. Reprinted with permission from ref 263. Copyright 1999 The Electrochemical Society.

done using the factor-group theoretical treatment of normal $A[B_2]O_4$ spinel-type compounds (O_h^7), which predicts five optic mode Raman-active vibrations $A_{1g} + E_g + 3F_{2g}$ (see Table 3). While studying the superconducting $Li_{1+x}Ti_{2-x}O_4$

system,[266] Liu et al. reported five phonon bands for polycrystalline $Li_{4/3}Ti_{5/3}O_4$, with slightly different frequencies compared to those of Leonidov et al.,[265] that is three main lines centered at 239, 427, and 675 cm^{-1} and weak features at 274 and 367 cm^{-1} (Figure 45).

Proskuryakova et al.[264] and Leonidov et al.[265] analyzed the Raman spectrum of the $Li_4Ti_5O_{12}$ spinel. Six Raman bands were observed at room temperature, at 160, 235, 335, 430, 675, and 740 cm^{-1}, with the most intense lines being located at 235, 430, and 675 cm^{-1}. The authors propose a qualitative band assignment in the following terms: the higher frequency bands at 675 and 740 cm^{-1} were assigned to vibrations of Ti−O bonds in TiO_6 octahedra whereas the 440 and 335 cm^{-1} Raman lines were assigned to the stretching vibrations of the Li−O bonds in LiO_4 and LiO_6 polyhedra, respectively. The Raman bands below 300 cm^{-1} were attributed to the bending vibrations of O−Ti−O bonds (235 cm^{-1}) and O−Li−O bonds (160 cm^{-1}).

A Raman spectrum of a pristine $Li_4Ti_5O_{12}$ electrode reported by Julien et al. was found to display bands at 671, 430, 347, 271, and 232 cm^{-1} which were tentatively assigned to the five expected A_{1g}, F_{2g}, and E_g symmetry species for the spinel O_h^7 spectroscopic point symmetry group.[267] It is
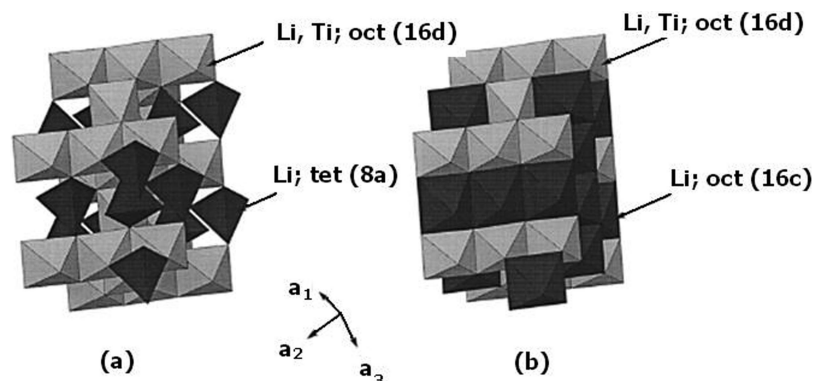
Figure 44. (a) Crystal structure of $Li_{4/3}Ti_{5/3}O_4$ (space group $Fd\bar{3}m$). (b) Crystal structure of $Li_{7/3}Ti_{5/3}O_4$ with the space group $Fd\bar{3}m$. Reprinted with permission from ref 263. Copyright 1999 The Electrochemical Society.
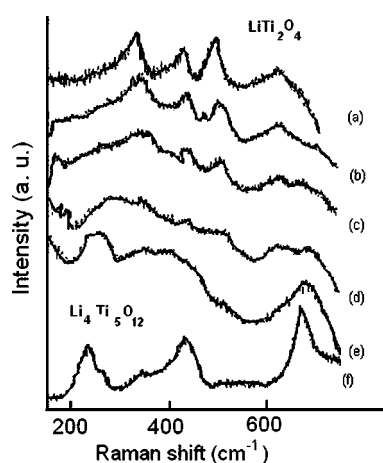
Figure 45. Raman spectra of polycrystalline $Li_{1+x}Ti_{2-x}O_4$ powders showing the end members (a) $LiTi_2O_4$ and (f) $Li_{4/3}Ti_{5/3}O_4$. Excitation with 514.5 nm radiation. Reprinted with permission from ref 266. Copyright 1994 Elsevier.

Figure 46. Raman spectra of a $Li_{4+x}Ti_5O_{12}$ electrode at different Li uptake. Excitation with 514.5 nm radiation. Reprinted with permission from ref 267. Copyright 2004 Elsevier.

noteworthy to outline the very weak Raman intensity of this spectrum in the low frequency region compared to other reported Raman data.[265,266]

In contrast to the Li−Mn−O system, there is practically no Raman data related to electrochemical lithium insertion in titanate spinels. This is probably due to the lack of theoretical analysis based on lattice dynamics simulation, which prevents a consistent analysis of the vibrational features exhibited by the rock-salt lithium-r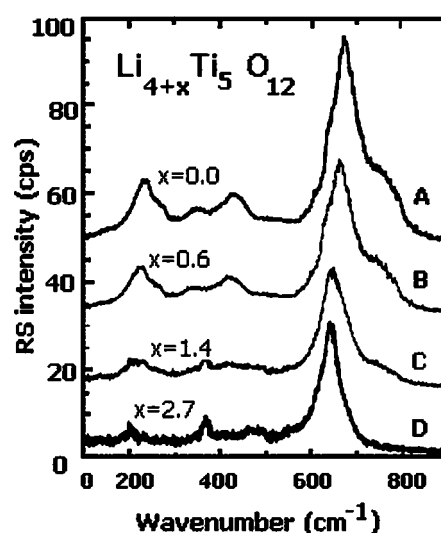ich compound. Raman spectra have been reported[267] for a $Li_{4+x}Ti_5O_{12}$ electrode material electrochemically reduced up to $x = 2.7$ (Figure 46). The main effect of lithium insertion is the shift of the strongest component from 675 to 642 cm^{-1} for the fully lithiated material and the decrease of the Raman activity in the low frequency region. However, the authors did not provide any explanation for the observed evolution and proposed instead a tetragonal structure for the fully lithiated $Li_7Ti_5O_{12}$ compound without structural validation. This assertion is rather surprising because factor group theory predicts 14 Raman active modes for the tetragonal D_{4h}^{19} spectroscopic point group. Aldon et al. reported the chemical lithium insertion into the $Li_4Ti_5O_{12}$ spinel.[268] Using XRD, neutron diffraction, NMR, and Raman spectroscopy, the authors proposed a different mechanism for chemical lithium insertion; that is, the spinel to the rock-salt transition would not occur in the chemically inserted phase. The Raman spectrum of the chemically inserted $Li_{5.9}Ti_5O_{12}$ shows an

overall broadening of the lines, changes in wavenumber values, and new features, but these variations are not discussed.

4.5.2. TiO$_2$ Anatase

Titanium dioxide TiO_2 is an interesting candidate for electrode applications in photoelectrochemical solar cells[269] and rechargeable lithium batteries.[270] The tetragonal anatase polymorph of titanium dioxide is of special interest, due to its ability to store a significant amount of Li as well as its insertion potential around 1.5 V. The first *ex situ* XRD investigation of the anatase Li_xTiO_2 system reported the existence of a tetragonal to cubic phase transition,[271] which was not validated by further neutron[272,273] and *in situ* powder X-ray diffraction[274] investigations, which rather invoked a phase transformation toward a Li-rich phase, here referred to as lithium titanate (LT), with orthorhombic symmetry.

As far is known from the literature, spectroscopic data for the anatase bulk have been limited because of the poor availability of single crystals.[275−277] Nevertheless, two Raman spectroscopic studies[275,276] and one IR study[277] made it possible to determine all the zone-center vibrational frequencies. Considering the anatase Li_xTiO_2 system, Raman data are limited to a few studies.[278−282] The main contributions were recently reported on composite powder electrodes.[280−282]

We report here recent results obtained from a Raman study on Li_xTiO_2 composite electrodes ($0 \leq x \leq 0.6$), with the

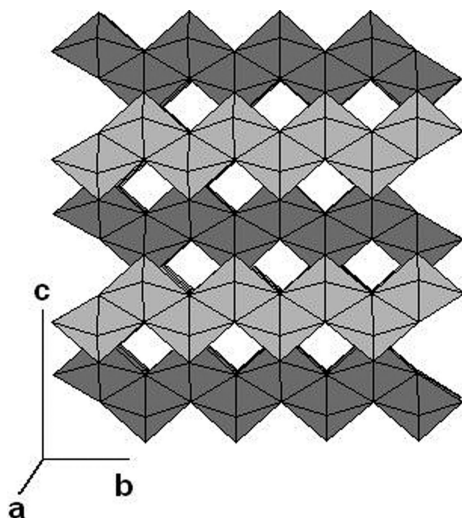**Figure 47.** Schematic structure of TiO_2 anatase.

Table 8. Interatomic distance (in Å) in tetragonal anatase TiO_2 and in orthorhombic lithium titanate $Li_{0.5}TiO_2$ at 10 K. Subscripts eq and ax denote the oxygen coordination in the (a,b) plane and in c direction, respectively. Reprinted from ref 280. Copyright 2004 with permission from Wiley

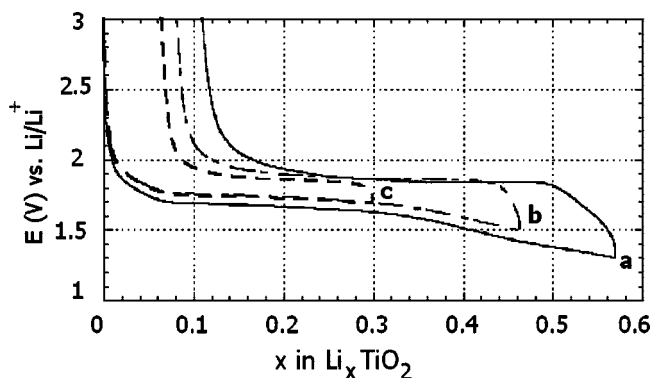| anatase TiO_2 ($I41/amd$)		lithium titanate ($Imma$)	
$4Ti-Ti$	3.0384	$2Ti-Ti$	3.1344
$4Ti-O_{eq}$	1.9367	$2Ti-Ti$	2.8914
$2Ti-O_{ax}$	1.9792	$2Ti-O_{eq}$	1.9416
		$2Ti-O_{eq}$	2.0438
		$1Ti-O_{ax}$	1.9639
		$1Ti-O_{ax}$	2.1331
		$2Li1-O_{eq}$	2.0487
		$2Li1-O_{eq}$	1.9301
		$1Li1-O_{ax}$	2.3697
		$1Li1-O_{ax}$	2.5991
		$2Li2-O_{eq}$	2.1135
		$2Li2-O_{eq}$	2.1465
		$1Li2-O_{ax}$	1.6717
		$1Li2-O_{ax}$	3.2972
		$2Li3-Li3$	2.5473
		$2Li3-Li3$	3.5033

Figure 48. First discharge charge curve at the C/20 rate of a TiO_2 anatase electrode as a function of the depth of discharge in 1 M $LiClO_4$/PC: (a) $x = 0.56$; (b) $x = 0.45$; (c) $x = 0.3$. Reprinted with permission from ref 280. Copyright 2004 Wiley.

pure anatase powder being synthesized via the sol–gel process.[280,281] Structural changes and reversibility will be discussed in relation with structural data drawn from XRD experiments. We will also illustrate through this example the interesting contribution of lattice dynamics simulation to perform a quantitative and thorough analysis of the Raman features.

TiO_2 anatase has a tetragonal symmetry[283] (space group D_{4h}^{19} $I41/amd$, number 141). The unit cell parameters are $a = b = 3.8$ Å; $c = 9.61$ Å. It is known that zigzag chains are formed in the close packed planes due to anion stacking and the half occupancy of the octahedral sites by titanium ions. Each $[TiO_6]$ octahedron shares two adjacent edges with other $[TiO_6]$ units in the (b, c) plane to form infinite, planar double chains parallel to a and b (Figure 47). These double chains share corners with identical chains above and below and are shifted along the c axis with respect to each others. Finally, all $[TiO_6]$ octahedra share four edges, and all oxygen ions are bonded to three titanium ions.

The typical discharge curve of TiO_2 anatase is shown in Figure 48. At a C/20 rate, one main discharge process located at 1.75 V is evidenced and corresponds to the insertion of 0.56 Li ion per mole of oxide according to the reaction:

$$TiO_2 + xe^- + xLi^+ + \ \leftrightarrow Li_xTiO_2$$

The charge process occurs at a higher voltage around 1.9 V. The efficiency (Q_{ox}/Q_{red}) of the intercalation process in

the anatase is around 80%. These electrochemical data show that the extraction of lithium is only partially quantitative whatever the depth of discharge is.

Several authors have shown that chemical[272,273] or electrochemical[271,274] lithium insertion in the anatase structure induces from the first lithium contents a phase transformation leading to lithiated titanate $Li_{0.5}TiO_2$. Ohzuku et al. reported from XRD powder experiments a cubic symmetry for the $Li_{0.5}TiO_2$ compound.[271] However, recent works based on X-ray[274] and neutron[272,273] diffraction found an orthorhombic structure for lithiated titanate $Li_{0.5}TiO_2$, indexed with the $Imma$ space group.

In fact, the initial anatase structure with tetragonal symmetry and the new orthorhombic lithiated titanate structure have very close diffraction patterns. The orthorhombic lithiated titanate consists of edge-sharing TiO_6 octahedra giving rise to an open structural framework. The lithium ions are located between the TiO_6 octahedra within the octahedral voids. The overall orthorhombic distortion of the atomic positions in the change from anatase to lithium titanate is small. XRD studies[272,273,280] showed the following changes in the unit cell dimensions of the anatase structure upon lithiation: from $a = b = 3.8$ Å, $c = 9.61$ Å to $a = 3.81$ Å, $b = 4.07$ Å, $c = 9.04$ Å. In lithium titanate, the a and b axes become different in length by about 7%, mainly increasing in the b direction and decreasing in the c direction by 9%. Examination of the interatomic distances (Table 8) reveals that the anatase structure is deformed upon lithiation. This entails a lowering of symmetry by loss of the C_4 axis on going from the pristine TiO_2 tetragonal $I41/amd$ to the orthorhombic $Li_{0.5}TiO_2$ $Imma$ structure.

According to Cava et al.,[272] the Li ions in the orthorhombic phase are randomly located in about half of the available interstitial octahedral 4e sites. This suggestion was also deduced from theoretical calculations.[284] Hence, only a maximum uptake of 0.5–0.6 Li^+ ions per mole of TiO_2 can be inserted in the lithiated titanate structure at room temperature. This result agrees with recent quantitative NMR findings[285] and with the composition value of the electrochemically formed $Li_{0.56}TiO_2$ orthorhombic phase.[280]

The Raman spectra observed for different Li_xTiO_2 ($0 \leq x \leq 0.6$) compositions are shown in Figure 49. Corresponding wavenumbers of the Raman bands are reported in Table 9. At low Li concentration (up to $x = 0.15$), the Raman
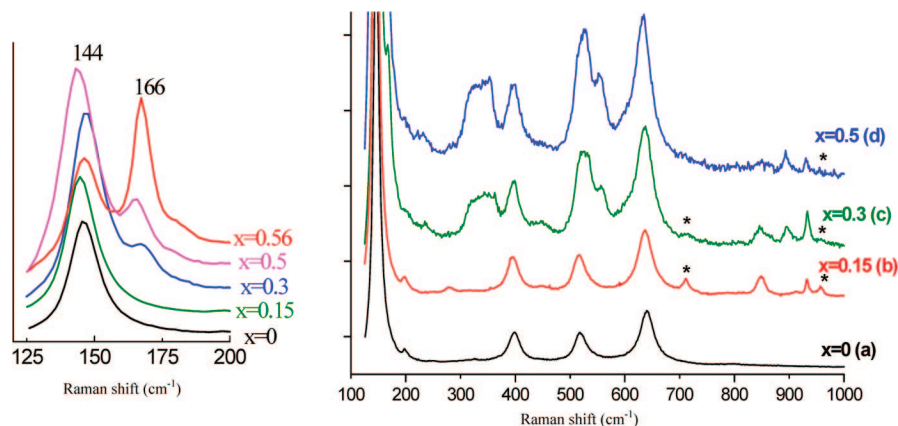
Figure 49. Raman spectra of electrochemically lithiated Li_xTiO_2 ($x = 0$; 0.15; 0.3; 0.5; 0.56). * indicates PC/LiClO$_4$ vibrational bands. Excitation with 514.5 nm radiation. Reprinted with permission from ref 280. Copyright 2004 Wiley.

Table 9. Raman Wavenumbers (in cm^{-1}) Observed for a Discharged Li_xTiO_2 Electrode[a]

$x = 0$	$x = 0.15$	$x = 0.3$	$x = 0.5$
144s	144s	144s	144s
		166w	166m
198	198	233vw	233vw
		320−335b	320−335b
		357	357
398	397	397s	397s
	450w	450b	450b
518	518	525	525
		559	559
639	637	637	634
	848	847	847
		897	894
934	930		

[a] Reprinted with permission from ref 280. Copyright 2004 Wiley. s, strong; m, medium; w, weak; b, broad.

spectrum is very close to that of the pure titanium oxide. Only a complex band structure in the high frequency region seems to indicate the presence of a new system. Along with increasing x up to $x = 0.3$ and $x = 0.5$, several spectroscopic changes are observed: (i) The main bands of pure anatase (144, 398, 518, and 639 cm^{-1}) are clearly observed; however, the band at 518 cm^{-1} shifts to 525 cm^{-1} and the band at 639 cm^{-1} slightly shifts to 634 cm^{-1}. (ii) Several new bands appear: a complex band structure in the high wavenumber region, a band at 559 cm^{-1} whose intensity increases with x, another broad-band structure around 320−330 cm^{-1}, and two bands in the low wavenumber region at 166 and 233 cm^{-1}.

According to the factor group analysis,[275] the 15 normal modes of TiO_2 anatase have the irreducible representation $1A_{1g} + 1A_{2u} + 2B_{1g} + 1B_{2u} + 3E_g + 2E_u$. The A_{1g}, B_{1g}, and E_g modes are Raman active, and thus, six fundamental transitions are expected in the Raman spectrum of anatase:

$$\Gamma_{Raman} = 1A_{1g} + 3B_{1g} + 3E_g$$

The typical Raman fingerprint of anatase, shown in Figure 49 curve a, exhibits five Raman bands at 144, 198, 398, 518, and 639 cm^{-1}. The band at 518 cm^{-1} splits into two components at 507 cm^{-1} and 519 cm^{-1} only at 73 K.[275]

Upon increasing the Li concentration in the TiO_2 host lattice, the evolution of the Raman spectra clearly indicates the emergence of a new phase. For low Li content ($x = 0.15$), the local symmetry of pure anatase is conserved, as shown by curve b in Figure 49. Upon increasing the Li concentra-

tion, the modification of the original anatase Raman spectrum indicates a break in the local symmetry, probably due to the appearance of the lithiated phase $Li_{0.5}TiO_2$ with an orthorhombic symmetry (*Imma*). This new phase exhibits several typical Raman bands with wavenumbers listed in Table 9. A good agreement exists with the experimental data recently reported from an *in situ* Raman study on nanosized TiO_2 anatase powders.[282] A Raman study on TiO_2 anatase thin films[278] reported several broad Raman bands, located at 176, 224, 316, 405, 531, and 634 cm^{-1}. However, the vibrations of the propylene carbonate/LiClO$_4$ electrolyte and the ITO substrate hinder most of the Raman spectrum from being observed. Moreover, the authors did not assign the observed new features to the $Li_{0.5}TiO_2$ phase.

The tetragonal-to-orthorhombic structural transition implies a lowering of symmetry of the TiO_2 lattice from D_{4h} to D_{2h}. As a consequence, the A_{1g} and B_{1g} modes of the tetragonal anatase lattice transform into A_g modes, and E_g modes split into B_{2g} (x) and B_{3g} (y) modes of the orthorhombic LT lattice. It has been determined that nine lattice modes are predicted for orthorhombic $Li_{0.5}TiO_2$:

$$\Gamma_{Raman}(\text{LT-lattice}) = 3A_g + 3B_{2g} + 3B_{3g}$$

Due to the small extent of the structural distortion, a quite moderate perturbation of the phonon states of the TiO_2 lattice can be expected. However, the coupling between TiO_2 lattice modes and vibrations of the Li atoms will cause considerable changes in the Raman spectrum, giving rise to the emergence of new modes assigned to lithium vibrations and band splitting due to perturbed lattice modes.[281]

The interpretation of the complex Raman spectrum of lithiated anatase requires the knowledge of Li positions. The NMR[285] and quasi-elastic neutron scattering data[273] suggest that the Li ions occupy several positions within the octahedral interstices and that dynamic hopping between them occurs. Neutron scattering data[273] were interpreted with triply split Li positions, namely Li1, Li2, and Li3, one of which (Li2) was found considerably displaced from the center of the interstitial site with the shortest Li−O$_{ax}$ distance of 1.67 Å (Table 8).

Lattice dynamics simulations were performed in order to determine the frequency region of vibrations of Li atoms within the TiO_2 host lattice.[281] Within these simulations, the potential model of the TiO_2 lattice[275] was supplemented by the Li−O, Li−Ti, and Li−Li potentials. Taking into account the variety of possible Li atom positions, the Li−O force
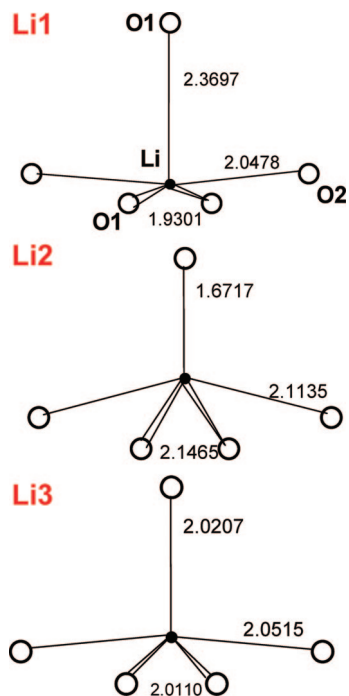
Figure 50. Multiple Li environments in LT-$Li_{0.5}TiO_2$, with the different Li−O bond lengths indicated (in Å). Reprinted with permission from ref 281. Copyright 2004 American Institute of Physics.

Figure 51. Simulated Raman spectrum of TiO_2 anatase and lithium titanate with Li atoms in the Li2 position (b), in the Li3 position (c), and in the Li1 position (d) in comparison with the experimental Raman spectra of anatase (e) and $Li_{0.5}TiO_2$ (f). The Li modes are labeled by bold letters in parts b−d. The TiO_2 lattice modes are labeled in italic in parts a and d. Assignment of the observed spectral features induced by lithium intercalation is shown by dotted lines. Reprinted with permission from ref 281. Copyright 2004 American Institute of Physics.

constant K was represented as a function of Li−O distance R. The dependence $K(R)$ was retrieved from the available references on the Li−O force constant values in different molecules and crystals[286] and justified by the quantum mechanical 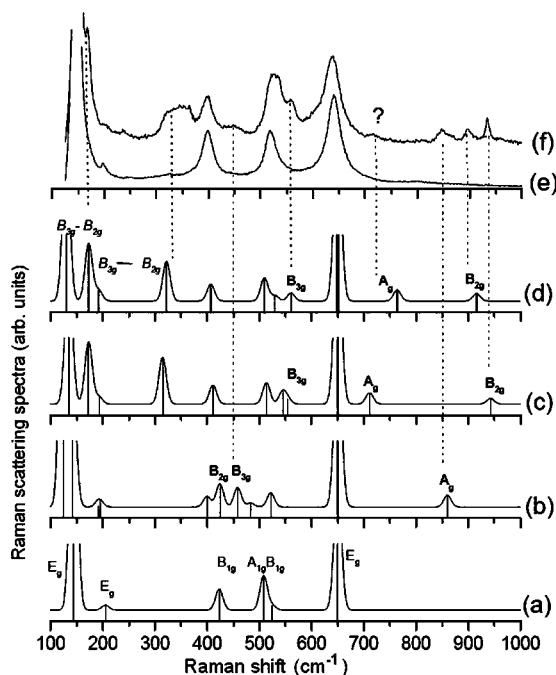simulations.[281] Spectral calculations have been carried out for each Li position, with R(Li−O) values shown in Figure 50. Taking into account the Li−O stretching modes along each of the three orientations, 12 Raman active modes are expected for each of the three Li positions in lithiated titanate $Li_{0.5}TiO_2$:

$$\Gamma_{Raman}(LT) = (3A_g + 3B_{2g} + 3B_{3g})_{lattice} + (A_g + B_{2g} + B_{3g})_{Li}$$

This leads to a complex pattern of simulated Raman spectra which enabled the assignment of all the experimental observed features (Figure 51).

The Raman spectrum and X-ray diffraction patterns of the reoxidized material (Figure 52) are typical of anatase, which indicates the recovery of the tetragonal framework upon oxidation. However, some extra-Raman bands are still observed in the high wavenumber region. This result suggests the presence of strong Li−O bonds which are not broken in the course of the reoxidation process and which are probably responsible for the partial loss of rechargeability of the material evidenced in Figure 48.

In conclusion, Raman experimental data[280] on the lithiated TiO_2 anatase system, supported by lattice dynamics simulation,[281] allowed access to the following straightforward information: (i) Li ions in the lithiated titanate phase have multiple positions in the octahedral interstices of this orthorhombic structure. The multiplicity of possible Li positions manifests itself in the Raman scattering spectra as splitting of the bands originating from Li atom oscillations along different orientations. This leads to the occurrence of multiple Raman bands originated from the Li atoms vibra-

Figure 52. Raman spectra of a Li_xTiO_2 electrode, $x = 0$ (TiO_2), $x = 0.5$ (lithiated titanate phase), and a reoxidized electrode $Li_{0.04}TiO_2$. Excitation with 514.5 nm radiation. The X-ray diffraction pattern of $Li_{0.04}TiO_2$ is shown in the inset. Reprinted with permission from ref 280. Copyright 2004 Wiley.

tions, covering a wide wavenumber range from 450 up to 950 cm^{-1}. Simulated spectra show six Li-bands lying above 450 cm^{-1} and six lattice modes below 650 cm^{-1}. (ii) Some Li interactions take place with the TiO_2 lattice, with this perturbation leading to the splitting of the low frequency lattice modes. (iii) Particular Li positions with rather short Li−O distances were found to give rise to high wavenumber features above 800 cm^{-1}. (vi) Partial electrochemical rechargeability could be explained by the existence of several modes in the high frequency range observed for the charged electrode material and assigned to rather strong Li−O bonds which are not broken in the course of the reoxidation.
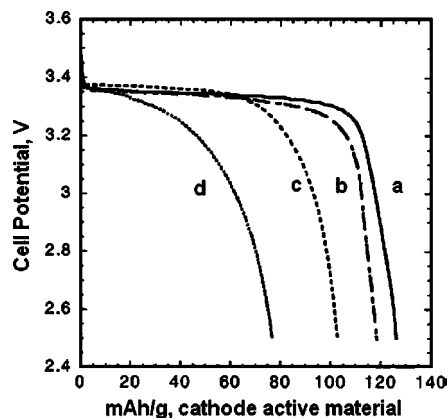
Figure 53. Discharges of Li/1 M LiPF$_6$, EC-DMC/LiFePO$_4$ cells at 0.055 mA/cm^2, showing the carbon coating improvement achieved by incorporating small amounts of a polyaromatic additive during the sol−gel synthesis. (a) Sol gel synthesis with additive, 1.15% total carbon; (b) solid state synthesis from iron acetate, 1.5% carbon; (c) sol gel synthesis with no additive, 0.69% total carbon; (d) sol gel synthesis with no additive, 0.4% total carbon. Reprinted with permission from ref 103. Copyright 2003 The Electrochemical Society.

5. Phospho-olivine LiFePO$_4$ Compound

Over the past few years, phosphate-based materials LiMPO$_4$ (M = Fe, Mn, Co, or Ni) isostructural with olivine have generated considerable interest as a new class of cathodes for lithium ion rechargeable batteries.[287−290] Indeed, in contrast to Li$_x$CoO$_2$ materials, which decompose at elevated temperature, leading to oxygen evolution, LiMPO$_4$ compounds have a highly stable three-dimensional framework due to strong P−O covalent bonds in (PO$_4$)$^{3-}$ polyanion, which prohibits the liberation of oxygen.[287] These characteristics provide an excellent safety and a high stability of the battery under operation.

Much attention has been focused on the low cost and low toxicity LiFePO$_4$ compound because of its attractive theoretical capacity (170 (mA h)/g), based on the two-phase reaction occurring at a 3.4 V vs Li$^+$/Li working potential:[287−290]

$$LiFePO_4 \rightleftarrows FePO_4 + e^- + Li^+$$

Its excellent stability during normal cycling and storage conditions make this material particularly attractive for large scale applications such as hybrid vehicles (HEVs) and electric vehicles (EVs). However, the major drawbacks are the low capacities achieved at even moderate discharge and the poor rate capability, associated with limited electronic and/or ionic conductivity. To address these issues, researchers have optimized the synthesis techniques to minimize particle size, which proved successful in achieving long-term cyclability of nanosized LiFePO$_4$,[291] or have incorporated additives to increase conductivity. The latter approach includes coating olivine particles with carbon by incorporating an organic or polymeric component with the precursors before firing,[103,292] adding metal particles to the mix,[293] or solid−solution doping[294] by metals having higher valence than Li$^+$. All have met success in improving performance. An example of optimization is illustrated in Figure 53, where the quality of the carbon coating, achieved by additive incorporation, accounts mainly for the performance variation.

There have been several investigations into the structure of LiMPO$_4$ compounds. The majority have used Mössbauer spectroscopy and X-ray absorption spectroscopy to focus on
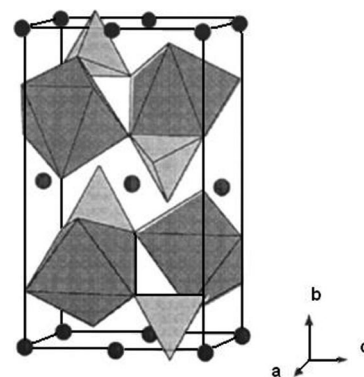
Figure 54. Schematic representation of the polyhedral structure of LiFePO$_4$, showing the arrangement of tetrahedral PO$_4$ and octahedral FeO$_6$ entities. Reprinted with permission from ref 287. Copyright 1997 The Electrochemical Society.

the local structure around transition metal ions.[290,295,296] Tucker et al. used ^{7}Li and ^{31}P magic angle spinning nuclear magnetic resonance (MAS NMR) to investigate the environment of the Li and P atoms in some LiMPO$_4$ materials.[297,298] The vibrational features of olivine-type compounds are well documented. Early work by Paques-Ledent and Tarte focused on identifying the atomic contributions of vibrational modes in a series of LiMPO$_4$ olivine compounds.[299,300] Using a computational simulation employing a normal coordinate analysis based on the Wilson's FG matrix method,[301] Paraguassu et al.[302] provided for the first time a complete set of Raman wavenumbers for LiMPO$_4$ (M = Fe, Co, Ni) with their assignments to vibrational motions and symmetry species of the crystal group. Their predicted values are in good agreement with the experimental Raman features reported for single crystals.[303,304]

LiFePO$_4$ is characterized by a true olivine structure (space group D_{2h}^{16} Pnma). The primitive unit cell is centrosymmetric, with four formula units in the cell. There are two types of octahedral sites; the divalent cations Fe^{2+} are randomly located on the largest 4c site with C_s symmetry, the monovalent cations Li$^+$ are located on the smaller 4a site with C_i symmetry. The pentavalent cations P^{5+} are located in "isolated" tetrahedra PO$_4$ in the 4c site with C_s symmetry. They bridge the FeO$_6$ chains to form an interconnected three-dimensional structure (Figure 54). The arrangement of the different coordinated groups was previously provided.[305]

Group theory[303,304] showed that the normal vibrational modes of LiMPO$_4$ are distributed on the irreducible representation of the D_{2h} point group as

$$\Gamma_{vibr} = 11A_g + 7B_{1g} + 11B_{2g} + 7B_{3g} + 10A_u + 14B_{1u} + 10B_{2u} + 14B_{3u}$$

The number of predicted active fundamentals is rather large: 36 for the Raman spectrum, but the number of observed bands is smaller than the number of predicted active fundamentals. It is usual, although not strictly correct, to classify those vibrations into internal and external modes.[300] Internal modes refer to vibrations occurring in the PO$_4$$^{3-}$ tetrahedra and external to pseudorotations and translations of the units. The translations include motions of the center-of-mass PO$_4$$^{3-}$ and M^{2+}. It should be mentioned that this separation is a guide to discussion only, because the vibrations may be coupled. Assignments of the LiMPO$_4$ internal modes are made using the simplified Herzberg's

Table 10. Raman Wavenumbers and Assignments for LiFePO₄

Raman wavenumbers From Ref. 307	Raman wavenumbers From Ref. 302	Assignment	
107	106		
151	147		
161	157	Translations	
199	195	of Fe^{II}, PO_4 and	External modes
226	238	rotations	
245	249		
292			
410			
447	442		
499		$\nu_2(PO_4)$	
513			
572	571		
595	586		
612	628	$\nu_4(PO_4)$	Internal modes essentially
631			
657			
953	949	$\nu_1(PO_4)$	
999	995		
1071	1067	$\nu_3(PO_4)$	
	1079		

notation for the vibrational modes of a free PO_4 tetrahedron.[306] According to this formalism, the free PO_4 group representations decompose into the irreducible representations of the T_d symmetry group as $A_1 + E + F_1 + 3F_2$. Among these, the internal vibrations in terms of symmetry species are $A_1(\nu_1)$ symmetric P−O stretching, $E(\nu_2)$ symmetric O−P−O bond bending, $F_2(\nu_3)$ antisymmetric P−O stretching, and $F_2(\nu_4)$ antisymmetric O−P−O bond bending. The Raman wavenumbers and assignments observed for LiFePO₄ are summarized in Table 10. The Raman spectrum of LiFePO₄ is shown in Figure 55.

Raman spectroscopy was used to follow the chemical delithiation process in Li_xFePO_4 ($0 \leq x \leq 1$).[307] Important

changes in the spectral features were observed in the first delithiation step; they are the presence of new lines with increased intensities upon Li_xFePO_4 delithiation, several band splittings, and frequency shifts (Figure 56). In particular, new Raman bands were observed in the ν_1 and ν_3 stretching region at 911, 962, 1064, 1080, and 1124 cm^{-1}. In spite of a lack of thorough vibrational analysis and symmetry assignments,

Figure 55. Raman spectrum of LiFePO₄ microcrystals. Excitation with 514.5 nm radiation. Reprinted with permission from ref 302. Copyright 2005 Wiley.
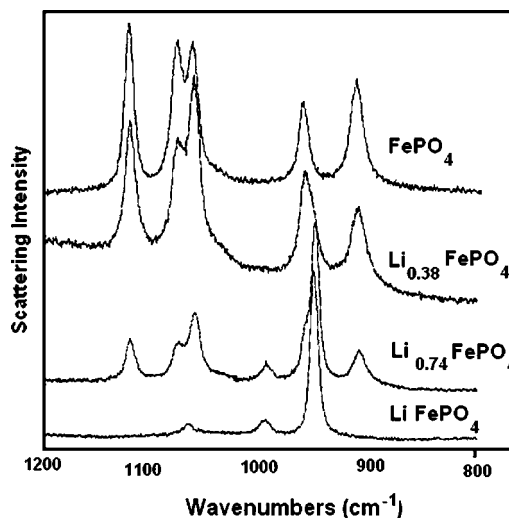
Figure 56. Raman spectra in the 800−1200 cm^{-1} frequency range obtained for chemically delithiated Li_xFePO_4 samples. Excitation with 532 nm radiation. Reprinted with permission from ref 307. Copyright 2004 The Electrochemical Society.
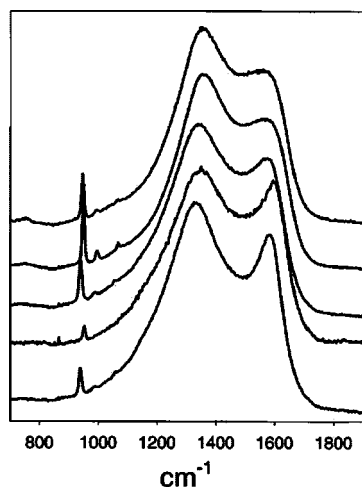
Figure 57. Micro-Raman spectra for different processed $LiFePO_4$ powders. The corresponding electrochemical discharge capacities are (from top to bottom) as follows: 58, 77, 106, 120, 126 (mA h)/g. Excitation with 632 nm radiation. Reprinted with permission from ref 103. Copyright 2003 The Electrochemical Society.
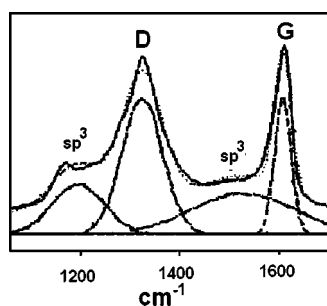
Figure 58. Raman spectrum of the residual carbon of a $LiFePO_4$ powder, with the deconvolution shown below. Excitation with 632 nm radiation. Reprinted with permission from ref 102. Copyright 2007 The Electrochemical Society.

the authors assigned these new features to the $FePO_4$ compound. The Raman band positions were found to be independent of the lithium content, and these results were consistent with the two-phase process usually described.[287]

Conversely, a recent vibrational study reported a contrasting finding which failed to support the well accepted two-crystalline-phase mixture model for lithium extraction.[308] In this work, the main Raman bands observed for delithiated $Li_{0.11}FePO_4$ were found to be in good agreement with those previously reported.[307] However, a deconvolution analysis of the vibrational spectra provided evidence for an additional significant broad-band contribution, in both the Raman and FTIR spectra of $Li_{0.11}FePO_4$. The authors claimed that the two-phase process for transformation of $LiFePO_4$ into $FePO_4$ upon lithium extraction probably includes a pathway where a highly disordered phase is generated.

The carbon coating of the $LiFePO_4$ matrix required for the electrochemical application of this material hinders any bulk Raman data on the Li_xFePO_4 cathode material to be obtained. This is illustrated in Figure 57, where the typical Raman spectrum of a $LiFePO_4$ powder exhibits only a sharp band at 953 cm^{-1} and two weaker bands at 997 and 1098 cm^{-1} assigned to the internal modes of the $(PO_4)^{3-}$ anion.[103] These weak features are explained by the fact that Raman spectroscopy allows examination of phenomena on a carbon surface within a limited penetration depth ($\sim50-100$ nm
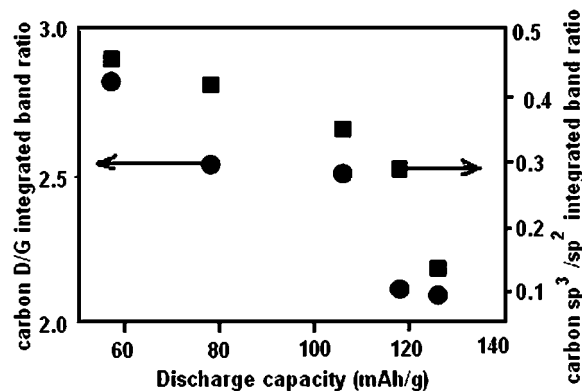
Figure 59. Electrochemical discharge capacity of $LiFePO_4$ electrodes in lithium cells vs structure of residual carbon. Reprinted with permission from ref 103. Copyright 2003 The Electrochemical Society.

with a 514.5 nm green laser beam[34]). In fact, two intense broad bands located at ~1590 and 1350 cm^{-1} are observed, which are assigned to carbon vibrations on the basis of the corresponding features in the spectrum of graphite. The structure at 1590 cm^{-1} mainly corresponds to the G-line associated with the optically allowed E_{2g} zone center mode of crystalline graphite. The structure at 1350 cm^{-1} mainly corresponds to the D-line associated with the disorder-allowed zone-edge mode of graphite. In so far as the structural properties of carbons are known to be strongly related to the shape of the G and D bands,[9−13,38,47,75,95,99−101] Raman spectroscopy in the field of $LiFePO_4$-based cathode materials is a very convenient diagnostic tool to evaluate the quality of the carbon coating on $LiFePO_4$ powders and films.[102,103,309−313] This property is of utmost importance, since these studies indicated that the structure of carbon coating influences greatly the electrochemical performance. As a matter of fact, the shapes of the D and G carbon bands were found to change substantially with the pyrolysis temperature and the nature of the precursor material. This effect is illustrated in Figure 57, where the Raman spectra of the residual carbon are resolved into four components located at ~1190, 1350, 1518, and 1590 cm^{-1} (Figure 58). The bands at 1190 and 1518 cm^{-1} have an uncertain origin but were assigned to short-range vibrations of sp^3-coordinated carbons, as already observed in disordered carbon blacks and diamond-like carbons. Several authors[102,103,309−313] proposed a relationship between the electrochemical capacity and the integrated Raman intensity ratios of D/G bands and sp^3/sp^2 coordinated carbons. As shown in Figure 59, the lower both ratios, the higher the performance exhibited by the $LiFePO_4$ composite electrode. This trend was interpreted in terms of the increasing amount of larger graphene clusters in the very disordered carbon structure and, consequently, an improved electronic conductivity of the carbon deposit.

6. General Conclusion

The application of Li batteries is becoming more prevalent, and demand for the next generation of energy storage for transportation and renewable energy is becoming very high. Through the examples developed in this review, we expect to have provided background and context for applying a powerful analytical tool to further understand battery materials, making advances more likely.

We hope to have convinced the reader of the considerable interest there is in using Raman spectroscopy for better understanding of the relationships between the structure and electrochemistry of electrode materials for lithium batteries. Indeed, the research reviewed in this work clearly demonstrates that it is now possible to obtain a wealth of structural information from the Raman study of various Li intercalated host lattices, from carbon to transition metal oxides and phosphates.

The beneficial aspects of Raman microspectrometry within the field of rechargeable Li batteries and Li ion batteries highlighted in this review are the following:

1. Most of the electrode materials, including carbonaceous compounds, transition metal oxides, and phospho-olivines, are Raman active compounds.

2. From an experimental point of view, Raman spectroscopy is a nondestructive and noninvasive analysis technique under appropriate experimental conditions and does not require any specific conditioning of the sample, which makes its use possible under various environments.

3. Over the past few years, several groups have demonstrated the application of Raman spectroscopy as a powerful *in situ* vibrational probe of electrode materials for Li-batteries.

4. The ability to spatially and temporally explore working lithium batteries has also been confirmed in several works, which might provide another opportunity for researchers to experimentally verify theoretical models used to simulate the movement of Li^+ ions inside batteries.

5. Raman spectroscopy constitutes a very pertinent local tool to enrich the knowledge of the structure of Li intercalation compounds at the scale of interatomic bonds by providing information regarding local disorder, changes in bond lengths, bond angles, coordination, Li dynamics, metal oxidation state, and cation ordering. For instance, several authors have shown that, in the case of carbon, Li_xTiO_2 anatase and $Li_xV_2O_5$ systems, Raman spectroscopy has allowed access to a dynamic picture of the structural changes induced by the electrochemical reaction as a function of various parameters such as Li content, grain size, electrode morphology, or temperature. In other respects, it has also been possible to answer specific electrochemical questions, such as (i) the loss of electrochemical reversibility for Li_xTiO_2 related to the existence of strong Li−O interactions and (ii) the large irreversible capacity of carbon-based electrodes due to a solvent/Li^+ cointercalation leading to graphite exfoliation. For the $Li_xV_2O_5$ system, Raman investigations revealed that the structural response was strongly influenced by the electrode morphology (bulk/thin film) and the nanosize effect. In the case of $LiFePO_4$, the electrochemical performance of the carbon coated cathode has been found to be strongly related to the amount of graphene clusters evaluated from the Raman analysis of the carbon bands.

6. New and pertinent data allowing the identification of the local processes that contribute to the mechanism of Li-battery degradation on cycling or aging have been recently obtained from the great possibilities offered by the confocal Raman imaging technique. Through comparison of peak positions and peak intensities, quantitative and qualitative information concerning the composition of electrode materials can be extracted, such as the spatial distribution of the different electrode components at the surface of the electrode, especially useful for composite electrodes, or the repartition of the local mechanical stresses induced by the electrochemical reaction. For instance, the Raman mapping technique allowed in several cases demonstration that the microscopic information can be directly linked to the macroscopic behavior. Indeed, through access to Raman images showing a marked change in the material's structure as well as its surface composition and distribution after prolonged charge/discharge cycling and/or storage, the searchers get a better understanding of the nature of the processes that affect the electrochemical performance of the electrode and the whole battery.

The ultimate step for a significantly improved and wider application of Raman microspectrometry will consist in systematically combining a rigorous experimental approach with appropriate lattice dynamics simulations. This is the price to benefit from well founded fingerprints for the various lithiated host lattices involved in the electrochemical reactions. Of course, this requires challenging the scientific community for developing reliable theoretical analysis, allowing a comprehensive view of the local structure and Li-induced distortions and then a relevant interpretation of Raman bands. This should make the Raman spectroscopy more efficient, in terms of both analytical and mechanistic analysis, and it prompts the interest of this technique for many researchers implicated in materials science applied to the field of energy storage.

7. Acknowledgments

8. References

(1) Delhaye, M.; Dhamelincourt, P. *J. Raman Spectrosc.* **1975**, *87*, 33.
(2) Delhaye, M.; Bridoux, M.; Wallart, F. *J. Mol. Struct.* **1982**, *79*, 51.
(3) Edward, L. L.; Wachs, I. E. *J. Phys. Chem.* **2007**, *C 11*, 14410.
(4) Loridant, S.; Abello, L.; Siebert, E.; Lucazeau, G. *Solid State Ionics* **1995**, *78*, 249.
(5) Arutyunyan, N. R.; Obraztsova, E. D.; Silly, M.; Jaffrennou, P.; Attal-Tretout, B.; Loiseau, A.; Chuvilin, A. L. *Phys. Status Solidi* **2006**, *B 243*, 3316.
(6) Veirs, D. K.; Ager, J. W.; Loucks, E. T.; Rosenblatt, G. M. *Appl. Opt.* **1990**, *29*, 4969.
(7) Ferraro, J. R.; Maroni, V. A. *Appl. Spectrosc.* **1990**, *44*, 351.
(8) Burns, G.; Dacol, F. H.; Feild, C.; Holtzberg, F. *Solid State Commun.* **1991**, *77*, 367.
(9) Lespade, P.; Marchand, A.; Couzi, M.; Cruege, F. *Carbon* **1984**, *22*, 375.
(10) Knight, D. S.; White, W. B. *J. Mater. Res.* **1989**, *4*, 385.
(11) Ghodbane, S.; Deneuville, A.; Tromson, D.; Bergonzo, P.; Bustarret, E.; Ballutaud, D. *Phys. Status Solidi* **2006**, *A203*, 2397.
(12) Haouni, A.; Mermoux, M.; Marcus, B.; Abello, L.; Lucazeau, G. *Diamond Relat. Mater.* **1999**, *8*, 657.
(13) Ramamurti, R.; Shanov, V.; Singh, R. N.; Mamedov, S.; Boolchand, P. *J. Vac. Sci. Technol. A* **2006**, *24* (2), 179.
(14) Huang, Y.; Yu, P.; Charasse, M. N.; Lo, Y.; Wang, S. *Appl. Phys. Lett.* **1987**, *51*, 192.
(15) Nakashima, S.; Yugami, H.; Fujii, A.; Hangyo, M.; Yamanaka, H. *J. Appl. Phys.* **1988**, *64*, 3067.
(16) Yoshikawa, M.; Ishida, H.; Ishitani, A.; Koisumi, S.; Inuzuka, T. *Appl. Phys. Lett.* **1991**, *58*, 1387.
(17) Vandenabeele, P.; Edwards, H. G. M.; Moens, L. *Chem. Rev.* **2007**, *107* (3), 675.
(18) Coupry, C.; Brissaud, D. In *Raman Microscopy, Developments and Applications*; Turrel, G., Corset, J., Eds.; Elsevier Academic Press: 1996; pp 421−453.
(19) Clarke, R. J. H. *C. R. Chim.* **2002**, *5* (1), 7.
(20) Frost, R. L. *Spectrochim. Acta* **2003**, *A59*, 1195.

(21) Bellot-Gurlet, L.; Le Bourdonnec, F. X.; Poupeau, G.; Dubernet, S. *J. Raman Spectrosc.* **2004**, *35*, 671.

(22) Reiche, I.; Pages-Camagna, S.; Lambacher, L. *J. Raman Spectrosc.* **2004**, *35*, 719.

(23) Whitthingham, M. S. *Chem. Rev.* **2004**, *104*, 4271.

(24) Turrell, G. In *Raman Microscopy, Developments and Applications*; Turrell, G.; Corset, J. Elsevier Academic Press: 1996; pp 1−25.

(25) Cotton, F. A. *Chemical Applications of Group Theory*; Wiley Interscience: New York, NY, 1963.

(26) Delhaye, M.; Barbillat, J.; Aubard, J.; Bridoux, M.; Da Silva, E. In *Raman Microscopy, Developments and Applications*; Turrel, G., Corset, J., Eds.; Elsevier Academic Press: 1996; pp 51−173.

(27) Minsky, M. *Scanning* **1988**, *10*, 128.

(28) Wilson, T. *Confocal Microscopy*; Academic Press: London, 1990.

(29) Dhamelincourt, P.; Barbillat, J.; Delhaye, M. *Spectrosc. Eur.* **1993**, *5*, 16.

(30) Turrel, G.; Delhaye, M.; Dhamelincourt, P. In *Raman Microscopy, Developments and Applications*; Turrel, G., Corset, J., Eds.; Elsevier Academic Press: 1996; pp 27−49.

(31) Everall, N. *Spectroscopy* **2004**, *19*, 22.

(32) Everall, N. *Appl. Spectrosc.* **2000**, *54*, 1515.

(33) Everall, N. *Appl. Spectrosc.* **2000**, *54*, 773.

(34) Solin, S. A. In *Graphite Intercalation Compounds*; Zabel, I. H., Solin, S. A., Eds.; Springer-Verlag: Berlin, 1990; p 165.

(35) Itoh, T.; Sato, H.; Nishina, T.; Matue, T.; Uchida, I. *J. Power Sources* **1997**, *68*, 333.

(36) Huang, W.; Frech, R. *J. Power Sources* **1999**, *82*, 616.

(37) Zhang, X.; Frech, R. *J. Electrochem. Soc.* **1998**, *145*, 847.

(38) Irish, D. E.; Deng, Z.; Odziemkowski, M. *J. Power Sources* **1995**, *54*, 28.

(39) Inaba, M.; Yoshida, H.; Ogumi, Z.; Abe, T.; Mizutani, Y.; Asano, M. *J. Electrochem. Soc.* **1995**, *142*, 20.

(40) Inaba, M.; Yoshida, H.; Ogumi, Z. *J. Electrochem. Soc.* **1996**, *143*, 2572.

(41) Huang, W.; Frech, R. *J. Electrochem. Soc.* **1998**, *145*, 765.

(42) Novak, P.; Joho, F.; Imhof, R.; Panitz, J.-C.; Haas, O. *J. Power Sources* **1999**, *81−82*, 212.

(43) Panitz, J. C.; Joho, F.; Novak, P. *Appl. Spectrosc.* **1999**, *53*, 1188.

(44) Rey, I.; Bruneel, J. L.; Grondin, J.; Servant, L.; Lassègues, J. C. *J. Electrochem. Soc.* **1998**, *145*, 3034.

(45) Rey, I.; Lassègues, J. C.; Baudry, P.; Majastre, H. *Electrochim. Acta* **1998**, *43*, 1539.

(46) Novak, P.; Panitz, J.-C.; Joho, F.; Lanz, M.; Imhof, R.; Coluccia, M. *J. Power Sources* **2000**, *90*, 52.

(47) Panitz, J. C.; Novak, P. *J. Power Sources* **2001**, *97−98*, 174.

(48) Panitz, J. C.; Novak, P.; Haas, O. *Appl. Spectrosc.* **2001**, *55*, 1131.

(49) Kerlau, M.; Marcinek, M.; Kostecki, R. *J. Power Sources* **2007**, *174*, 1046.

(50) Kerlau, M.; Marcinek, M.; Srinivasan, V.; Kostecki, R. M. *Electrochim. Acta* **2007**, *52*, 5422.

(51) Kostecki, R.; Lei, J.; McLarnon, F.; Shim, J.; Striebel, K. *J. Electrochem. Soc.* **2006**, *153*, A669.

(52) Kostecki, R.; McLarnon, F. *Electrochem. Solid-State Lett.* **2004**, *7*, A380.

(53) Striebel, K. A.; Shim, J.; Cairns, E. J.; Kostecki, R.; Lee, Y.-J.; Reimer, J.; Richardson, T. J.; Ross, P. N.; Song, X.; Zhuang, G. V. *J. Electrochem. Soc.* **2004**, *151*, A857.

(54) Kostecki, R.; McLarnon, F. *Electrochem. Solid-State Lett.* **2002**, *5*, A164.

(55) Kostecki, R.; McLarnon, F. *J. Power Sources* **2003**, *119−121*, 550.

(56) Hardwick, L. J.; Marcinek, M.; Beer, L.; Kerr, J. B.; Kostecki, R. *J. Electrochem. Soc.* **2008**, *155*, A442.

(57) (a) Totir, D. A.; Scherson, D. A. *Electrochem. Solid-State Lett.* **2000**, *3*, 263. (b) Luo, Y.; Cai, W.-B.; Scherson, D. A. *J. Electrochem. Soc.* **2002**, *149*, A1100.

(58) Luo, Y.; Cai, W.-B.; Scherson, D. A. *Electrochem. Solid-State Lett.* **2001**, *4*, A101.

(59) Dokko, K.; Shi, Q.; Stefan, I.-C.; Scherson, D.-A. *J. Phys. Chem B* **2003**, *107*, 12549.

(60) Luo, Y.; Cai, W. B.; Xing, X. K.; Scherson, D. A. *Electrochem. Solid-State Lett.* **2004**, *7*, 1.

(61) Lei, J.; McLarnon, F.; Kostecki, R. *J. Phys. Chem. B* **2005**, *109*, 952.

(62) Migge, S.; Sandmann, G.; Rahner, D.; Dietz, H.; Plieth, W. *J. Solid State Electrochem.* **2005**, *9*, 132.

(63) Burba, M.; Frech, R. *Appl. Spectrosc.* **2006**, *60*, 490.

(64) Peled, E. *J. Electrochem. Soc.* **1979**, *126*, 2047.

(65) Deng, Z.; Irish, D. E. *Langmuir* **1994**, *10*, 586.

(66) Hardwick, L. J.; Holzapfel, M.; Wokaun, A.; Novak, P. *J. Raman Spectrosc.* **2007**, *38*, 110.

(67) Hyodo, S. A.; Okabayashi, K. *Electrochim. Acta* **1989**, *34*, 1557.

(68) Howlett, P. C.; MacFarlane, D. R.; Hollenkamp, A. F. *J. Power Sources* **2003**, *114*, 277.

(69) Aurbach, D. *J. Power Sources* **2000**, *89*, 206.

(70) Naudin, C.; Bruneel, J. L.; Chami, M.; Desbat, B.; Grondin, J.; Lassègues, J. C.; Servant, L. *J. Power Sources* **2003**, *124*, 518.

(71) Li, H.; Mo, Y.; Pei, N.; Xu, X.; Huang, X.; Chen, L. *J. Phys. Chem. B* **2000**, *104*, 8477.

(72) Li, G.; Li, H.; Mo, Y.; Chen, L.; Huang, X. *J. Power Sources* **2002**, *104*, 190.

(73) Wakihara, M. *Mater. Sci. Eng.* **2001**, *R33*, 109.

(74) Dahn, J. R.; Sleigh, A. K.; Shi, H.; Reimers, J. N.; Zhong, Q.; Way, B. M. *Electrochim. Acta* **1993**, *38*, 1179.

(75) Tuinstra, F.; Koenig, J. L. *J. Chem. Phys.* **1976**, *53*, 1126.

(76) Mernagh, T. P.; Cooney, R. P.; Johnson, R. A. *Carbon* **1984**, *22*, 39.

(77) Ramsteiner, M.; Wagner, J. *Appl. Phys. Lett.* **1987**, *51*, 1355.

(78) Wang, Y.; Aolsmeyer, D. C.; McCreery, R. L. *Chem. Mater.* **1990**, *2*, 557.

(79) Matthews, M. J.; Pimenta, M. A.; Dresselhaus, G.; Dresselhaus, M. S.; Endo, M. *Phys. Rev. B* **1999**, *59*, 6585.

(80) Kastner, J.; Pichler, T.; Kuzmany, H.; Curran, S.; Blau, W.; Weldon, D. N.; Dlamesiere, M.; Draper, S.; Zandbergen, H. *Chem. Phys. Lett.* **1994**, *221*, 53.

(81) Pócsik, I.; Hundhausen, M.; Koós, M.; Ley, L. *J. Non-Cryst. Solids* **1998**, *227−230*, 1083.

(82) Tan, P.; Dimovski, S.; Gogotsi, Y. *Philos. Trans. R. Soc. A* **2004**, *362*, 2289.

(83) Barros, E. B.; Demir, N. S.; Souza Filho, A. G.; Mendes Filho, J.; Jorio, A.; Dresselhaus, G.; Dresselhaus, M. S. *Phys. Rev. B* **2005**, *71*, 165422.

(84) Vidano, R. P.; Fishbach, D. B.; Willis, L. J.; Loehr, T. M. *Solid State Commun.* **1981**, *39*, 341.

(85) Baranov, A. V.; Bekhterev, A. N.; Bobovich, Ya. S.; Petrov, V. I. *Opt. Spectrosk.* **1987**, *62*, 612.

(86) Thomsen, C.; Reich, S. *Phys. Rev. Lett.* **2000**, *85*, 5214.

(87) Sato, K; Saito, R.; Oyama, Y.; Jiang, J.; Cançado, L. G.; Pimenta, M. A.; Jorio, A.; Samsonidze, Ge. G.; Dresselhaus, G.; Dresselhaus, M. S. *Chem. Phys. Lett.* **2006**, *427*, 117.

(88) Dresselhaus, M. S.; Dresselhaus, G.; Eklund, P. J.; Chung, D. D. *Mater. Sci. Eng.* **1977**, *31*, 141.

(89) Underhill, C.; Leung, S. Y.; Dresselhaus, G.; Dresselhaus, M. S. *Solid State Commun.* **1979**, *29*, 769.

(90) Dresselhaus, M. S.; Dresselhaus, G. *Adv. Phys.* **1981**, *30*, 139.

(91) Abe, T.; Inaba, M.; Ogumi, Z.; Yokota, Y.; Mizutani, Y. *Phys. Rev. B* **2000**, *61*, 11344.

(92) Chan, C. T.; Ho, K. M.; Kamitakahara, W. A. *Phys. Rev. B* **1987**, *36*, 3499.

(93) Doll, G. L.; Ecklund, P.; Fischer, J. E. *Phys. Rev. B* **1987**, *36*, 4940.

(94) Maurin, G.; Bousquet, Ch.; Henn, F.; Bernier, P.; Almairac, R.; Simon, B. *Solid State Ionics* **2000**, *136*, 1295.

(95) Spahr, M. E.; Paladino, T.; Wilhelm, H.; Würsig, A.; Goers, D.; Buqa, H.; Holzapfel, M.; Novak, P. *J. Electrochem. Soc.* **2004**, *151*, 1383.

(96) Hardwick, L. J.; Buqa, H.; Novak, P. *Solid State Ionics* **2006**, *177*, 2801.

(97) Hardwick, L. J.; Ruch, P. W.; Hahn, M.; Scheifele, W.; Kötz, R.; Novak, P. *J. Phys. Chem. Solids* **2008**, *69*, 1232.

(98) Hardwick, L. J.; Buqa, H.; Holzapfel, M.; Scheifele, W.; Krumeich, F.; Novak, P. *Electrochim. Acta* **2007**, *52*, 4884.

(99) Goers, D.; Buqua, H.; Hardwick, L.; Würsig, A.; Novak, P. *Ionics* **2003**, *9*, 258.

(100) Nakajima, T. *J. Fluorine Chem.* **2007**, *128*, 277.

(101) Reynier, Y.; Yazami, R.; Fultz, B.; Barsukov, I. *J. Power Sources* **2007**, *165*, 552.

(102) Wilcox, J. D.; Doeff, M. M.; Marcinek, M.; Kostecki, R. *J. Electrochem. Soc.* **2007**, *154A*, 389.

(103) Doeff, M. M.; Hu, Y.; McLarnon, F.; Kostecki, R. *Electrochem. Solid-State Lett.* **2003**, *6A*, 207.

(104) Striebel, K.; Shim, J.; Sierra, A.; Yang, H.; Song, X.; Kostecki, R.; McCarthy, K. *J. Power Sources* **2005**, *146*, 33.

(105) Kostecki, R.; Tran, T.; Song, X.; Kinoshita, K.; McLarnon, F. *J. Electrochem. Soc.* **1997**, *144*, 3111.

(106) Fong, R.; Von Sacken, U.; Dahn, J. R. *J. Electrochem. Soc.* **1990**, *137*, 2009.

(107) Mizushima, K.; Jones, P. C.; Wiseman, P. J.; Goodenough, J. B. *Mater. Res. Bull.* **1980**, *15*, 783.

(108) Ohzuku, T.; Ueda, A. *J. Electrochem. Soc.* **1994**, *141*, 2972.

(109) Inaba, M.; Todzuka, Y.; Yoshida, H.; Grincourt, Y.; Tasaka, A.; Tomida, Y.; Ogumi, Z. *Chem. Lett.* **1995**, 889.

(110) Inaba, M.; Iriyama, Y.; Ogumi, Z.; Todsuka, Y.; Tasaka, A. *J. Raman Spectrosc.* **1997**, *28*, 613.

(111) Reimers, J. N.; Dahn, J. R. *J. Electrochem. Soc.* **1992**, *139*, 2091.

(112) Amatucci, G. G.; Tarascon, J. M.; Klein, L. C. *J. Electrochem. Soc.* **1996**, *143*, 1114.

(113) Itoh, T.; Anzue, N.; Mohamedi, M.; Hisamitsu, Y.; Umeda, M.; Uchida, I. *Electrochem. Commun.* **2000**, *2*, 743.

(114) Kim, Y. J; Lee, E. K.; Kim, H.; Cho, J.; Cho, Y. W.; Park, B.; Oh, S. M.; Yoon, J. K. *J. Electrochem. Soc.* **2004**, *151*, 1063.

(115) Kang, S. G.; Kang, S. Y.; Ryu, K. S.; Chang, S. H. *Solid State Ionics* **1999**, *120*, 155.

(116) Santiago, E. I.; Andrade, A. V. C.; Paiva-Santos, C. O.; Bulhoes, L. O. S. *Solid State Ionics* **2003**, *158*, 91.

(117) Ra, D. I.; Han, K. S. *J. Power Sources* **2006**, *163*, 284.

(118) Julien, C.; Camacho-Lopez, M. A.; Escobar-Alarcon, L.; Haro-Poniatowski, E. *Mater. Chem. Phys.* **2001**, *68*, 210.

(119) Tang, S. B.; Lai, M. O.; Lu, L. *J. Alloys Compd.* **2006**, *424*, 342.

(120) Park, H. Y.; Lee, S. R.; Lee, Y. J.; Cho, B. W.; Cho, W. I. *Mater. Chem. Phys.* **2005**, *93*, 70.

(121) Jeon, S. W.; Lim, J. K.; Lim, S. H.; Lee, S. M. *Electrochim. Acta* **2005**, *51*, 268.

(122) Pracharova, J.; Pridal, J.; Bludska, J.; Jakubec, I.; Vorlicek, V.; Malkova, Z.; Dikonimos Makris, Th.; Giorgi, R.; Jastrabik, L. *J. Power Sources* **2002**, *108*, 204.

(123) Liao, C. L.; Wu, M. T.; Chen, J. H.; Leu, I. C.; Fung, K. Z. *J. Alloys Compd.* **2006**, *414*, 302.

(124) Lee, T.; Cho, K.; Oh, J.; Shin, D. *J. Power Sources* **2007**, *174*, 394.

(125) Koike, S.; Tatsumi, K. *J. Power Sources* **2007**, *174*, 976.

(126) Kushida, K.; Kuriyama, K. *J. Cryst. Growth* **2002**, *237–239*, 612.

(127) Lee, J. H.; Han, K. S.; Lee, B. J.; Seo, S. I.; Yoshimura, M. *Electrochim. Acta* **2004**, *50*, 467.

(128) Rossen, E.; Reimers, J. N.; Dahn, J. R. *Solid State Ionics* **1993**, *62*, 53.

(129) Gummow, R. J.; Liles, D. C.; Tackeray, M. M.; David, W. I. F. *Mater. Res. Bull.* **1993**, *28*, 1177.

(130) Garcia, B.; Farcy, J.; Pereira-Ramos, J. P.; Baffier, N. *J. Electrochem. Soc.* **1997**, *144*, 1179.

(131) Huang, W.; Frech, R. *Solid State Ionics* **1996**, *86–88*, 395.

(132) Mendoza, L.; Baddour-Hadjean, R.; Cassir, M.; Pereira-Ramos, J. P. *Appl. Surf. Sci.* **2004**, *225*, 356.

(133) Kuk, S. T.; Song, Y. S.; Suh, S. I.; Kim, J. Y.; Kim, K. *J. Mater. Chem.* **2001**, *11*, 630.

(134) Uchida, I.; Sato, H. *J. Electrochem. Soc.* **1995**, *142*, L139.

(135) Goodenough, J. B.; Wickham, D. G.; Croft, W. J. *J. Phys. Chem. Solids* **1958**, *5*, 107.

(136) Delmas, C.; Saadoune, I. *Solid State Ionics* **1992**, *53–56*, 370.

(137) Julien, C. *Solid State Ionics* **2000**, *887*, 136–137.

(138) Rougier, A.; Nazri, G. A.; Julien, C. *Ionics* **1997**, *3*, 170.

(139) Ramana, C. V.; Zaghib, K.; Julien, C. M. *J. Power Sources* **2006**, *159*, 1310.

(140) Shim, J.; Kostecki, R.; Richardson, T.; Song, X.; Striebel, K. A. *J. Power Sources* **2002**, *112*, 222.

(141) Norin, L.; Kostecki, R.; McLarnon, F. *Electrochem. Solid-State Lett.* **2002**, *5*, A67.

(142) Kerlau, M.; Kostecki, R. *J. Electrochem. Soc.* **2006**, *153*, A1644.

(143) Ohzuku, T.; Makimura, Y. *Chem. Lett.* **2001**, 642.

(144) Hwang, B. J.; Tsai, Y. W.; Carlier, D.; Ceder, G. *Chem. Mater.* **2003**, *15*, 3676.

(145) Tran, N.; Croguennec, L.; Jordy, C.; Biensan, P.; Delmas, C. *Solid State Ionics* **2005**, *176*, 1539.

(146) Wang, Z. X.; Sun, Y. C.; Chen, L. Q.; Huang, X. J. *J. Electrochem. Soc.* **2004**, *151*, A914.

(147) Tran, N.; Croguennec, L.; Labrugere, C.; Jordy, C.; Biensan, Ph.; Delmas, C. *J. Electrochem. Soc.* **2006**, *153*, A251.

(148) Saavedra-Arias, J. J.; Karan, N.; Pradhan, D. K.; Kumar, A.; Nieto, S.; Thomas, R.; Katiyar, R. S. *J. Power Sources* **2008**, *138*, 761.

(149) Le Goff, P.; Baffier, N.; Bach, S.; Pereira-Ramos, J. P. *Mater. Res. Bull.* **1996**, *31*, 63.

(150) Thackeray, M. M. *Prog. Solid State Chem.* **1997**, *25*, 1.

(151) McBreen, J. *Electrochim. Acta* **1975**, *20*, 221.

(152) Nardi, J. C. *J. Electrochem. Soc.* **1985**, *132*, 1787.

(153) Ohzuku, T.; Kitagawa, M.; Hirai, T. *J. Electrochem. Soc.* **1989**, *136*, 3169.

(154) Hill, L. I.; Portal, R.; La Salle, A. L.; Verbaere, A.; Guyomard, D. *Electrochem. Solid-State Lett.* **2001**, *4*, 1.

(155) Thackeray, M. M.; De Picciotto, L. A.; De Kock, A.; Johnson, P. J.; Nicholas, V. A.; Andendorf, K. T. *J. Power Sources* **1987**, *21*, 1.

(156) Armstrong, A. R.; Bruce, P. G. *Nature* **1996**, *381*, 499.

(157) Bordet-Le Guenne, L.; Deniard, P.; Biensant, P.; Siret, C.; Brec, R. *J. Mater. Chem.* **2000**, *10*, 2201.

(158) Julien, C. M.; Massot, M.; Poinsignon, C. *Spectrochim. Acta, Part A* **2004**, *60*, 689.

(159) Julien, C. M. *Solid State Ionics* **2006**, *177*, 11.

(160) Strohmeier, B. R.; Hercules, D. M. *J. Phys. Chem.* **1984**, *88*, 4923.

(161) Kapteijn, F.; Van Langeveld, A. D.; Moulijn, J. A.; Andreini, A.; Vuurman, M. A.; Turek, A. M.; Jehng, J.-M.; Wachs, I. E. *J. Catal.* **1994**, *150*, 94.

(162) Gosztola, D.; Weaver, M. J. *J. Electroanal. Chem. Interfacial Electrochem.* **1989**, *271*, 141.

(163) Bernard, M. C.; Hugot-le Goff, A.; Vu, B. Thi; Cordoba de Torresi, S. *J. Electrochem. Soc.* **1993**, *140*, 3065.

(164) Buciuman, F.; Patcas, F.; Craciun, R.; Zahn, D. R. T. *Phys. Chem. Chem. Phys.* **1999**, *1*, 185.

(165) Widjaja, E.; Sampanthar, J. T. *Anal. Chim. Acta* **2007**, *585*, 241.

(166) Paolone, A.; Sacchetti, A.; Corridoni, T.; Postorino, P.; Cantelli, R.; Rousse, G.; Masquelier, C. *Solid State Ionics* **2004**, *170*, 135.

(167) Paolone, A.; Sachetti, A.; Postorino, P.; Cantelli, R. *J. Phys. Chem. B* **2005**, *109*, 7587.

(168) Franger, S.; Bach, S.; Farcy, J.; Pereira-Ramos, J. P.; Baffier, N. *J. Power Sources* **2002**, *109*, 262.

(169) Julien, C.; Massot, M.; Baddour-Hadjean, R.; Franger, S.; Bach, S.; Pereira-Ramos, J. P. *Solid State Ionics* **2003**, *159*, 345.

(170) Franger, S.; Bach, S.; Pereira-Ramos, J. P.; Baffier, N. *J. Electrochem. Soc.* **2000**, *147*, 3226.

(171) Julien, C. M.; Massot, M. *Mater. Sci. Eng. B* **2003**, *97*, 217.

(172) Thackeray, M. M.; Johnson, P.; De Piciotto, L.; Bruce, P. G.; Goodenough, J. B. *Mater. Res. Bull.* **1984**, *19*, 179.

(173) Ohzuku, T.; Kitagawa, M.; Hirai, T. *J. Electrochem. Soc.* **1990**, *137*, 769.

(174) Guyomard, D.; Tarascon, J. M. *J. Electrochem. Soc.* **1992**, *139*, 937.

(175) Yamada, A.; Miura, K.; Hinokuma, K.; Tanaka, M. *J. Electrochem. Soc.* **1995**, *142*, 2149.

(176) Tarte, P. *J. Inorg. Nucl. Chem.* **1967**, *29*, 915.

(177) Tarte, P.; Preudhomme, J. *Spectrochim. Acta* **1970**, *26A*, 747.

(178) Preudhomme, J.; Tarte, P. *Spectrochim. Acta* **1971**, *27A*, 845.

(179) White, W. B.; De Angelis, B. A. *Spectrochim. Acta* **1967**, *23A*, 985.

(180) Richardson, J. T.; Wen, S. J.; Striebel, K. A.; Ross, P. N.; Cairns, E. J. *Mater. Res. Bull.* **1997**, *32*, 609.

(181) Wen, S. J.; Richardson, J. T.; Ma, L.; Striebel, K. A.; Ross, P. N.; Cairns, E. J. *J. Electrochem. Soc.* **1996**, *143*, L136.

(182) Kanoh, H.; Tang, W.; Ooi, K. *Electrochem. Solid-State Lett.* **1998**, *1*, 17.

(183) Ammundsen, B.; Burns, G. R.; Islam, M. S.; Kanoh, H.; Roziere, J. *J. Phys. Chem. B* **1999**, *103*, 5175.

(184) Hwang, S.-J.; Park, D.-H.; Choy, J.-H.; Campet, G. *J. Phys. Chem. B* **2004**, *108*, 12713.

(185) Liu, W.; Kowal, K.; Farrington, G. C. *J. Electrochem. Soc.* **1998**, *145*, 459.

(186) Mukerjee, S.; Thurston, T. R.; Jisrawi, N. M.; Yang, X. Q.; McBreen, J.; Daroux, M. L.; Xing, X. K. *J. Electrochem. Soc.* **1998**, *145*, 466.

(187) Xia, Y.; Yoshio, M. *J. Electrochem. Soc.* **1996**, *143*, 825.

(188) Gao, Y.; Reimers, J. N.; Dahn, J. R. *Phys. Rev.* **1996**, *B54*, 3878.

(189) David, W. I. F.; Thackeray, M. M.; De Picciotto, L. A.; Goodenough, J. B. *J. Solid State Chem.* **1987**, *67*, 316.

(190) Julien, C. M.; Massot, D. *Mater. Sci. Eng. B* **2003**, *100*, 69.

(191) Anzue, N.; Itoh, T.; Mohamedi, M.; Umeda, M.; Uchida, I. *Solid State Ionics* **2003**, *156*, 301.

(192) Shi, Q.; Takahashi, Y.; Akimoto, J.; Stefan, I. C.; Scherson, D. A. *Electrochem. Solid-State Lett.* **2005**, *8*, A521.

(193) Song, D.; Ikuta, H.; Uchida, T.; Wakihara, M. *Solid State Ionics* **1999**, *117*, 151.

(194) Li, G. H.; Ikuta, H.; Uchida, T.; Wakihara, M. *J. Electrochem. Soc.* **1996**, *143*, 178.

(195) Kim, K. W.; Lee, S. W.; Han, K. S.; Chung, H. J.; Woo, S. I. *Electrochim. Acta* **2003**, *48*, 4223.

(196) Strobel, P.; Ibarra-Palos, A.; Anne, M.; Poinsignon, C.; Crisci, A. *Solid State Sci.* **2003**, *5*, 1009.

(197) Wei, Y.; Kim, K.-B.; Chen, G. *Electrochim. Acta* **2006**, *51*, 3365.

(198) Dokko, K.; Mohamedi, M.; Anzue, N.; Itoh, T.; Uchida, I. *J. Mater. Chem.* **2002**, *12*, 3688.

(199) Dokko, K.; Anzue, N.; Mohamedi, M.; Itoh, T.; Uchida, I. *Electrochem. Commun.* **2004**, *6*, 384.

(200) Ramana, C. V.; Massot, M.; Julien, C. M. *Surf. Interface Anal.* **2005**, *37*, 412.

(201) Zhang, F.; Whittingham, M. S. *Electrochem. Solid-State Lett.* **2000**, *3*, 7.

(202) Park, H. S.; Hwang, S. J.; Choy, J. H. *J. Phys. Chem.* **2001**, *B105*, 4860.

(203) Hwang, S. J.; Park, H. S.; Choy, J. H.; Campet, G.; Portier, J.; Kwon, C. W.; Etourneau, J. *Electrochem. Solid-State Lett.* **2001**, *4*, A213.

(204) Doeff, M. M.; Anapolsky, A.; Edman, L.; Richardson, T. J.; De Jonghe, L. C. *J. Electrochem. Soc.* **2001**, *148*, A230.

(205) Saint, J. A.; Doeff, M. M.; Wilcox, J. *Chem. Mater.* **2008**, *20*, 3403.

(206) Saint, J.; Best, A. S.; Hollenkamp, A. F.; Kerr, J.; Shin, J.-H.; Doeff, M. M. *J. Electrochem. Soc.* **2008**, *155*, A127.

(207) Hardwick, L. J.; Saint, J. A.; Lucas, I. T.; Doeff, M. M.; Kostecki, R. *J. Electrochem. Soc.* **2009**, *156*, A120.

(208) Murphy, D. W.; Christian, P. A.; Disalvo, F. J.; Waszczak, J. V. *Inorg. Chem.* **1979**, *18*, 2800.

(209) Whittingham, M. S. *J. Electrochem. Soc.* **1976**, *126*, 315.

(210) Wiesener, K.; Schneider, W.; Ilic, D.; Steger, E.; Hallmeir, K. H.; Brackmann, E. *J. Power Sources* **1978**, *20*, 157.

(211) Delmas, C.; Cognac-Auradou, H.; Cocciantelli, J. M.; Ménétrier, M.; Doumerc, J. P. *Solid State Ionics* **1994**, *69*, 257.

(212) Bates, J. B.; Gruzalski, G. R.; Dudney, N. J.; Luck, C. F.; Xiaohua, Y. *Solid State Ionics* **1994**, *70/71*, 619.

(213) Cocciantelli, J. M.; Doumerc, J. P.; Pouchard, M.; Broussely, M.; Labat, J. *J. Power Sources* **1991**, *34*, 103.

(214) Abello, L.; Husson, E.; Repelin, E.; Lucazeau, G. *Spectrochim. Acta* **1983**, *39A*, 641.

(215) Clauws, P.; Vennik, J. *Phys. Status Solidi* **1980**, *B59*, 469.

(216) Baddour-Hadjean, R.; Pereira-Ramos, J. P.; Navone, C.; Smirnov, M. *Chem. Mater.* **2008**, *20*, 1916.

(217) Dickens, P. G.; French, S. J.; Hight, A. T.; Pye, M. F. *Mater. Res. Bull.* **1979**, *14*, 1295.

(218) Galy, J.; Darriet, J.; Hagenmuller, P. *Rev. Chim. Miner.* **1971**, *8*, 509.

(219) Rozier, P.; Savariault, J. M.; Galy, J.; Marichal, C.; Horschinger, J.; Granger, P. *Eur. J. Solid State Inorg. Chem.* **1996**, *33*, 1.

(220) Galy, J. *J. Solid State Chem.* **1992**, *100*, 229.

(221) Cocciantelli, J. M.; Gravereau, J. M.; Doumerc, J. P.; Pouchard, M.; Hagenmuller, P. *J. Solid State Chem.* **1991**, *93*, 497.

(222) Leger, C.; Bach, S.; Soudan, P.; Pereira-Ramos, J. P. *J. Electrochem. Soc.* **2005**, *152A*, 236.

(223) Delmas, C.; Brethes, S.; Ménétrier, M. *J. Power Sources* **1991**, *34*, 113.

(224) Baddour-Hadjean, R.; Rackelboom, E.; Pereira-Ramos, J. P. *Chem. Mater.* **2006**, *18*, 3548.

(225) Rozier, P.; Savariaut, J. M.; Galy, J. *Solid State Ionics* **1997**, *98*, 133.

(226) Meulenkamp, E. A.; van Klinken, W.; Schlatmann, A. R. *Solid State Ionics* **1999**, *126*, 235.

(227) Prouzet, E.; Cartier, C.; Vilain, F.; Tranchant, A. *J. Chem. Soc., Faraday Trans.* **1996**, *92*, 103.

(228) Hirschinger, J.; Mongrelet, T.; Marichal, C.; Granger, P.; Savariault, J. M.; Déramond, E.; Galy, J. *J. Phys. Chem.* **1993**, *97*, 10301.

(229) Pecquenard, B.; Gourier, D.; Baffier, N. *Solid State Ionics* **1995**, *78*, 287.

(230) Cava, R. J.; Santoro, A.; Murphy, D. W.; Zahurak, S. M.; Fleming, R. M.; Marsh, P.; Roth, R. S. *J. Solid State Chem.* **1986**, *65*, 63.

(231) Savariault, J. M.; Rozier, P. *Physica B* **1997**, *234–236*, 97.

(232) Katzke, H.; Czank, M.; Depmeier, W.; van Smaalen, S. *Philos. Mag.* **1997**, *B75*, 757.

(233) Zhang, X.; Frech, R. *Electrochim. Acta* **1997**, *42*, 475.

(234) Cazzanelli, E.; Mariotto, G.; Passerini, S.; Decker, F. *Solid State Ionics* **1994**, *70–71*, 412.

(235) Ramana, C. V.; Smith, R. J.; Hussain, O. M.; Massot, M.; Julien, C. M. *Surf. Interface Anal.* **2005**, *37*, 406.

(236) Julien, C.; Ivanov, I.; Gorenstein, A. *Mater. Sci. Eng.* **1995**, *B33*, 168.

(237) Baddour-Hadjean, R.; Golabkan, V.; Pereira-Ramos, J. P.; Mantoux, A.; Lincot, D. *J. Raman Spectrosc.* **2002**, *33*, 631.

(238) McGraw, J. M.; Perkins, J. D.; Zhang, J. G.; Liu, P.; Parilla, P. A.; Turner, J.; Schulz, D. L.; Curtis, C. J.; Ginley, D. S. *Solid State Ionics* **1998**, *113–115*, 407.

(239) Baddour-Hadjean, R.; Navone, C.; Pereira-Ramos, J. P. *Electrochim. Acta* **2009**, *54*, 6674.

(240) Satto, C.; Sciau, P.; Dooryhee, P. E.; Galy, J.; Millet, P. *J. Solid State Chem.* **1999**, *146*, 103.

(241) Popovic, Z. V.; Gajic, R.; Konstantinovic, M. J.; Provoost, R.; Moshchalkov, V. V.; Vasil'ev, A. N.; Isobe, M.; Ueda, Y. *Phys. Rev.* **2000**, *B61*, 11454.

(242) Talledo, A.; Granqvist, C. G. *J. Appl. Phys.* **1995**, *77*, 4655.

(243) Scarminio, J.; Talledo, A.; Andersson, A.; Passerini, S.; Decker, F. *Electrochim. Acta* **1993**, *38*, 1637.

(244) Ptitsyn, M. V.; Tikhonov, K. I.; Rotinyan, A. L. *Sov. Electrochem.* **1981**, *17*, 1297.

(245) Andrukaitis, E.; Jacobs, P. W. M.; Lorimer, J. W. *Solid State Ionics* **1988**, *27*, 19.

(246) Meulenkamp, E. A. *J. Electrochem. Soc.* **1998**, *145*, 2759.

(247) Vivier, V.; Farcy, J.; Pereira-Ramos, J. P. *Electrochim. Acta* **1998**, *44*, 831.

(248) Navone, C.; Pereira-Ramos, J. P.; Baddour-Hadjean, R.; Salot, R. *J. Electrochem. Soc.* **2006**, *153A*, 2287.

(249) Navone, C.; Baddour-Hadjean, R.; Pereira-Ramos, J. P.; Salot, R. *J. Electrochem. Soc.* **2005**, *152A*, 1790.

(250) Navone, C.; Baddour-Hadjean, R.; Pereira-Ramos, J. P.; Salot, R. *Electrochim. Acta* **2008**, *53*, 3329.

(251) Navone, C.; Pereira-Ramos, J. P.; Baddour-Hadjean, R.; Salot, R. *J. Power Sources* **2005**, *146*, 327.

(252) Katzke, H.; Depmeier, W. *Phase Transitions* **1996**, *59*, 91.

(253) Katzke, H.; Czank, M.; Depmeier, M.; Van Smaalen, S. *J. Phys.: Condens. Matter* **1997**, *9*, 6231.

(254) Galy, J.; Satto, C.; Sciau, P.; Millet, P. *J. Solid State Chem.* **1999**, *146*, 129.

(255) Ferg, E.; Grummov, R. J.; De Kock, A.; Thackeray, M. M. *J. Electrochem. Soc.* **1994**, *141*, 147.

(256) Colbow, K. M.; Dahn, J. R.; Haering, R. R. *J. Power Sources* **1989**, *26*, 397.

(257) Rossen, E.; Reimers, J. N.; Dahn, J. R. *Solid State Ionics* **1993**, *62*, 53.

(258) Ohzuku, T.; Ueda, A.; Yamamoto, N. *J. Electrochem. Soc.* **1995**, *142*, 1431.

(259) Bach, S.; Pereira-Ramos, J. P.; Baffier, N. *J. Mater. Chem.* **1998**, *8*, 251.

(260) Bach, S.; Pereira-Ramos, J. P.; Baffier, N. *J. Power Sources* **1999**, *81–82*, 273.

(261) Zaghib, K.; Simoneau, M.; Armand, M.; Gauthier, M. *J. Power Sources* **1999**, *81–82*, 300.

(262) Jansen, A. N.; Kahaian, A. J.; Kepler, K. D.; Nelson, P. A.; Amine, K.; Dees, D. W.; Vissers, D. R.; Thackeray, M. M. *J. Power Sources* **1999**, *81–82*, 902.

(263) Scharner, S.; Weppner, W.; Schmid-Beurmann, P. *J. Electrochem. Soc.* **1999**, *146*, 857.

(264) Proskuryakova, E. V.; Kondratov, O. I.; Porotnikov, N. V.; Petrov, K. I. *Zh. Neorg. Khim.* **1983**, *28*, 1402.

(265) Leonidov, I. A.; Leonidova, O. N.; Perelyaeva, L. A.; Samigullina, R. F.; Kovyazina, S. A.; Patrakeev, M. V. *Phys. Solid State* **2003**, *45*, 2183.

(266) Liu, D. Z.; Hayes, W.; Kurmoo, M.; Dalton, M.; Chen, C. *Physica C* **1994**, *235*, 1203.

(267) Julien, C. M.; Massot, M.; Zaghib, K. *J. Power Sources* **2004**, *136*, 72.

(268) Aldon, L.; Kubiac, P.; Womes, M.; Jumas, J. C.; Olivier-Fourcade, J.; Tirado, J. L.; Corredor, J. I.; Pérez Vicente, C. *Chem. Mater.* **2004**, *16*, 5721.

(269) O'Regan, B.; Gratzel, M. *Nature* **1991**, *353*, 737.

(270) Bonino, F.; Busani, L.; Manstretta, M.; Rivolta, B.; Scrosati, B. *J. Power Sources* **1981**, *6*, 261.

(271) Ohzuku, T.; Takehara, Z.; Yoshizawa, S. *Electrochim. Acta* **1979**, *24*, 219.

(272) Cava, R. J.; Murphy, D. W.; Zahurak, S.; Santoro, A.; Roth, R. S. *J. Solid State Chem.* **1984**, *53*, 64.

(273) Wagemaker, M.; Kearley, G. J.; Van Well, A.; Mutka, H.; Mulder, F. M. *J. Am. Chem. Soc.* **2003**, *125*, 840.

(274) De Krol, R. V.; Goossens, A.; Meulenkamp, E. *J. Electrochem. Soc.* **2003**, *146*, 3150.

(275) Ohsaka, T.; Izumi, F.; Fujiki, Y. *J. Raman Spectrosc.* **1978**, *7*, 321.

(276) Sekiya, T.; Ohta, S.; Kamei, S.; Hanakawa, M.; Kurita, S. *J. Phys. Chem. Solids* **2001**, *62*, 717.

(277) Gonzales, R. J.; Zallen, R.; Berger, H. *Phys. Rev.* **1997**, *B55*, 7014.

(278) Dinh, N. N.; Oanh, N. Th. T.; Long, P. D.; Bernard, M. C.; Hugot-Le Goff, A. *Thin Solid Films* **2003**, *423*, 70.

(279) Lindsay, M. J.; Blackford, M. G.; Attard, D. J.; Luca, V.; Skyllas-Kasacos, M.; Griffith, C. S. *Electrochim. Acta* **2007**, *52*, 6401.

(280) Baddour-Hadjean, R.; Bach, S.; Smirnov, M.; Pereira-Ramos, J. P. *J. Raman Spectrosc.* **2004**, *35*, 577.

(281) Smirnov, M.; Baddour-Hadjean, R. *J. Chem. Phys.* **2004**, *121*, 2348.

(282) Hardwick, L. J.; Holzapfel, M.; Novak, P.; Dupont, L.; Baudrin, E. *Electrochim. Acta* **2007**, *52*, 5357.

(283) Murphy, D. W.; Greenblatt, M.; Zahurak, S. M.; Cava, R. J.; Waszczak, J. V.; Hull, G. W.; Hutton, R. S. *Rev. Chim. Miner.* **1982**, *19*, 441.

(284) Lunell, S.; Stashans, A.; Ojamae, L.; Lindstrom, H.; Hagfeldt, A. *J. Am. Chem. Soc.* **1997**, *119*, 7374.

(285) Wagemaker, M.; van de Krol, R.; Kentgens, A. P. M.; van Well, A. A.; Mulder, F. M. *J. Am. Chem. Soc.* **2001**, *123*, 11454.

(286) Lazarev, A. N.; Mirgorodsky, A. P.; Ignatiev, I. S. *Vibrational Spectra of Complex Oxides*; Nauka: Leningrad, 1975.

(287) Padhi, A. K.; Nanjundaswamy, K. S.; Goodenough, J. B. *J. Electrochem. Soc.* **1997**, *144*, 1188.

(288) Amine, K.; Yasuda, K.; Yamachi, M. *Electrochem. Solid-State Lett.* **2000**, *3*, 178.

(289) Okada, S.; Sawa, S.; Egashira, M.; Yamaki, J.; Tabuchi, M.; Kageyama, H.; Konishi, T.; Yoshino, A. *J. Power Sources* **2001**, *97–98*, 432.

(290) Yamada, A.; Chung, S. C.; Hinokuma, K. *J. Electrochem. Soc.* **2001**, *148A*, 224.

(291) Prosini, P. P.; Karewska, M.; Scaccia, S.; Wisniewski, P.; Pasquali, M. *Electrochim. Acta* **2003**, *48*, 4205.

(292) Huang, H.; Yin, S. C.; Nazar, L. *Electrochem. Solid-State Lett.* **2001**, *4A*, 170.

(293) Croce, F.; D'Epifanio, A.; Haussoun, J.; Deptula, A.; Olczac, A.; Scrosati, B. *Electrochem. Solid-State Lett.* **2002**, *5A*, 47.

(294) Chung, S. Y.; Bloking, J. T.; Chiang, Y. M. *Nat. Mater.* **2002**, *2*, 123.

(295) Anderson, A. S.; Kalska, B.; Häggström, L.; Thomas, J. O. *Solid State Ionics* **2000**, *130*, 41.

(296) Yamada, A.; Takei, Y.; Koizumi, H.; Sonoyama, N.; Kanno, R. *Chem. Mater.* **2006**, *18*, 804.

(297) Tucker, M. C.; Doeff, M. M.; Richardson, T. J.; Finones, R.; Reimers, J. A.; Cairnes, E. J. *Electrochem. Solid-State Lett.* **2002**, *5A*, 95.

(298) Tucker, M. C.; Doeff, M. M.; Richardson, T. J.; Finones, R.; Cairnes, E. J.; Reimers, J. A. *J. Am. Chem. Soc.* **2002**, *124*, 3832.

(299) Paques-Ledent, M. T.; Tarte, P. *Spectrochim. Acta* **1973**, *29A*, 1007.

(300) Paques-Ledent, M. T.; Tarte, P. *Spectrochim. Acta* **1974**, *30A*, 673.

(301) Wilson, E. B.; Decius, J. C.; Cross, P. C. *Molecular Vibrations. The Theory of Infrared and Raman Vibrational Spectra*; Dover: New York, 1955.

(302) Paraguassu, W.; Freire, P. T. C.; Lemos, V.; Lala, S. M.; Montoro, L. A.; Rosolen, J. M. *J. Raman Spectrosc.* **2005**, *36*, 213.

(303) Fomin, V. I.; Gnezdilov, V. P.; Kumosov, V. S.; Peschanskii, A. V.; Yeremenko, V. V. *Low Temp. Phys.* **1999**, *25*, 829.

(304) Fomin, V. I.; Gnezdilov, V. P.; Kumosov, V. S.; Peschanskii, A. V.; Yeremenko, V. *Low Temp. Phys.* **2002**, *28*, 203.

(305) Geller, S.; Durand, J. L. *Acta Crystallogr.* **1960**, *13*, 325.

(306) Herzberg. G. *Infrared and Raman Spectra of Polyatomic Molecules*; Van Nostrand: New York, 1975.

(307) Burba, C. M.; Frech, R. *J. Electrochem. Soc.* **2004**, *151A*, 1032.

(308) Lemos, V.; Guerini, S.; Mendes Filho, J.; Lala, S. M.; Montoro, L. A.; Rosolen, J. M. *Solid State Ionics* **2006**, *177*, 1021.

(309) Hong, J.; Wang, C.; Dudney, N. J.; Lance, M. J. *J. Electrochem. Soc.* **2007**, *154A*, 805.

(310) Julien, C. M.; Zaghib, K.; Mauger, A.; Massot, M.; Ait-Salah, A.; Selmane, M.; Gendron, F. *J. Appl. Phys.* **2006**, *100*, 63511.

(311) Doeff, M. M.; Wilcox, J. D.; Kostecki, R.; Lau, G. *J. Power Sources* **2006**, *163*, 180.

(312) Doeff, M. M.; Wilcox, J. D.; Yu, R.; Aumentado, A.; Marcinek, M.; Kostecki, R. *J. Solid State Electrochem.* **2008**, *12*, 995.

(313) Hu, Y.; Doeff, M. M.; Kostecki, R.; Finones, R. *J. Electrochem. Soc.* **2004**, *151*, A1279.